LOI-2001.2

LETTER OF INTENT

A Physics Program Based on a New Asymmetrical Electron-Positron Collider for the Regime $1 < \sqrt{s} < 3$ GeV

V. Blinov, V. Bukind, V. Golubev, S. I. Eidelman, V. N. Ivanchenko, B. Khazin, E. Onuchin, S. I. Serednyakov, E. P. Solodov
Budker Institute of Nuclear Physics, Novosibirsk 630090, Russia

M. Mandelkern, C. Munger, W. Roethel, J. Schultz
University of California at Irvine, Irvine, CA 92697, USA

M. Placidi, F. Sauli
CERN, 1211 Genève 23, Switzerland

M. Sokoloff
University of Cincinnati, Cincinnati, OH 45221, USA

T. Barillari
University of Colorado, Boulder, CO 80309, USA

V. Azzolini, W.Baldini, D. Bettoni, R. Calabrese, G. Cibinetto, G. Ciullo, P. Dalpiaz, P. F. Dalpiaz, P. Lenisa, E. Luppi, M. Martini, M. Negrini, F. Petrucci, M. Savrié
INFN and University of Ferrara, 44100 Ferrara, Italy

R. Baldini, M. Bertani, S. Bellucci, M. Cordelli, P. Levisandri, P. Patteri, A. Zallo
INFN Laboratori Nazionali di Frascati, 00044 Frascati, Italy

M. Schioppa
INFN Gr.Coll. di Frascati and University of Calabria, Arcavacata di Rende, 87036 Cosenza, Italy

U. Mallik
The University of Iowa, Iowa City, IA 52242, USA

R .Arnold, P. Bosted, R. Hicks, G. Peterson, S. Rock
University of Massachussets, Amherst, MA 01003, USA

P. Paolucci, D. Piccolo
INFN and University of Napoli, 80126 Napoli, Italy

T. Dimova, M. Morandin, M. Posocco, P. Sartori, R. Stroili, C. Voci
INFN and University of Padova, 35131 Padova, Italy

G. Bonneau
Ecole Polytechnique, F-91128 Paliseau, France

C. Bini, P. Gauzzi, E. Pasqualucci
INFN and University of Roma 'La Sapienza', 00185 Roma, Italy

V. Bidoli, R. Messi, L. Paoluzi
INFN and University of Roma 'Tor Vergata', 00133 Roma, Italy

T. Fieguth, R. Iverson, L. Keller, S. Menke, M. Perl, M. Sullivan, J. Va'vra
SLAC, P.O. Box 4349, Stanford, CA 94309, USA

S.Conetti, D. B .Day, B.E.Norum
University of Virginia, Charlottesville, VA 22901, USA

Contents

Abstract

We propose a comprehensive physics program at an asymmetrical collider consisting of the PEPII LER and a new electron accelerator, to be constructed in the IR-12 hall at PEP-II. Two options for the electron accelerator are being considered, a storage ring of energy 100 MeV $< E_e <$ 800 MeV and a linac of energy 50 MeV $< E_e <$ 800 MeV. The accessible center of mass energies will then respectively be 1.1 GeV $< \sqrt{s} <$ 3.15 GeV and 0.8 GeV $< \sqrt{s} <$ 3.15 GeV. The 1.4 GeV $\div$ 3.1 GeV energy regime has been inadequately explored in electron-positron collisions. It was studied by ADONE and DCI with a total integrated luminosity of < 3 pb^{-1}. BES acquired inclusive data between 2 and 3 GeV with an integrated luminosity of < 1 pb^{-1}; the region below 1.4 GeV was studied by VEPP-2M with relatively high luminosity and good final state identification; DAΦNE may potentially study the regime below 1.4 GeV. We expect to increase the integrated luminosity between 1.4 and 3.1 GeV to greater than 100 pb^{-1} with high-efficiency and complete identification of hadronic final states.

The principal emphasis of the program will be the accurate determination of R, the ratio of hadron to muon pair cross sections, initially at the 2-3% level but with the goal of a 1% measurement. In determining R by measuring exclusive annihilation cross sections, we will do detailed vector meson spectroscopy in this richly populated but poorly characterized region and measure nucleon, hyperon and meson time-like form factors. We anticipate observing 2γ processes that provide especially clean tests of perturbative QCD.

R is poorly measured in this region. A high precision measurement of R at finely spaced energy intervals is required to accurately evolve the electromagnetic coupling constant in the low energy regime ($\alpha_{EM}(0)$) to the Z scale ($\alpha_{EM}(M_Z^2)$). The latter value, plus knowledge of the Higgs and top masses, is required for computation of electroweak processes, or conversely to predict the Higgs mass from precision electroweak measurements. Similar hadronic corrections are required for the accurate calculations needed for precision tests of the Standard Model such as BNL E821, the current $(g-2)_\mu$ experiment. The proposed new data would reduce the Standard Model uncertainty to a level below the expected statistical error on $(g-2)_\mu$, greatly improving the discovery potential of this and similar experiments.

Precision nucleon electromagnetic form factor data will confront the many puzzles posed by the (poor) existing data; this include the anomalously large neutron time-like form factor, which is several times larger than expected, and the rapid fall of the proton form factor at threshold, suggestive of a narrow bound state. The new measurements will for the first time allow clear separation of the electric and magnetic form factors of the nucleons and will potentially resolve ambiguities in the analytic continuation of these functions.

We anticipate making the first measurements of time-like nucleon transition form factors, i.e. $N-\Delta$. Of the hyperon form factors, only that of the Λ is (badly) measured and measurements of the Λ, charged and neutral Σ and $\Lambda-\Sigma$ transition form are crucial for determining the detailed structure of baryons.

Pion and charged kaon time-like electromagnetic form factors are poorly measured above $Q^2 = 1$ GeV^2. The neutral kaon electromagnetic form factor is poorly measured above the ϕ. Vector meson form factors are essentially unmeasured. Both pseudoscalar and vector meson form factors are constrained by dispersion relations

and have clearly predicted asymptotic forms in perturbative QCD. Form factors are simply related to hadron distribution amplitudes, which characterize hadrons to all orders in strong interactions and are required for computing the QCD amplitudes of more complicated processes.

Electron-positron annihilations to exclusive hadronic final states are ideal for studying excited 1^{--} states. The spectrum of 1^{--} states, their identity as quark-antiquark radial and orbital excitations, hybrids, glueballs, or mixtures of the above, and their organization into SU(3) multiplets are all poorly understood, mainly because of the inadequate data set, a situation which will be rectified at PEP-N. Exclusive multi-hadron final states will be measured to search for exotic and non-exotic resonances in production, such as those recently reported in antiproton annihilation experiments at LEAR and in diffractive photoproduction at FNAL.

Meson-photon transition form factors, e.g. $F_{\pi\gamma^*}$ have particularly simple behavior in pQCD and powerful predictions have been made for their properties. Measurement of $\gamma\gamma^*$ and $\gamma^*\gamma^*$ cross sections will be important in testing the calculations of the light-by-light contribution to $(g-2)_\mu$.

1 Introduction

There is a rich variety of important physics measurements that are accessible to an electron-positron collider in the center of mass energy range $1 < \sqrt{s} < 3$ GeV.

The principal emphasis of the program will be the accurate determination of R, the ratio of hadron to muon pair cross sections. In addition we will measure nucleon, hyperon and meson time-like form factors and we will do detailed vector meson spectroscopy in this richly populated, but poorly characterized region. We will also have the capability to observe 2 photon processes.

Therefore we envision what is effectively a program rather than a single measurement and we expect the active period of data taking to last several years.

This document is organized as follows. The main physics motivations will be discussed in section 2. The measurement method of R and the experimental requirements will be the subject of section 3. Section 4 will be devoted to the study of backgrounds. The experimental apparatus will be described in detail in section 5. Monte Carlo simulation of hadronic channels and the measurement of R will be discussed in section 6, while nucleon-antinucleon final states are the subject of section 7. Finally in section 8 we will present our conclusions.

2 Physics Motivation

2.1 The importance of R

A crucial issue that has only recently attracted attention is that we cannot test the Standard Model without taking hadron physics into account. The parameters of the Standard Model can be taken as G_F, $\alpha_{em}(0)$, M_Z, M_H and the fermion masses. In order to compute physical quantities we must include radiative corrections. Although the electroweak radiative corrections are calculable, the hadronic radiative corrections are not. One such correction, the hadronic vacuum polarization diagram shown in Fig. 1, contributes significantly to the evolution of α_{em} and to the anomalous magnetic moment of the muon, $a_\mu \equiv (g_\mu - 2)/2$. The relevant diagrams are given in Fig. 2.

The value of $\alpha_{em}(M_Z^2)$ is vital for determining the mass of the Higgs boson. The hadronic vacuum polarization diagram can be determined directly from the ratio $R = \sigma(e^+ + e^- \to \text{hadrons})/\sigma(e^+ + e^- \to \mu^+ + \mu^-)$. We propose to obtain an accuracy on R of at least 2.5% in the range $1.4 < \sqrt{s} < 3.1$ GeV, which would significantly reduce the uncertainty of the calculated value of the mass of the Higgs and reduce the errors on the calculated value of $g_\mu - 2$ to below the proposed experimental errors.

2.1.1 α_{em}

The value of the QED coupling at the Z pole, $\alpha_{em}(M_Z^2)$, is the most poorly determined of the three fundamental parameters $G_F, M_Z, \alpha_{em}(M_Z^2)$. $\alpha_{em}(M_Z^2)$ is $\sim$1/129 compared to $\alpha_{em}(0) \simeq$1/137. To illustrate the dependence on $\alpha_{em}(M_Z^2)$ of electroweak observables (such as M_W) we give the expression for $sin^2\theta_W$ in the NOV scheme in which the m_t and M_H dependences have been removed:

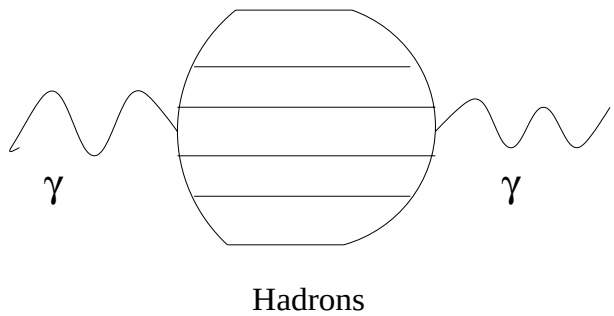

Figure 1: The Feynmann diagram that contributes to the hadronic part of $g_\mu - 2$ and the evolution of α_{EM}.

$$sin^2\theta_W(1 - sin^2\theta_W) = \frac{\pi\alpha_{em}(M_Z^2)}{\sqrt{2}G_F M_Z^2} \tag{1}$$

Furthermore, it is the precision to which we know $\alpha_{em}(M_Z^2)$ that also limits the accuracy of the indirect prediction of the mass M_H of the (Standard Model) Higgs boson[1]. The evolution of α_{em} is given by:

$$\alpha_{em}(s)^{-1} = [1 - \Delta\alpha_{lep}(s) - \Delta\alpha_{had}^{(5)}(s) - \Delta\alpha_{top}(s)]\alpha_{em}^{-1}(0). \tag{2}$$

The leptonic term $\Delta\alpha_l(s)$ is accurately known. The hadronic contribution is divided so m_t can be treated as a parameter in standard model fits. The term $\Delta\alpha_{had}^{(5)}(s)$, which includes the contributions of the u through b quarks, must be determined experimentally using the relation:

$$\Delta\alpha_{had}^{(5)}(s) = -\frac{\alpha_{em}(0)s}{3\pi} P \int_{4m_\pi^2}^{\infty} \frac{R(s')ds'}{s'(s'-s)} \tag{3}$$

where R=$\sigma(e^+ + e^- \to \text{hadrons})/\sigma(e^+ + e^- \to \mu^+ + \mu^-)$, $\alpha_{em}^{-1}(0) = 137.0359895(61)$ and P denotes principal value. The integral is weighted toward the low energy contributions due to the $1/s'$ in the integrand.

There have been many efforts to calculate $\Delta\alpha_{had}^{(5)}(M_Z^2)$ [1-18] from experimental data supplemented by theoretical models such as pQCD at high energy, non-perturbative gluon and light quark condensates, analyticity, space-like calculations etc. Not only have the calculated values varied over a wide range, but there has also been a wide range of uncertainties. Fortunately, new data have been published from CMD-2 [19], SND [20] at VEPP-2M at $\sqrt{s} < 1.4$ GeV, BES [21] at $\sqrt{s} > 2.5$ GeV and BES-II data [22] for 2 GeV $< \sqrt{s} <$ 5 GeV. The release of the new BES-II data has led to new calculations, e.g., by Martin, Outhwaite and Ryskin [15] (with two different models, 0.02738 ± 0.00020 and 0.02761 ± 0.00022), Jegerlehner [16] (0.02787 ± 0.00039), and Burkhardt and Pietrzyk [17] (0.02761 ± 0.00036).

As seen in Table 1 (see [16]), for $\Delta\alpha_{had}^{(5)}(M_Z^2)$ the uncertainty arising from the intermediate energy range from 1.4 to 3.1 GeV is already higher than that from the low energies making new precise measurements of the e^+e^- hadronic cross sections in this range absolutely necessary.

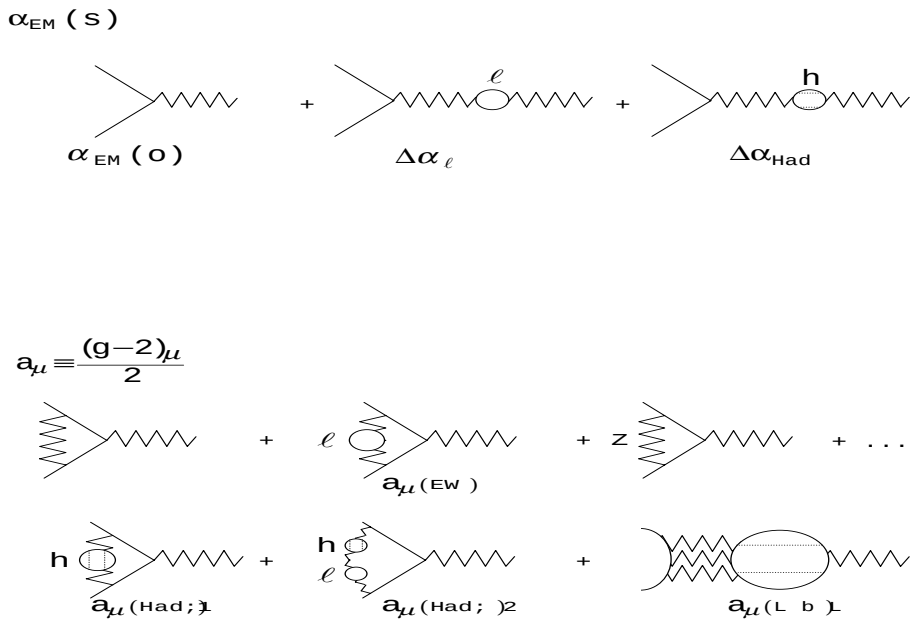

Figure 2: Feynman diagrams for radiative corrections to α_{em} and $(g-2)_\mu$

The strong influence of the low energy data is a general feature of all the calculations. Burkhardt and Pietrzyk [17] use all available annihilation data in parametrized form. For $\sqrt{s}$ >12 GeV they use third-order perturbative QCD with $\alpha_s(M_Z^2) = 0.118 \pm 0.002$. The largest contributions to the uncertainty in $\Delta\alpha_{had}^{(5)}(s)$ are from the measured values of R in the regions 1.05< s <2.0 GeV and 2.0< s <5.0 GeV, each contributing roughly equally as shown in Fig. 3, where the pie charts of Ref. [17] are given. The latter uncertainty decreased significantly after inclusion of the BES-II (inclusive) data even though the measurements between 2-3 GeV have large errors and potentially significant systematic uncertainties.

Unfortunately, the critical energy range $1.4 < \sqrt{s} < 2.0$ GeV still suffers from old data of limited precision and is out of the range of existing colliders. Fig. 4 taken from ref. [23] shows the large experimental errors and possible structure in this energy region. This uncertainty introduces an error into the prediction of the Higgs Mass M_H in Standard Model calculations. Using an analytic approximation [2] we find that at $M_H \sim 100$ GeV, $\delta M_H(\text{GeV}) \sim -32000\delta\Delta\alpha_{had}^5(M_Z^2)$. Thus, if we take the current experimental error $\delta\Delta\alpha_{had}^5(M_Z^2)$ to be ± 0.00036 [17], this corresponds to $\delta M_H = \pm 12$ GeV.

To further illustrate the sensitivity of electroweak model parameters to $\alpha_{em}(M_Z^2)$, or alternatively, our ability to test the electroweak model, we show in Fig. 5 the LEP EW WG [24] determination of $sin^2\theta_{eff}^l$ from asymmetry data and the Standard Model prediction given as a function of M_H with uncertainties due to $\Delta\alpha_{had}^{(5)}$ and m_t. The uncertainty due to $\Delta\alpha_{had}^{(5)}$ is $\sim \pm 0.0003$, which is larger than the experimental error. The overall fit to M_H from all electroweak data, shown in Fig.6, yields an estimate of ~ 100 GeV in

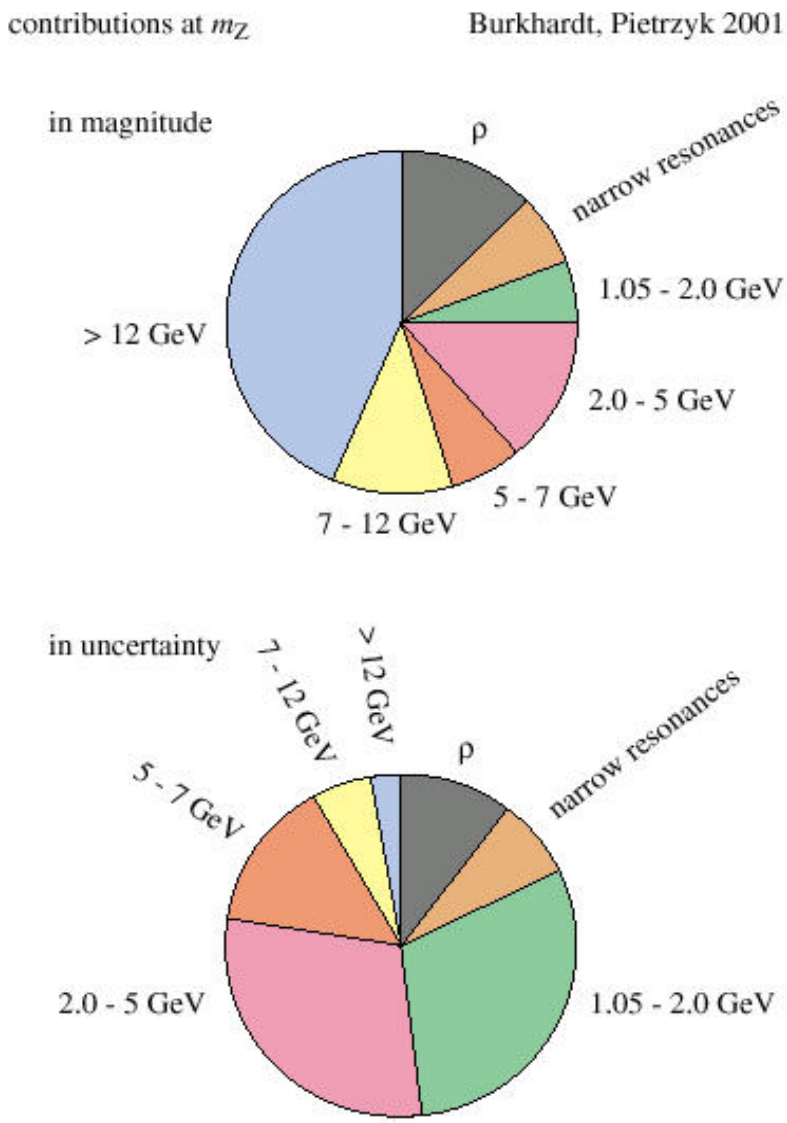

Figure 3: Relative contributions to $\Delta\alpha^{(5)}_{had}(M_Z^2)$ in magnitude and uncertainty from Burkhardt and Pietrzyk [17].

$\sqrt{s}$ (GeV)	$\Delta\alpha^{(5)}_{had}(M_Z^2)$ (10^{-4})	a_μ^{had} (10^{-10})
2m$_\pi$-1.4	47.72 ± 0.74	603.9 ± 6.2
1.4-3.1	26.75 ± 1.83	60.1 ± 5.0
> 3.1	204.25 ± 3.36	29.2 ± 1.1
Total	278.72 ± 3.90	693.2 ± 8.0

Table 1: Hadronic corrections to $\Delta\alpha^{(5)}_{had}(M_Z^2)$ and a_μ^{had}

which the dominant uncertainty is from $\Delta\alpha^{(5)}_{had}$. Still another example of the dependence of predictions of fundamental parameters on $\Delta\alpha^{(5)}_{had}$ is shown in Fig. 7.

We take as our goal the reduction of error on $\Delta\alpha^{(5)}_{had}(M_Z^2)$ (from the integral in Eq. 3) in our kinematic region to a level below that in other kinematic regions:

1. For $1.4 < \sqrt{s} < 2.0$ GeV, the region below the range of BES, we will reduce the error to about 0.3×10^{-4}. This implies that the error on the integral over R in Eq. 3 will be less than 3%, an improvement of about a factor of 5 over the current uncertainty.

2. For $2.0 < \sqrt{s} < 2.5$ GeV which is covered by the BES-II results, we will reduce the current error by about a factor of two. This region has the second biggest contribution to the total error. The overall uncertainty on $\Delta\alpha^5_{had}(M_Z^2)$ would then be about 0.00013, giving $\delta M_H \sim 4$ GeV.

2.1.2 $g_\mu - 2$

Theoretically, the anomalous g value is the simplest quantity calculable to extremely high precision in the Standard Model. The comparison of precise measurements of $a_\mu = (g_\mu - 2)/2$ with theory thus provides a crucial test of the Standard Model [25] and may open up a window for new physics. The goal of the current $g_\mu - 2$ experiment, E821, at Brookhaven National Laboratory [25] is to reach a precision of 4×10^{-10} and substantial progress has been made [26]. The recent results from E821 [27] for the positive muon give $a_\mu = 11659202(14)(6) \times 10^{-10}$, yielding a difference between the world average experimental value and the existing Standard Model prediction of $(43 \pm 16) \times 10^{-10}$. It is now necessary to calculate a_μ to even greater accuracy than before.

In the Standard Model, $a_\mu = a_\mu^{QED} + a_\mu^{weak} + a_\mu^{had}$, where a_μ^{QED} and a_μ^{weak} are known to a few parts in 10^{11}. The uncertainty in a_μ is dominated by that in a_μ^{had} which is usually broken up (see Fig. 2) into the leading vacuum polarization contribution $a_\mu(had;1)$ of

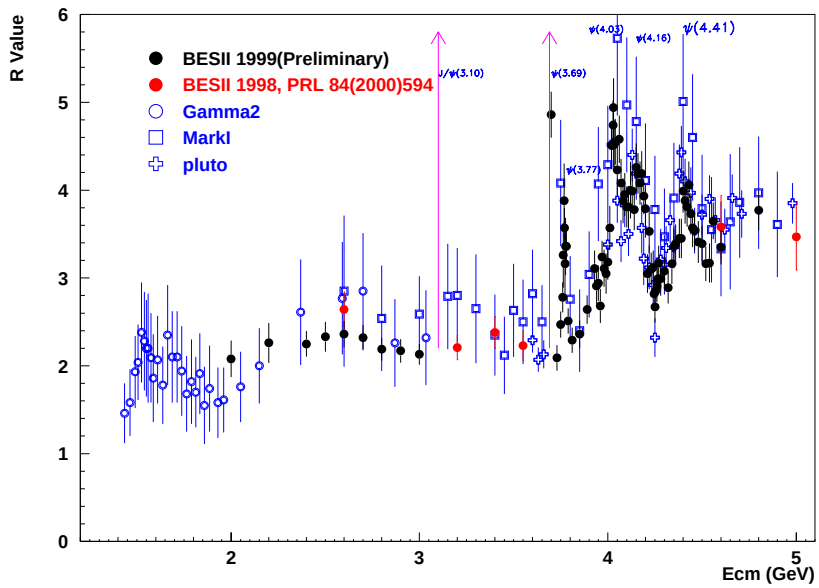

Figure 4: R vs. center of mass energy in the low energy regime. The solid circles are the new preliminary results from BES-II [22]. The region below 2 GeV still has large errors and may have structure. The figure is taken from ref. [23].

order $(\frac{\alpha}{\pi})^2$, the higher order vacuum polarization contribution $a_\mu(had;2)$ of order $(\frac{\alpha}{\pi})^3$, and the hadronic light-by-light contribution $a_\mu(lbl)$, also of order $(\frac{\alpha}{\pi})^3$. The first of these is related to R as given below, and the second and third must be estimated. Ignoring the latter higher order contributions, the leading part, usually identified as the hadronic vacuum polarization contribution, is then given by [3, 28]

$$a_\mu^{had} = \frac{\alpha^2(0)}{3\pi^2}\int_{4m_\pi^2}^{\infty} ds \frac{K(s)}{s} R(s) \tag{4}$$

$$K(s) = x^2(1-\frac{x^2}{2}) + (1-x)^2(1+\frac{1}{x^2})(\ln(1+x) - x + \frac{x^2}{2}) + \frac{(1+x)}{(1-x)}x^2 \ln x, \tag{5}$$

where $x = (1-\beta_\mu)/(1+\beta_\mu)$ and $\beta_\mu = \sqrt{1-4m_\mu^2/s}$. The greatest contribution comes from the low energy part of the integral with $\sim 92\%$ coming from $\sqrt{s} < 1.8$ GeV[3]. The current value, $a_\mu^{had} = (693.2 \pm 8.0) \times 10^{-10}$, has an error twice as large as the goal of the BNL experiment. Thus the kinematic region $1.4 < \sqrt{s} < 3.1$ GeV is critical. As discussed in more detail below, the contribution to a_μ^{had} from this range is $\sim 6 \times 10^{-9}$. Reduction

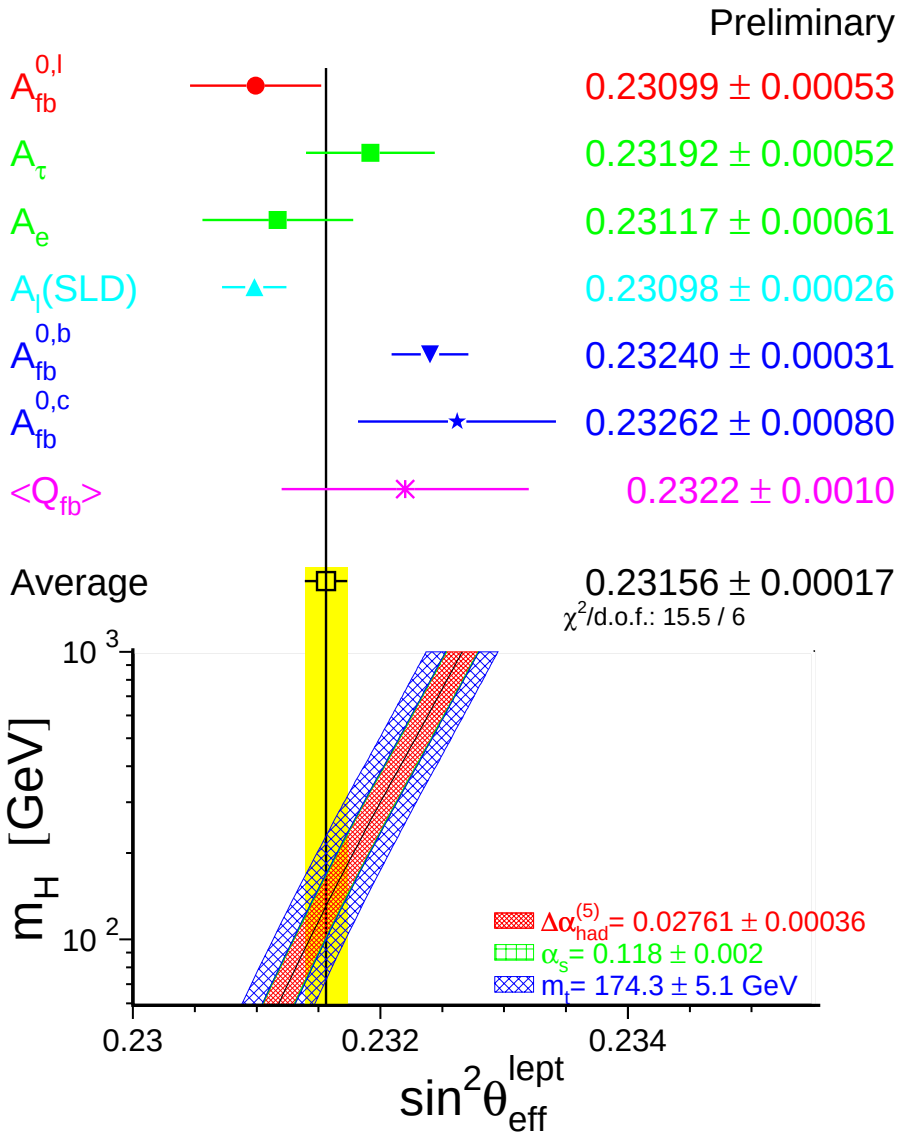

Figure 5: Measurements of the effective leptonic $\sin^2\theta_W$ and the predictions of the Standard Model with uncertainties due to $\Delta\alpha_{had}^{(5)}$ and m_t.

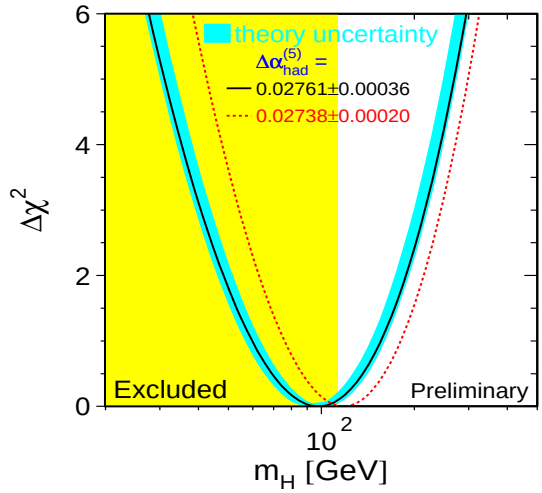

Figure 6: Light Higgs mass prediction of precision electroweak data, with uncertainty due to hadronic corrections

of the error in this region to $\sim 1 \times 10^{-10}$ requires an accuracy in the R measurement of 2.5%.

Various calculations of a_μ^{had} exist in the literature [7, 8, 9, 29, 30, 31, 32]. The approaches of these papers vary by the extent of use of QCD and τ lepton data in addition to the data on e^+e^- annihilation into hadrons. The approach of [7, 33] is based on e^+e^- data below 12 GeV and the predictions of perturbative QCD in the higher energy region giving a negligible contribution to the total uncertainty.

Table 1 presents the contributions to a_μ^{had} from three energy regions: from threshold of hadron production to 1.4 GeV (the range of the VEPP-2M collider in Novosibirsk), from 1.4 GeV to 3.1 GeV (the range of the PEPN) and the one above 3.1 GeV [7, 33]. From the Table it is clear that at the moment the largest contribution to the uncertainty of a_μ^{had} comes from the low energy range, predominantly from the ρ meson region. Although the accuracy of the recent measurement in the energy range 610 to 960 MeV is rather high and better than 0.6% [34], since the contribution of the energy region below 1.4 GeV is large by itself, the absolute uncertainty is also high (6.2 of the total 8.0 in units of 10^{-10}). Analysis of the data recorded at VEPP-2M is still in progress and some improvement of the overall accuracy is expected. Moreover, successful beginning of the analysis of the radiative return data at the KLOE detector at DAΦNE [35] and at BaBaR at SLAC B-factory [36] shows that completely independent measurements of the cross section below 1 GeV with data samples comparable to VEPP-2M are possible. An improvement in the accuracy by a factor of about 2 is expected below 1.4 GeV so the uncertainty coming from the range 1.4 to 3.1 GeV dominates.

Some recent analyses have used τ decay data to supplement e^+e^- data. Here CVC (see the section 2.2) is used to relate processes through the vector charged weak current to comparable processes through the isovector electromagnetic current assuming no second class weak currents, which implies that the contribution of the axial vector current to

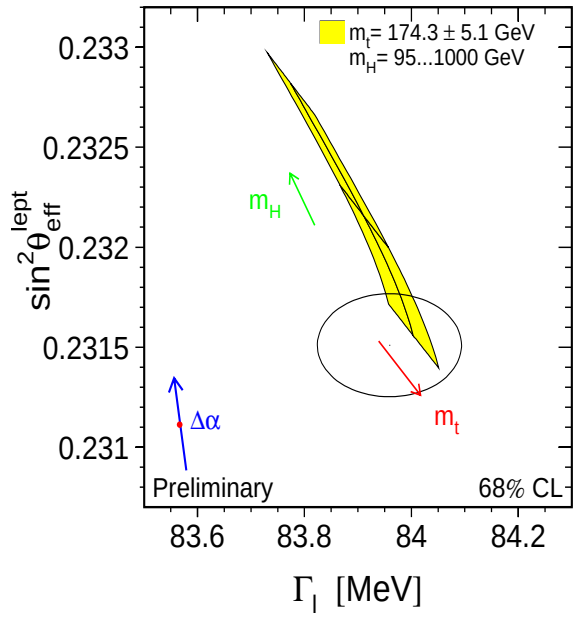

Figure 7: LEP-I+SLD measurements of $\sin^2\theta_{eff}^{lept}$ and Γ_{ll}, the leptonic width of the Z, and the Standard Model prediction. The point shows the predictions where among the electroweak radiative corrections only the photon vacuum polarization is included. The corresponding arrow shows the variation of this prediction if $\alpha_{EM}(M_Z^2)$ is changed by one standard deviation. This variation gives an additional uncertainty to the Standard Model prediction shown in the figure.

$G = +1$ decays is zero. Thus annihilation cross sections with $G = C(-1)^I = +1$ are obtained from the rates of corresponding τ decays. The result of Davier and Hocker [37], who use τ data and pQCD, for the leading vacuum polarization contribution is $a_\mu^{had} = 6924(62) \times 10^{-11}$, which gives the dominant uncertainty in a_μ. While τ decay data are useful at the current level of accuracy, I-spin violation and effects such as initial and final state radiation must be understood if we are to rely on it at smaller experimental errors, as emphasized by Eidelman and Jegerlehner [38, 39] and by Melnikov [40].

The higher order hadronic vacuum polarization and hadronic *light-by-light* contribution are comparable. However while the uncertainty in the former is several parts in 10^{11}, the uncertainty in the latter is much larger. The detailed calculations done by Hayakawa and Kinoshita [41] and by Bijkens, Pallante and Prades [42] give a negative a_μ^{lbl} which is of opposite sign to that obtained from the simple light quark loop calculation first done by Laporta and Remiddi [43]. Marciano and Roberts in their recent review [44] take $a_\mu(lbl) = -85(25) \times 10^{-11}$ for an overall result of $a_\mu^{SM} = 116591597(67) \times 10^{-11}$, to be compared with the BNL E821 [45] result of $116592020(160) \times 10^{-11}$ for a discrepancy of $423(173) \times 10^{-11}$. Since BNL E821 ultimately anticipates an uncertainty of 40×10^{-11}, we must clearly do better on the hadronic vacuum polarization and light-by-light scattering to make use of high-precision measurements of $(g-2)_\mu$.

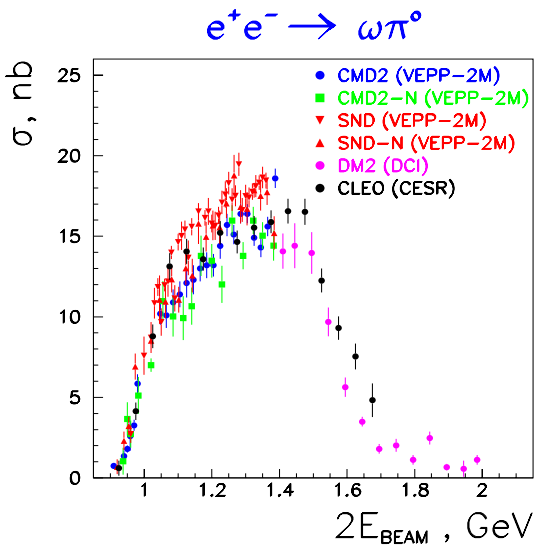

Figure 8: Cross section of $e^+e^- \to \omega\pi^0$ and the corresponding spectral function for the τ^- decay (CLEO data).

2.1.3 Summary

We propose a measurement of R in the energy range $1.0 < \sqrt{s} < 3.1$ GeV with a statistical precision of 1% and initially with a systematic uncertainty of 2% or better. This will allow the calculation of $g_\mu - 2$ to an accuracy better than the projected experimental uncertainty of the BNL experiment, leading to a stringent test of the Standard Model. The measurement will lead to a reduced uncertainty in $\alpha_{em}(M_Z^2)$ which will reduce the currently large uncertainty in the calculated mass of the Higgs to less than 5 GeV. It is worth noting that at PEP-N we will have the excellent knowledge of the center of mass energy essential for the accurate measurement of R, both from beam diagnostics and from the measurement of thresholds for $N\bar{N}$ and $\Lambda\bar{\Lambda}$.

2.2 Testing CVC

Another important issue which can be addressed in e^+e^- is a test of the conservation of the vector current (CVC). It is well known that CVC and isospin symmetry relate cross sections for e^+e^- annihilation into isovector hadronic final states and corresponding decays of the τ lepton [46]. For the Cabibbo allowed vector part of the weak hadronic current, the hadronic mass distribution in the τ lepton decay is given by the following expression:

$$\frac{d\Gamma}{dq^2} = \frac{G_F^2 cos^2\theta_c S_{EW}}{32\pi^2\alpha^2 m_\tau^3} \times (m_\tau^2 \ - \ q^2)^2 \ (m_\tau^2 \ + \ 2q^2) \ v_1(q^2),$$

where G_F is the Fermi constant, θ_c is the Cabibbo angle, S_{EW} is a factor taking into account electroweak radiative corrections, approximately equal to 1.0194 [47], m_τ is the

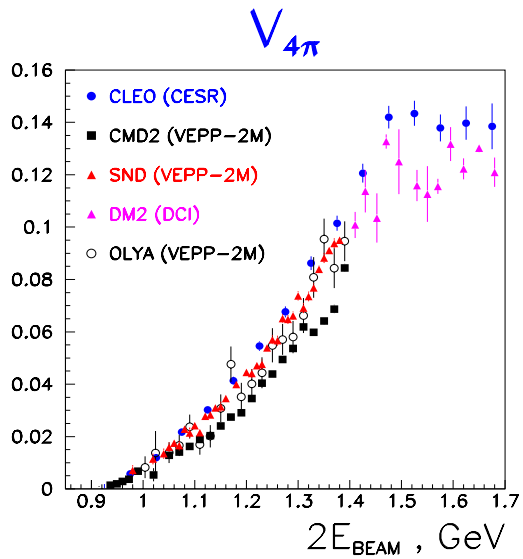

Figure 9: Spectral function for the decay $\tau^- \to 2\pi^-\pi^+\pi^0\nu_\tau$ (CLEO data) and its predictions from e^+e^-.

τ lepton mass and $v_1(q^2)$ is a spectral function:

$$v_1(q^2) = \frac{q^2\sigma^{I=1}_{e^+e^-}(q^2)}{4\pi\alpha^2},$$

where $\sigma^{I=1}_{e^+e^-}(q^2)$ is the cross section of e^+e^- annihilation into hadrons with I=1. Integrating the differential rate, one obtains the branching ratio for the decay into neutrino plus any hadronic state, X, where the allowed quantum numbers for X are:

$$J^{PG} = 1^{-+}, \quad \tau \to 2n\pi\nu_\tau, \quad \omega\pi\nu_\tau, \quad \eta\pi\pi\nu_\tau, ...$$

Using experimental data on e^+e^- into hadrons with I=1, one can confront the CVC predictions and τ lepton decay data for both decay spectra and branching ratios. The total probability of the decays covered by CVC is about 31% or almost a half of all hadronic decays of the τ lepton. Thus, tests of CVC validity serve as a good test of the Standard Model. In addition, as suggested in [8], if CVC is valid, an interesting possibility appears. One can use precise measurements of the τ decays into two and four pions for an inverse procedure - determination of the corresponding exclusive e^+e^- cross sections from τ and improvement of the accuracy in the calculations of various hadronic corrections [48]. While the first tests of CVC have already demonstrated its validity with about 5% accuracy [49], the increasing experimental precision in both the e^+e^- and the τ sectors has revealed some problems. The current situation is summarized in Table 2 [33].

The predicted rate for the decay into two pions is obviously below the observed world average value. This difference also manifests itself in the regular excess of the τ spectral function for the decay into two pions over that from e^+e^- recently confirmed by CLEO

Hadronic State X	CVC, 2001	World Average	WA - CVC
$\pi^-\pi^0$	24.43 ± 0.26	25.31 ± 0.18	0.88 ± 0.32
$\pi^-3\pi^0$	1.07 ± 0.05	1.08 ± 0.10	0.01 ± 0.11
$2\pi^-\pi^+\pi^0$	3.84 ± 0.17	4.19 ± 0.23	0.35 ± 0.29
$\omega\pi^-$	1.82 ± 0.07	1.92 ± 0.07	0.10 ± 0.10
$\eta\pi^-\pi^0$	0.13 ± 0.02	0.17 ± 0.02	0.04 ± 0.03
Others	0.37 ± 0.11	0.24 ± 0.02	-0.13 ± 0.11
Total	29.84 ± 0.37	30.99 ± 0.31	1.15 ± 0.48

Table 2: Branching ratios of $\tau^- \to X^-\nu_\tau$, %

[50]. The effect can be due to the isospin breaking corrections for $m_{\pi\pm} \neq m_{\pi 0}$ [8, 51, 52] as well as to additional radiative corrections in τ decays which are not negligible and according to some estimates can reach 0.8% [52, 53].

For decays into the 4π and the $\omega\pi$ final states the difference between the CVC based predictions and measured branching ratios is smaller and not statistically significant. However, as seen from Figs. 8,9, while below 1.4 GeV the agreement is fairly good, above this energy the τ data are systematically higher than those from the e^+e^- data [54]. This necessitates new high statistics measurements of the corresponding e^+e^- cross sections with a good detector. A single experiment covering the energy range from 1.3 GeV to the τ lepton mass will clarify the difference between the four pion cross sections measured by two detectors at VEPP-2M and will also facilitate the problem of matching e^+e^- cross sections from VEPP-2M and DCI at 1.4 GeV.

2.3 Nucleon form factors

The form factors of the proton and neutron are fundamentally important in that they describe the bound state properties of three valence quarks in the configuration that dominates the known baryonic matter in the universe. The form factors embody the

probability that a nucleon will remain intact after absorption of a virtual photon with four-momentum transfer Q^2, as shown in Fig. 10, where we define the form factors to be space-like for $Q^2 < 0$, and time-like for $s = Q^2 > 0$. In Appendix I we give the differential cross section for $e^+e^- \to N\overline{N}$ in terms of the form factors and provide some further discussion of kinematics.

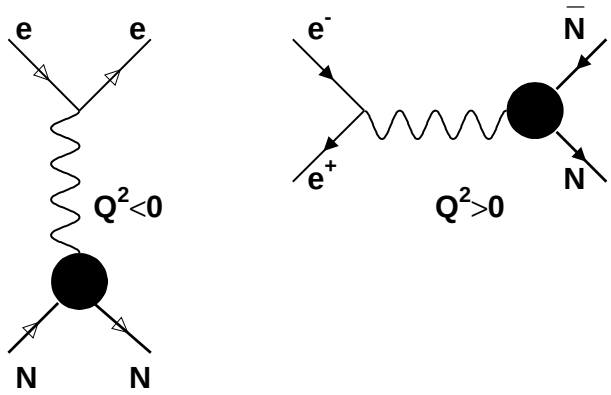

Figure 10: Feynman diagrams containing the nucleon form factors

Confronting nucleon form factor data with QCD-based models of quark bound states is one of the most important ways of pinning down parameters of the models, which then can be used to predict other observables. At small Q^2 the form factors can be thought of as describing the distribution of charge and magnetization current within the nucleons, while at high Q^2 they probe the valence quark distribution functions at high relative momentum [55, 56], with the dominant Feynman diagram being the exchange of two gluons. As QCD models develop, and are able to predict phenomena over the full range of Q^2, from the non-perturbative regime near threshold to the perturbative regime at very large Q^2, nucleon form factor data will be crucial in testing the validity and applicability of these approaches to solving QCD.

A great deal of effort has been put into elucidating the form factors in the space-like region, with ongoing efforts at several laboratories to improve the separate determinations of both electric and magnetic form factors of both the proton and neutron over an increasingly large Q^2 range, and also to determine the form factors of strange baryons.

Much less is known about the time-like form factors. Even so, many questions have been raised by the existing data [57] and there is clearly a strong case [58, 59] to be made for new measurements of the neutron time-like electric and magnetic form factors. In addition, measurements that separate the electric and magnetic (or equivalently the Pauli and Dirac) form factors of the proton are called for by the surprisingly strong variation with Q^2 of the existing data near threshold, in which the form factors were not separately measured. This strong Q^2 dependence may be related to the narrow structures

observed in multihadronic cross sections near the $N\overline{N}$ threshold. For this reason it is important to make improved measurements of multihadronic cross sections with good energy resolution in a variety of channels in addition to measuring the nucleon form factors.

At present, predictions of nucleon form factors are applicable to high $|Q^2|$ in both the space-like and time-like regions. Analyticity relates time-like and space-like form factors, predicting a continuous transition and space-like time-like equality at asymptotic $|Q^2|$. This behavior is also found by pQCD [55, 56], which in addition predicts $F_1(Q^2) \propto \alpha_S^2(Q^2)/Q^4$ and $F_2(Q^2) \propto \alpha_S^2(Q^2)/Q^6$. Here $\alpha_S(Q^2)$ is the strong coupling constant, $F_1(Q^2)$ is the non-spin flip form factor and $F_2(Q^2)$ is the spin flip form factor, which decreases with an extra power of $1/Q^2$ due to helicity conservation. Both pQCD [60, 61] and analyticity [62] predict that the ratio of neutron to proton form factors is < 1, namely $(G_M^n/G_M^p)^2 \sim (q_d/q_u)^2 \sim 0.25$ in both the time-like and space-like regions. This prediction is expected to hold in the threshold region based on pQCD and dispersion relations [58, 59], and the known vector meson spectrum.

There are several unexpected experimental features in the existing data for time-like form factors that motivate the need for a new high statistics experiment with the ability to separately measure the electric and magnetic form factors (or equivalently F_1 and F_2). These are summarized as follows:

- Ratio between neutron and proton form factors: The measurements of the neutron magnetic time-like form factors are shown in Fig.11, as obtained primarily by FENICE [57]. Two further measurements by DM2 at DCI are included [63], at $Q^2 = 5.75$ GeV^2 on the basis of two candidate events, and from the Λ time-like form factors according to U-spin invariance (that is $G_M^n \sim 2G_M^\Lambda$) [64]. Remarkably, the neutron magnetic form factor is found to be larger than that of the proton, at variance with the predictions of most models. Calculations in which the form factors are largely determined by valence quarks have great difficulty in predicting such a large neutron magnetic form factor. Large neutron to proton form factor ratios have been predicted by using rather extreme parameters in several effective low-energy VDM [65]; similar values of neutron to proton form factors are predicted by Skyrme [66] models.

  One factor responsible for the large experimental neutron to proton form factor ratio may be the simplifying assumption required to extract G_M from the experimental cross sections (i.e. $G_M^n = G_E^n$ and $G_E^p = G_M^p$) These statements are exact at threshold, (see Appendix I) but may be poor approximations above threshold. A new high statistics measurement is needed to separate electric and magnetic form factors in order to obtain an *ansatz*-free determination of the ratios G_M^n/G_M^p and G_E^n/G_E^p as a function of Q^2.

- Threshold Q^2 dependence: The proton magnetic form factor has a rapid fall with Q^2 just above threshold. This result was achieved by the PS-170 experiment at LEAR [67]. The data are shown in Fig. 12(a). For the neutron, there may also be a strong fall with Q^2 above threshold. The existing statistics-limited data from FENICE[57] are more compatible with a non-isotropic than an isotropic angular

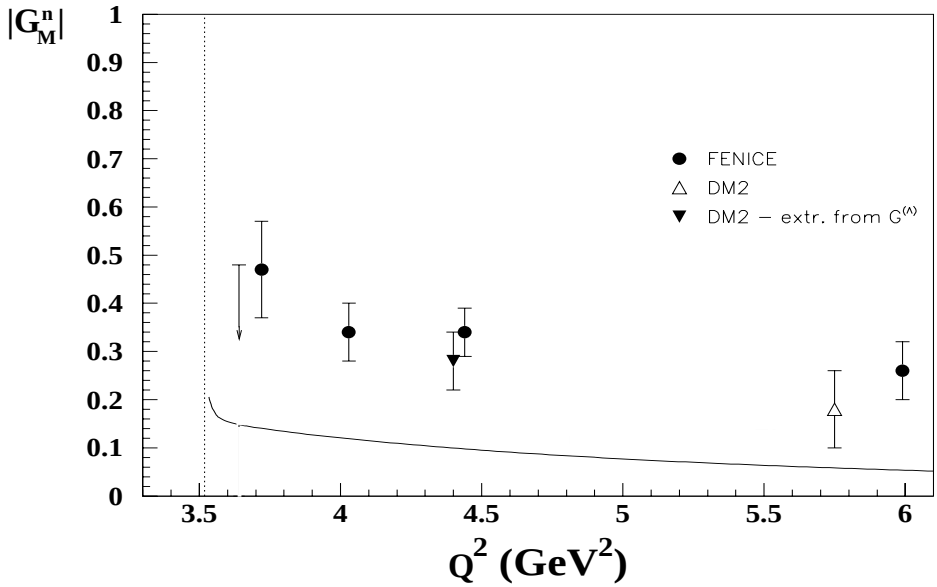

Figure 11: Neutron magnetic form factor in the time-like region. The solid line represents a pQCD based prediction for the asymptotic behavior $|G_M^n| = 0.5|G_M^p|$. The dotted line indicates the $n\overline{n}$ threshold.

distribution, suggesting that $G_M^n \gg G_E^n$ in the accessible energy range. Since at threshold the relationship $G_M(4M^2) = G_E(4M^2)$ (see Appendix I) is exact, this result may result from a rapid decline of G_E^n with increasing Q^2. On the other hand, if G_M^n and G_E^n are actually comparable such that their ratio has a weak Q^2-dependence (that is $G_E^n \sim G_M^n \sim 0.35$ at 4 GeV^2), the existing data imply a very large ratio of time-like to space-like electric form factor at $|Q^2| = 4$ GeV^2, as the existing space-like data are consistent with $G_E^n(-4M^2) \sim 0$.

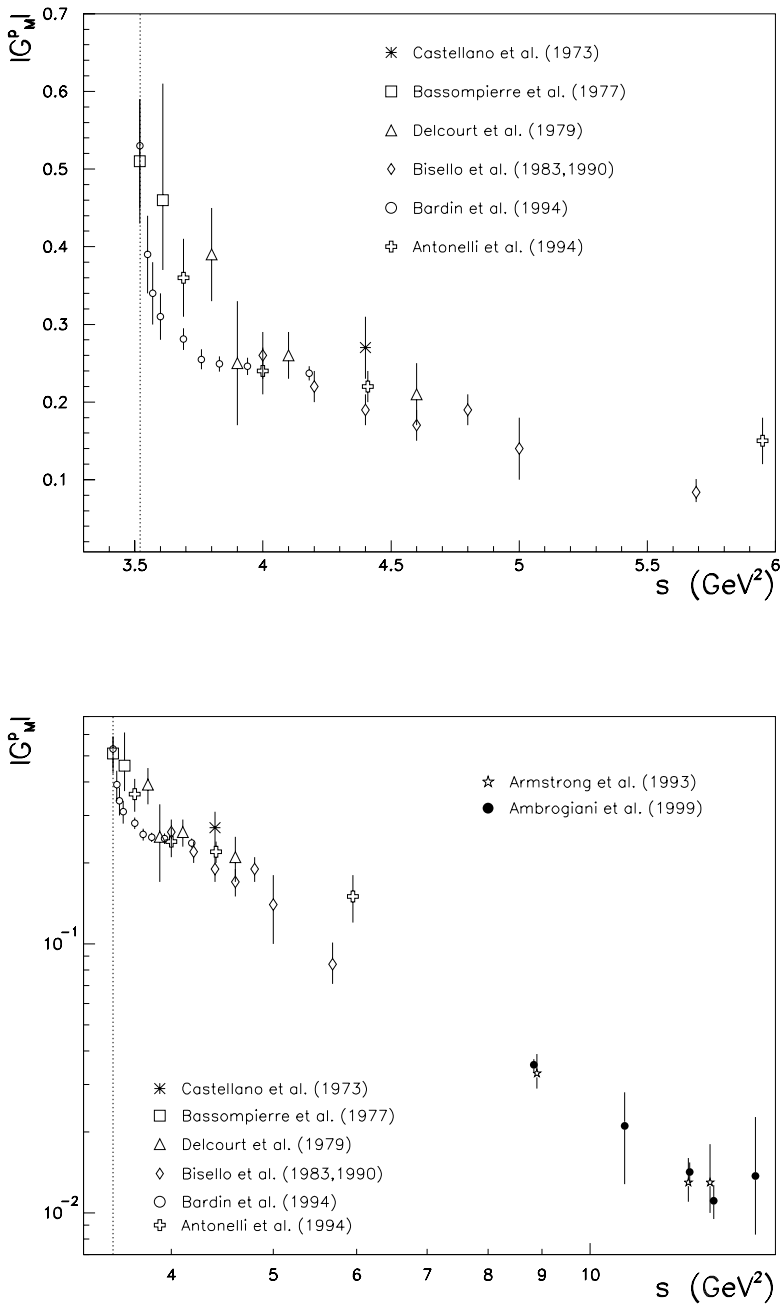

Figure 12: Proton time-like form factor: (a) low $|Q^2|$, (b) high $|Q^2|$. The dotted line indicates the $p\overline{p}$ threshold. See [68] for experimental references.

- High $|Q^2|$ predictions: In the Q^2 range explored to date the proton magnetic time-like form factor remainis substantially larger than the space-like form factor measured at the same $|Q^2|$. The various measurements of the proton magnetic time-like form factor [67, 68] are shown in Fig.12. The expected high Q^2 behavior $1/Q^4$ [69] is reached quite early, however the time-like form factor is approximately twice the space-like form factor measured at the same $|Q^2|$. The same factor is observed in the pion form factor; in this case a qualitative explanation has been suggested in an improved pQCD analysis in terms of integrable singularities of the propagaters [70]. Disentangling electric and magnetic form factors would permit a better understanding of the high Q^2 behavior.

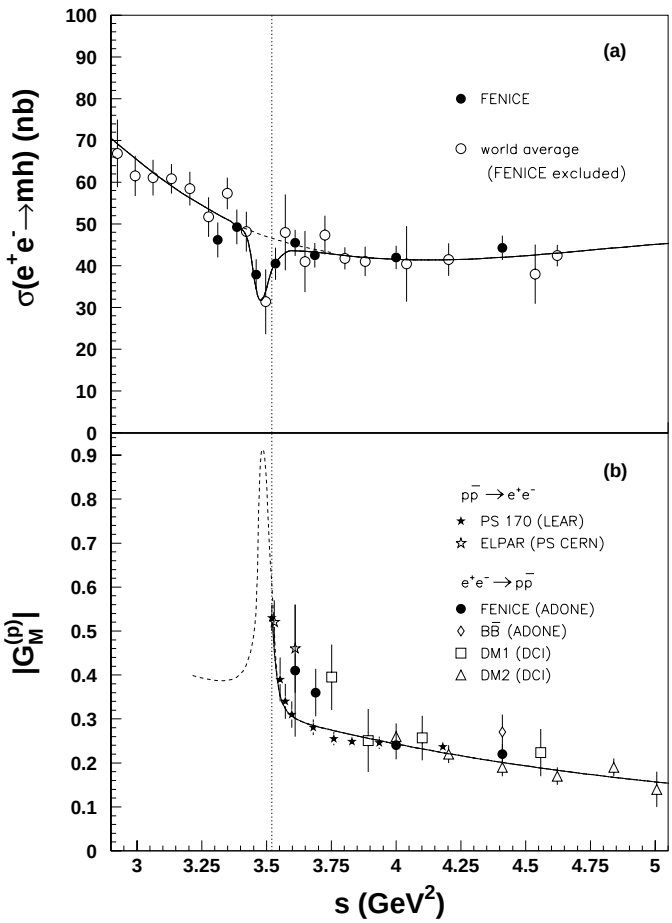

Figure 13: (a) Total multihadronic cross section (FENICE data and the average over previous experiments) superimposed on the result of a fit to a narrow resonance below the $N\overline{N}$ threshold; (b) comparison of the proton FF data to the expected behavior for such a resonance. The dotted line indicates the $p\overline{p}$ threshold.

- Resonant structures: The steep Q^2-dependence of the proton form factor near threshold [71-75] suggests a relatively narrow structure below threshold, which would be seen also in multihadronic e^+e^- annihilation near the $N\overline{N}$ threshold

[76]. Anomalies are indeed seen in the total cross section $\sigma_{tot}(e^+e^- \to hadrons)$ (see Fig. 13a) and in some multihadronic e^+e^- annihilation channels (e.g., see subsection 2.7 The dip in the total multihadronic cross section and the steep variation of the proton form factor near threshold (see Fig. 13) may be fitted with a narrow vector meson resonance, with a mass $M \sim 1.87$ GeV and a width $\Gamma \sim 10$ MeV. The relatively small cross section and width suggest that the couplings of this state to e^+e^- and to multihadronic channels are small. Additional high-statistics, high-mass-resolution e^+e^- annihilation data in the mass range $1.4 < \sqrt{s} < 3$ GeV are clearly needed to confirm these effects, determine the masses and widths of these putative new vector mesons and determine their relationship with the nucleon form factors.

- Overall analytic solution for nucleon form factors: The nucleon form factor in the unphysical region below the $N\overline{N}$ threshold, where the structures discussed above would appear, can in principle be calculated from the space-like form factor using dispersion relations and many such attempts have been made; one such solution is shown in Figs. 14 and 15.

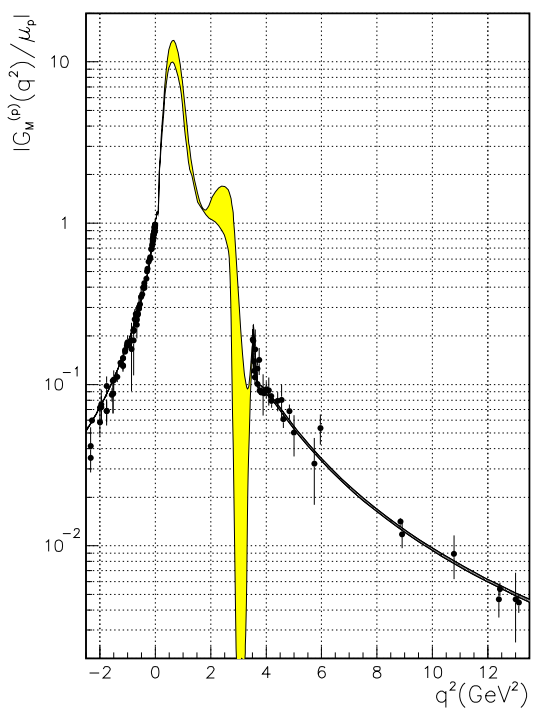

Figure 14: Proton magnetic form factor in the unphysical region from dispersion relations.

Unfortunately, a stable solution cannot be obtained without a huge and unrealistic improvement in statistical accuracy with respect to the existing space-like data. However modestly accurate data in the time-like region will in principle allow a

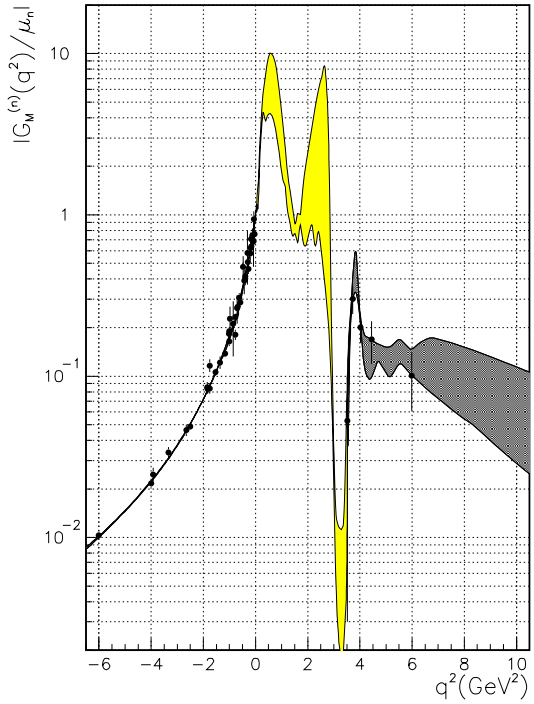

Figure 15: Neutron magnetic form factor in the unphysical region from dispersion relations.

stable solution. A recent evaluation of the magnetic form factors in the unphysical region [77] shows unexpected features, potentially related to structures of the type discussed above, which can realistically be resolved only by new data in the time-like regime.

These considerations strongly support the importance of a new measurement of the neutron and proton time-like form factors with much higher statistics than previous work and with the capability of separately determining the electric and magnetic form factors, especially very close to threshold. Such a new measurement would significantly improve our knowledge of the form factors in the unphysical region and would check the consistency of space-like measurements.

It is worth noting that for the proton form factor, the alternative technique of antiproton annihilation suffers from complications related to stopping $\overline{p}$s in a target [78]. A measurement at a e^+e^- collider avoids these difficulties, albeit at the expense of a smaller cross section.

Near and below the threshold a measurement of the various multihadronic e^+e^- channels is also of great importance to understand if there are indeed $N\overline{N}$ bound states. We propose a statistical accuracy comparable to that achieved in diffractive photoproduction. e^+e^- annihilation provides a much better mass resolution than photoproduction

which is particularly important to a search for narrow structures.

2.4 Other baryon form factors

Nucleon excitation via electron scattering demonstrates three prominent resonant regions, at 1.232, 1.535, and 1.65 GeV. The first is due to the $\Delta(1232)$ resonance, and the other regions each represent the overlap of several resonances. Electron scattering (space-like) data to $Q^2 \sim -20$ (GeV/c)^2 has been analyzed in terms of transition form factors, analogous to the nucleon form factors discussed above [79]. The magnitudes of the transition form factors are comparable to those of the nucleon form factors. Perturbative QCD predicts a $1/Q^4$ behavior for the transition form factors, which is satisfied for the higher mass resonances. However the transition form factor for the Δ resonance falls much faster, approximately at $1/Q^6$, which may be due to suppression of the leading-order pQCD amplitude, leaving higher-order amplitudes dominant.

Time-like data will be important in testing QCD and in resolving the questions raised by the space-like Δ data. There appear to be no existing data. The transition form factors are determined by observing annihilations to nucleon plus baryon resonance. We will have access to the Δ in its $n\pi$ and $N\pi\pi$ decay modes and the $S_{11}(1535)$ in its $N\pi$ and $N\eta$ decay modes. Since the cross sections are expected to be similar, we anticipate uncertainties for the resonance transition form factors that are comparable to those for the nucleon form factors. They will easily be small enough to identify the power of the Q^2 dependence. We are hopeful that the angular distributions and polarization data will allow determination of individual form factors, i.e. charge, dipole, quadrupole, for a more detailed study of hadron structures and of QCD predictions.

The physics of hyperon form factors is analogous to that of nucleon nucleon form factors. Form factors reveal the distribution of charge and magnetization within the hyperons and probe the quark wave functions of these states. Flavor symmetry relates the hyperon form factors to those of the nucleons and accurate prediction of flavor-symmetry breaking is an important test of QCD. At PEP-N we will measure the form factors of the Λ, Σ^0 and charged Σ. We will also determine the $\Lambda - \Sigma^0$ transition form factor, which is different from the $N - \Delta$ form factor discussed above in that the baryons are members of the same SU(3) multiplet.

2.5 Meson form factors

Hadron form factors fall into the category of exclusive reactions at non-asymptotic momentum transfers. Computation of hadron form factors is a critical test of QCD and there is an active program in form factor computation using perturbative QCD, which is expected to be accurate at asymptotic Q^2, but is however not yet fully successful at accessible Q^2. There is active interest in the question of whether these processes can be successfully described by perturbative QCD at experimental Q^2 or whether these fundamental properties of hadrons are intrinsically non-perturbative in this regime [61]. Much of the theoretical attention has been directed at the proton form factor because of its experimental accessibility in both space-like and time-like regimes. However the meson

form factors are intrinsically simpler and may provide more guidance to theory than nucleon form factors (see Appendix II).

For the pion form factor and for the charged and neutral kaon form factors, there is data only at the very small space-like momentum transfers $Q^2 < 0.25 GeV^2$ and for time-like momentum transfers smaller than 1.5 GeV^2. The data above 1.0 GeV^2 is particularly poor. Despite this, a significant amount of sophisticated theoretical work has been done which has not been afforded comparison with experiment. Although significantly better measurements of the pseudoscalar space-like form factors are not likely to be available soon, the fact that analyticity implies that high-statistics measurement of the time-like form factor determines the space-like form factor makes it possible to comprehensively compare experiment with theory.

We are aware of no work, either experimental or theoretical, on form factors of vector mesons. Successful prediction of pseudoscalar and vector meson form factors are necessary elements of a comprehensive description of hadron structure. The PEP-N experiment will have the capability of observing formation of pairs of charged pions, charged rho mesons and charged and neutral K and K* mesons. It will have the capability of making precise measurement of the electromagnetic form factors for these hadrons in the (time-like) regime 1.4 GeV $< \sqrt{s} <$ 2.5 GeV.

A closely related area is the 3-point coupling of a vector meson, pseudoscalar meson and photon, manifested in e^+e^- annihilation to $\rho\pi$, $\omega\pi^0$, $\phi\pi^0$, analogous reactions with η's, and annihilation to K^*K, each dependent on an s-dependent transition form factor. These fundamental processes are potentially amenable to perturbative QCD in this regime.

2.6 1^{--} spectroscopy

A hadron pair made in electron positron annihilation is necessarily in a neutral 1^{--} state and these reactions therefore constitute the simplest arena in which to study 1^{--} states, as it is straightforward to determine the reaction amplitude. An analysis of this type was carried out by Donnachie and Mirzaie [80], who found evidence for the $\rho(1450)$ and $\rho(1700)$. Exclusive multihadron channels may also be analyzed for the formation of vector mesons as described below. The PEP-N experiment will generate high-statistics data in channels containing multiple π and K mesons that can be analyzed for the formation of heavy ρ, ω, and ϕ mesons.

The current status of the vector meson spectroscopy is as follows:

- All main states of $q\overline{q}$ systems are established.
- Charmonium and bottomonium families are farily well known.
- Excitation states of the $q\overline{q}$ systems for u, d, s quarks are not well established.
- There are indications for existence of $K\overline{K}$ or 4-quark states in the vector meson decays [81, 82, 83, 84].
- There are indications for existence of $N\overline{N}$ or 6-quark states [76].

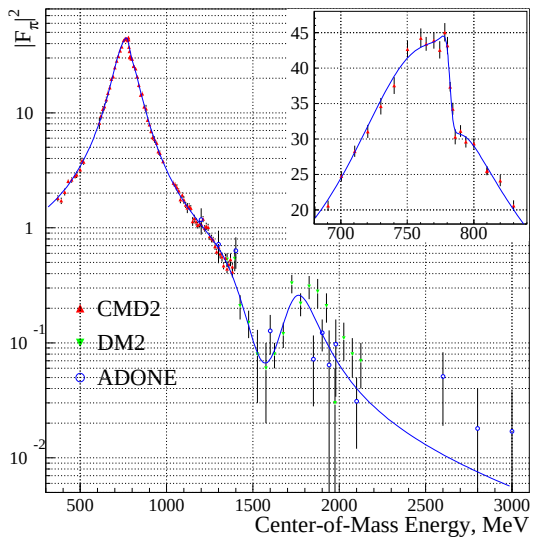

Figure 16: The $e^+e^- \to \pi^+\pi^-$ cross section.

The main problems of light vector meson spectroscopy arise from the fact that in the mass region 1.4 to 2.5 GeV only a total integrated luminosity $\simeq 2$ pb^{-1} was collected at DCI and ADONE. The corresponding statistics are inadequate compared with data collected in the energy regions of the charmonium and bottomonium families. In contrast, in the low energy region from the hadron production threshold to 1.4 GeV, systematic studies have been performed in Novosibirsk at the e^+e^- collider VEPP-2M, which was in operation from 1974 to 2000 and a total integrated luminosity $\simeq 80$ pb^{-1} was collected. Important measurements were done by OLYA [85, 86] and ND [87] experiments, but the major share of integrated luminosity was taken by the CMD-2 [88] and SND [89] experiments. The experimental program is now finished and final data analysis is in progress.

2.6.1 Light Vector Mesons

The main advantages of experiments on vector meson production in e^+e^- annihilation are the clean initial state with well defined quantum numbers, high mass resolution and good conditions for study of exclusive reactions. The main problems of the e^+e^- data analysis derive from uncertainties in the interference between several resonances, which often introduces model dependence into final results (see for example [90]). There are also model dependences of the data analysis [91]-[95], which can be resolved only with significant increase of experimental statistics. In this section, we review the status of spectroscopy in the low energy and 1 - 2 GeV regions, and we note the sharp contrast between the quality of the available data above and below $E_{cm} = 1.4$ GeV.

a. $e^+e^- \to \pi^+\pi^-$

Precise measurements of the two pion production cross section have been performed

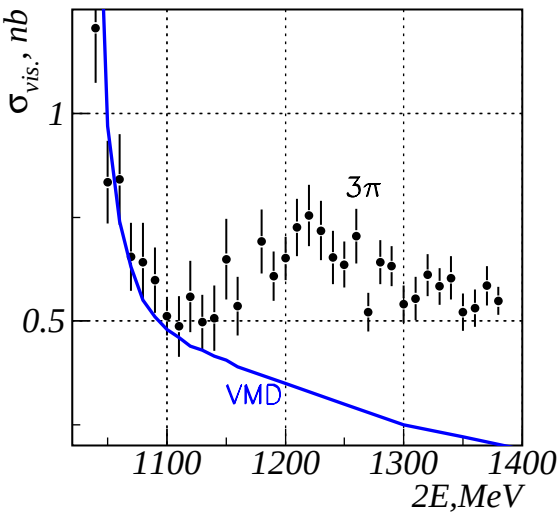

Figure 17: Visible cross section of the reaction $e^+e^- \to \pi^+\pi^-\pi^0$ [103].

for many years [86, 96, 97]. The systematic uncertainty of 0.6 % was achieved in the last CMD-2 experiment [98] in the energy range below 1 GeV. For higher energies the results are not so precise, but DM2 data [99] strongly emphasize the signal of $\rho(1700)$ (Fig.16). There is a wide enhancement in the the cross section around 1.25 GeV which may be taken as an evidence for the $\rho(1250)$ resonance, but at the same time other models have been discussed [92, 100].

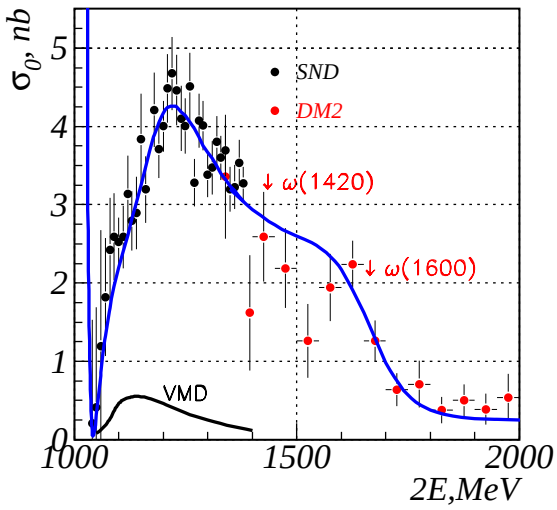

Figure 18: The $e^+e^- \to \pi^+\pi^-\pi^0$ cross section.

b. $e^+e^- \to \pi^+\pi^-\pi^0$

The main contributions to the three pion production cross section at low energy come from the $\omega(782)$ and $\phi(1020)$ resonances. It is well known that the interference between

these resonances is destructive [90]. For many years, in the energy region above 1 GeV, the experimental data were not precise [87, 101]. The last SND measurement [103] shows that there is a visible peak in the cross section at 1.25 GeV (Fig.17). After applying radiative corrections and detection efficiencies, total cross sections were obtained in which a clear resonance signal is seen. Taking into account the data below 1 GeV and the DM2 data [101] a set of fits was performed [103]. The best fit (Fig.18) requires contributions of ω, ϕ, $\omega(1200)$, and $\omega(1650)$ with the relative phases (+), (-), (-), (+).

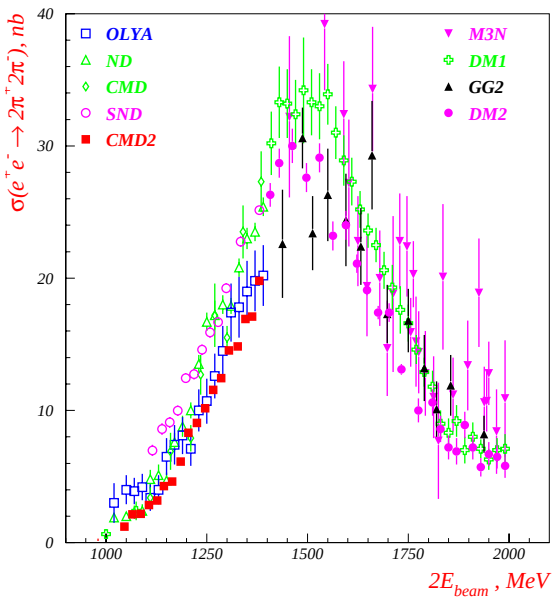

Figure 19: The $e^+e^- \to \pi^+\pi^-\pi^+\pi^-$ cross section [102].

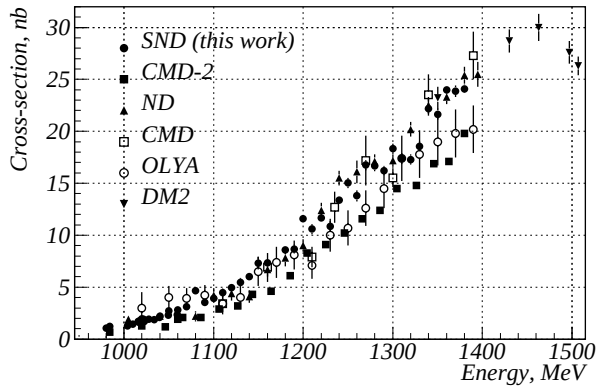

Figure 20: The $e^+e^- \to \pi^+\pi^-\pi^+\pi^-$ cross section with the recent VEPP-2M data [105].

c. $e^+e^- \to \pi^+\pi^-\pi^+\pi^-$

Four charged pion production (Fig.19) has been studied by many groups [97]. The most detailed investigations have been reported by CMD-2 [104]. In this work a partial wave analysis was performed, showing that the $a_1(1260)\pi$ intermediate state dominates

in the energy region below 1.4 GeV. The SND results [105] confirm the CMD-2 data (Fig.20).

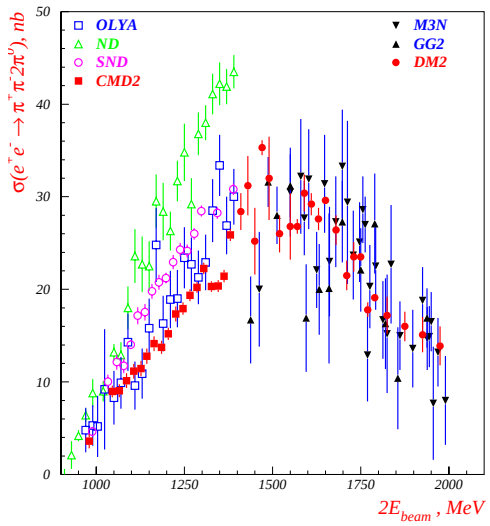

Figure 21: The $e^+e^- \to \pi^+\pi^-\pi^0\pi^0$ cross section [102].

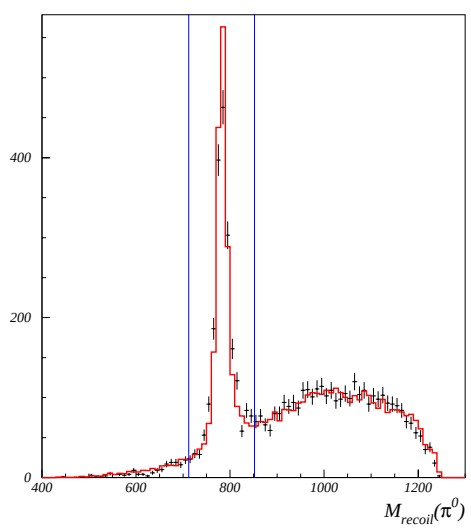

Figure 22: The invariant mass of $\pi^+\pi^-\pi^0$ in the reaction $e^+e^- \to \pi^+\pi^-\pi^0\pi^0$ [104].

d. $e^+e^- \to \pi^+\pi^-\pi^0\pi^0$

The $e^+e^- \to \pi^+\pi^-\pi^0\pi^0$ cross section has been studied in many experiments (Fig.21). The agreement between different groups is poor because of experimental problems and because of unclear process dynamics [106]. Some progress was achieved in the recent Novosibirsk experiments at low energy. Using a partial wave analysis of the reaction $e^+e^- \to \pi^+\pi^-\pi^0\pi^0$, CMD-2 found [104] that $a_1(1260)\pi$ and $\omega\pi^0$ intermediate states dominate the reaction mechanism (Figs.22 and 23). The recent SND data [105] are in

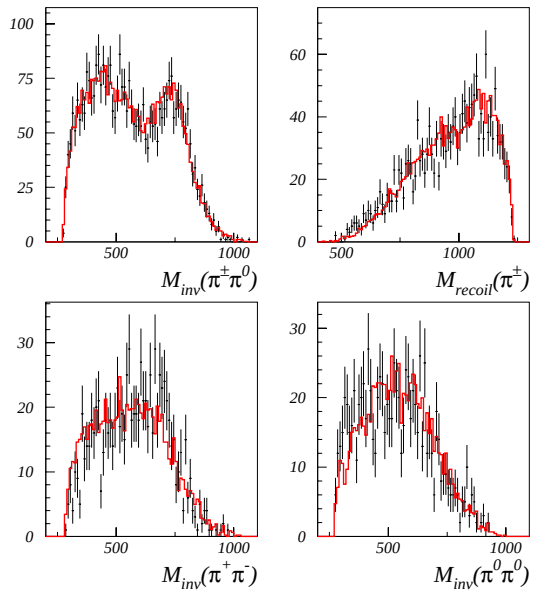

Figure 23: The two pions invariant mass in the reaction $e^+e^- \to \pi^+\pi^-\pi^0\pi^0$ [104].

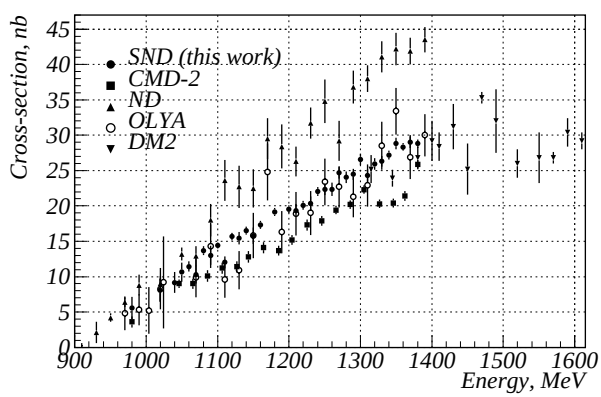

Figure 24: The $e^+e^- \to \pi^+\pi^-\pi^0\pi^0$ cross section with the recent VEPP-2M data [105].

agreement with the CMD-2 results within the systematic uncertainty of the experiments (Fig.24). But until now the systematics of these experiments is significantly higher than statistical accuracy.

e. $e^+e^- \to \pi^+\pi^-\pi^+\pi^-\pi^0$

The five pion production cross section has been studied by CMD-2 [107] and DM2 [101]. It has been shown that tree diagrams (Figs.25, 26) dominate in these reactions. In the $\omega\pi^+\pi^-$ cross section, the clear peak of the $\omega(1650)$ is seen and there is probably some contribution of the $\omega(1200)$ (Fig. 27). In the $\eta\pi^+\pi^-$ reaction the clear peak of $\rho(1450)$ determines the cross section shape but some contribution of $\rho(1700)$ is not excluded (Fig. 28).

f. $e^+e^- \to \omega\pi^0$

The main reaction channel $e^+e^- \to \omega\pi^0 \to \pi^+\pi^-\pi^0\pi^0$ is seen in the four pion final state but a smaller systematic uncertainty in the cross section measurement was achieved by SND using the $e^+e^- \to \omega\pi^0 \to \pi^0\pi^0\gamma$ reaction [108]. Combining SND data with the data of DM2 [109] and CLEOII [110] the fit of the cross section was performed (Fig.29). It should be noted that there is a systematic bias between the DM2 and CLEOII data, which can be connected with a normalization problem or with a bias in the energy scale.

g. $e^+e^- \to \eta\gamma$

The first indication of a radiative decay of radial excitations of light vector mesons was found by CMD-2 [111]. Two events of the reaction $e^+e^- \to \eta\gamma$ were identified. The estimated production cross section is in agreement with the data of CMD-2 [107] and DM2 [112] for the reaction $e^+e^- \to \eta\pi^+\pi^-$.

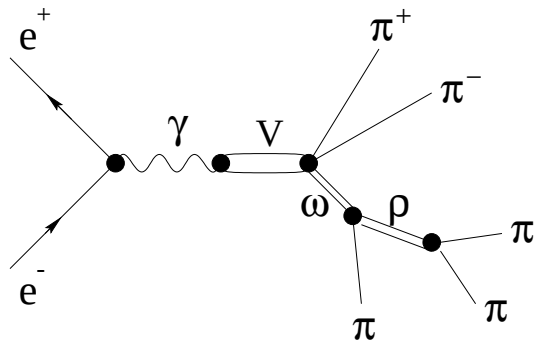

Figure 25: The $e^+e^- \to \omega\pi^+\pi^-$ main diagram.

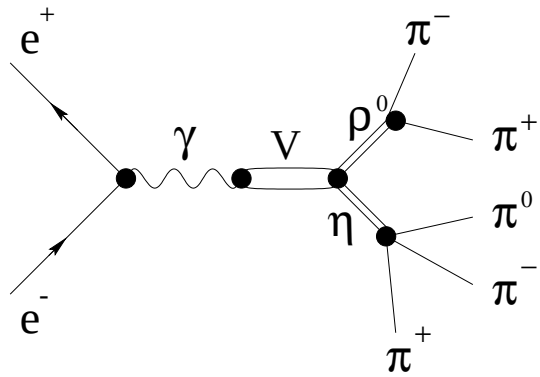

Figure 26: The $e^+e^- \to \eta\pi^+\pi^-$ main diagram.

h. $e^+e^- \to K_SK_L, K^+K^-$

The preliminary SND results on the cross section $e^+e^- \to K_SK_L$ [90, 113] together with the DM1 data [114] can be successfully fitted if the contributions of the ρ, ω, ϕ, and $\phi(1680)$ resonances are taken into account (Fig.30). The data on the reaction $e^+e^- \to K^+K^-$ [85, 115] are in agreement with such a model.

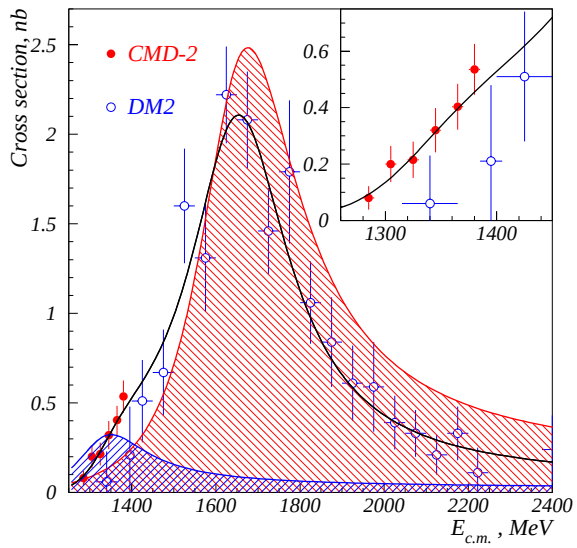

Figure 27: The $e^+e^- \to \omega\pi^+\pi^-$ cross section.

i. $e^+e^- \to KK\pi$

A partial wave analysis of the $e^+e^- \to KK\pi$ reaction has been performed by DM2 [116]. It was shown that the isoscalar process $\phi(1680) \to K^*K \to K_S K^\pm \pi^0$ dominates. The cross section $e^+e^- \to K^+K^-\pi^0$ is small. The 1.45 GeV vector state observed in the hadron production [117] is not confirmed in the e^+e^- production at VEPP-2M [113, 118].

2.6.2 The Light Vector Meson Spectrum

$N^{2S+1}L_J$	$(u\overline{u} - d\overline{d})/\sqrt{2}$	$(u\overline{u} + d\overline{d})/\sqrt{2}$	$s\overline{s}$
1^3S_1	$\rho(770)$	$\omega(782)$	$\phi(1020)$
2^3S_1	$\rho(1450)$	$\omega(1420)$	$\phi(1680)$
1^3D_1	$\rho(1700)$	$\omega(1650)$	-
3^3S_1	$\rho(2150)$		

Table 3: The classification of vector mesons by PDG'00.

The classification (Table 3) of the light vector mesons proposed by PDG [97] is still subject to some controversy. Some of the resonances included in the table are not well established, and data on other states are ignored. The difficulty of the existing data analysis is connected with the low statistical accuracy of the data above 1.4 GeV. Moreover, the model uncertainty of resonance masses and widths may exceed 200 MeV [95]. The quality of the experimental data is reported in Table 2.6.2 and the following conclusions can be drawn after review of the current data:

	$\rho(1250)$	$\omega(1200)$	$\rho(1450)$	$\omega(1420)$	$\rho(1700)$	$\omega(1650)$	$\phi(1680)$	$\rho(2150)$
$e^+e^- \to \pi^+\pi^-$	*		*		+			*
$e^+e^- \to \pi^+\pi^-\pi^0$		+		*		*	*	
$e^+e^- \to 4\pi$			+		+			
$e^+e^- \to \omega\pi^0$			*		+			
$e^+e^- \to \omega\pi^+\pi^-$		*		*		+	*	
$e^+e^- \to \eta\pi^+\pi^-$			+		*			
$e^+e^- \to \eta\gamma$			*					
$e^+e^- \to K_S K_L$					*		+	
$e^+e^- \to K^+K^-$					*	*	*	+
$e^+e^- \to K^*K$					*		+	
$e^+e^- \to K^+K^-\pi^0$							*	
$\pi^-p \to \omega\pi^0 n$								+
$\pi^-p \to \phi\pi^0 n$					*			
$p\overline{p}, \overline{p}n \to hadrons$	*		*		+			
$\gamma p \to hadrons$	*				+			

Table 4: The level of experimental significance of the vector mesons in selected reactions: + - well established states, * - not well established states.

- $\rho(1250)$ is ignored by PDG but, as pointed out by D. Peaslee [119] there are several old and new experiments (OMEGA [120], LASS [121], OBELIX [122, 123]) in which some evidence for the $\rho(1250)$ was obtained.
- $\omega(1200)$ is identified by $\pi^+\pi^-\pi^0$ cross section [103].
- $\rho(1450)$ is identified by $\pi^+\pi^-\pi^+\pi^-$ and $\eta\pi^+\pi^-$ production in e^+e^- and in $p\overline{p}$ experiments.
- $\omega(1420)$ is not well established.
- $\rho(1700)$ is seen in the e^+e^- production in $\pi^+\pi^-$, $\omega\pi^0$, and $\pi^+\pi^-\pi^0\pi^0$ final states. It is identified in the gamma production [97] and in the $p\overline{p}$ production [124, 125].
- $\omega(1650)$ is identified by $\omega\pi^+\pi^-$ cross section [101].
- $\phi(1680)$ is identified by the K^*K cross section [116].
- $\rho(2150)$ is identified in the hadron production of $\omega\pi^0$ by GAMS [126].

2.6.3 Prospects

A number of questions must be answered to clarify the situation with respect to the excited states of the light vector mesons. PEP-N can contribute significantly to many of these issues:

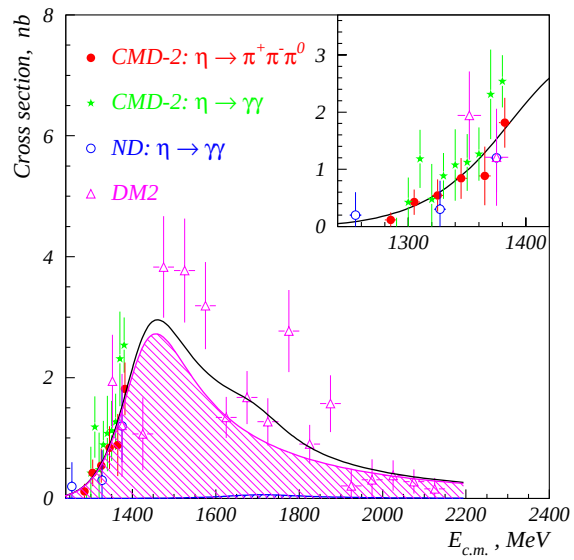

Figure 28: The $e^+e^- \to \eta\pi^+\pi^-$ cross section.

- Does $\rho(1250)$ exist? What is the nature of this object? It is the 2^3S_1 $q\overline{q}$ state or is it the lowest 4-quark vector state?
- Is $\omega(1200)$ a 2^3S_1 $q\overline{q}$ state or is it the lowest 4-quark vector state?
- Does $\omega(1420)$ exist?
- $\rho(1700)$, $\omega(1650)$, and $\phi(1680)$ have practically the same mass. They must have common decay channels, so cross section shapes are modified because of the interference. Are there three resonances $\rho(1700)$, $\omega(1650)$, and $\phi(1680)$ or are there only two?
- Do other light quark states exist?

To resolve these issues one needs an e^+e^- collider experiment with good efficiency and particle identification in the relevant energy region. Other methods or other existing facilities have the following limitations:

- DAΦNE is in principle capable of reaching 1.4 GeV. The design maximum energy of VEPP-2000 [127] is 2 GeV. Otherwise there is no e^+e^- facility operational or planned for this regime.
- Hadronic τ decays are useful for isovector and vector meson spectroscopy only up to 1.7 GeV.
- The Initial State Radiation method [128, 129] is effective but limited in mass resolution and in statistics, especially for low cross section channels like the isoscalars ones.

- Experience indicates that experiments using hadronic and γ interactions, or $p\overline{p}$ annihilations can not compete with e^+e^- experiments for precise vector meson spectroscopy.

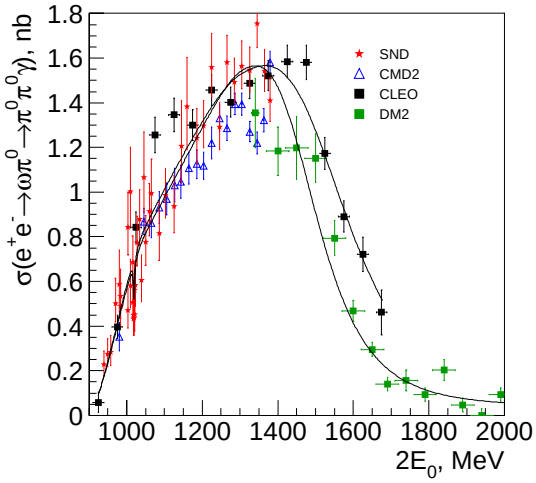

Figure 29: The $e^+e^- \to \omega\pi^0$ cross section.

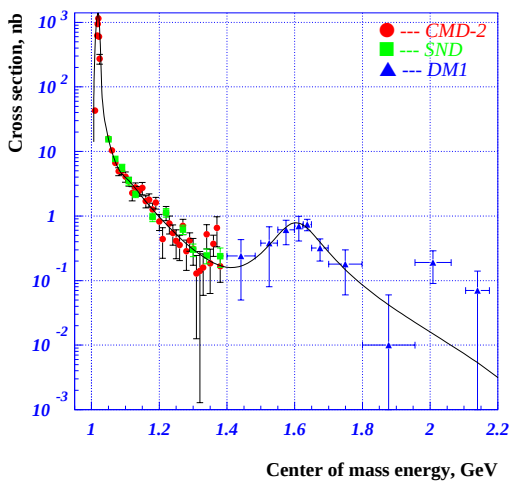

Figure 30: The $e^+e^- \to K_S K_L$ cross section.

2.7 Search for non $q\overline{q}$ states in PEP-N

The present knowledge of the established meson states shows the basic validity of the constituent quark model, even if many $q\overline{q}$ states remain to be discovered or are poorly known. Nevertheless, some discrepancies with the predictions of the quark model are present, mostly in the 1.5-2.5 GeV mass region, and point to the need to go beyond the

search for pure $q\overline{q}$ states: the non-Abelian nature of QCD does not exclude hadronic states made of valence gluons (glueballs) or valence gluons and quarks (hybrids) or multiquark states (like $N\overline{N}$ bound states). This search has been going on from more than 20 years but until now no fully established candidate has been identified.
The best way to look for new vector mesons is in e^+e^- annihilation, where only a small integrated luminosity has been collected in the past in the PEP-N mass range. The other way to look for vector mesons is diffractive photoproduction with high energy incident photons. High statistics data have been collected by E687 and FOCUS at FNAL. In their data there is strong evidence of new vector mesons (perhaps an entire family of new vector mesons, weakly coupled to the photon). Of course diffractive photoproduction is limited by the unavoidable non diffractive background and by the detector mass resolution, affecting narrow structures. With a much higher luminosity in e^+e^- , we can foresee an improvement in this search of one or two orders of magnitude.

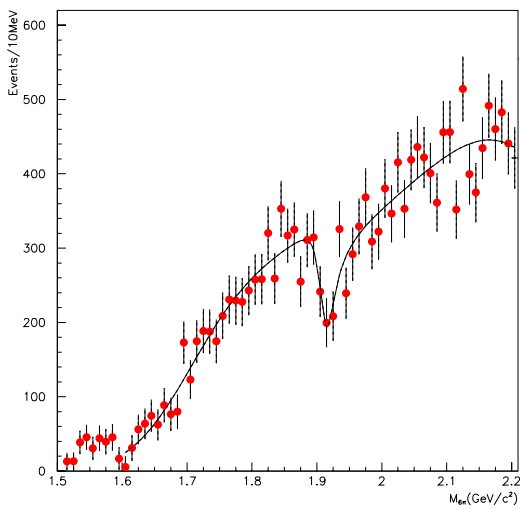

Figure 31: $3\pi^+3\pi^-$ invariant mass distribution in high energy diffractive photoproduction by FNAL/E687. The mass resolution has been unfolded and a $1/M$ factor is applied to the E687 data to facilitate comparison with e^+e^-.

2.7.1 Hybrid spectroscopy at PEP-N

Hybrid masses and decays are usually calculated using the flux tube model, [130, 131], where the hybrid new degree of freedom is identified in the excitation of the color flux tube connecting the valence quarks. It is remarkable that this model predicts non strange hybrids all clustered at ~ 1.9 GeV and strange ones at ~ 2.1 GeV. The same prediction has been obtained by lattice calculations [132, 133, 134]. Furthermore, the way the string breaks forbids decay into two identical mesons and correlates spin and parity of the decay products [135]. For instance, a vector hybrid is allowed to decay into $a_1\pi$ and forbidden to decay into $h_1\pi$. Because of these selection rules in the two body decay, high multiplicity

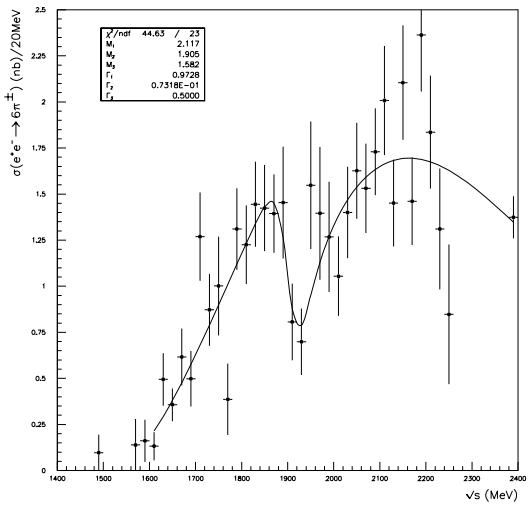

Figure 32: Cross section for $e^+e^- \to 3\pi^+3\pi^-$ by DM2.

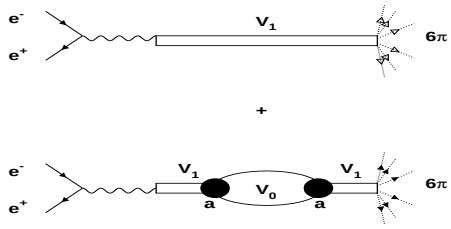

Figure 33: Diagram describing the e^+e^- annihilation via a V_0, V_1 interference term contribution.

channels should be favored and a relatively small width can be expected. Looking for vector hybrids in e^+e^- has significant advantages:

- quantum numbers $J^{PC} = 1^{--}$ are naturally selected in e^+e^- annihilation;
- there is no glueball/hybrid ambiguity, because the lightest vector glueball is expected at ~ 4 GeV [136, 137];
- small, but non-vanishing, e^+e^- widths are expected;
- aforementioned selection rules forbid many channels, in particular simple channels like two equal mesons; as a consequence a small total width is expected and high multiplicity channels should be favoured.
- in case of a small total width they are seen as a dip in the cross section, as will be shown in the following.

The $\rho(1450)$ has been suggested as a hybrid candidate mixed with nearby S and D wave $q\overline{q}$ states, because it decays mostly into $a_1\pi$ and not into $h_1\pi$ [138][139]. Evidence for a $\rho(1450)$ comes mostly from $e^+e^- \to 2\pi^+2\pi^-$. The fact that $e^+e^- \to \pi^+\pi^-2\pi^0$ is wider at high masses is considered evidence for a further $\rho(1700)$. This is very compelling evidence for some hybrid in this mass region, although the width of the $\rho(1450)$ bump, $\Gamma \sim 300$ MeV, is still quite large and the cross section is quite large for a hybrid, i.e., the largest in e^+e^- annihilation at these energies.

The mass region around 2 GeV, where vector hybrids are expected, is nearly unexplored. However in diffractive photoproduction of $3\pi^+3\pi^-$ there is a narrow dip at $\sim$ 1.91 GeV (Fig. 31), obtained by E687 [140] in agreement with $e^+e^- \to 3\pi^+3\pi^-$ data obtained by DM2 (Fig. 32) [141].

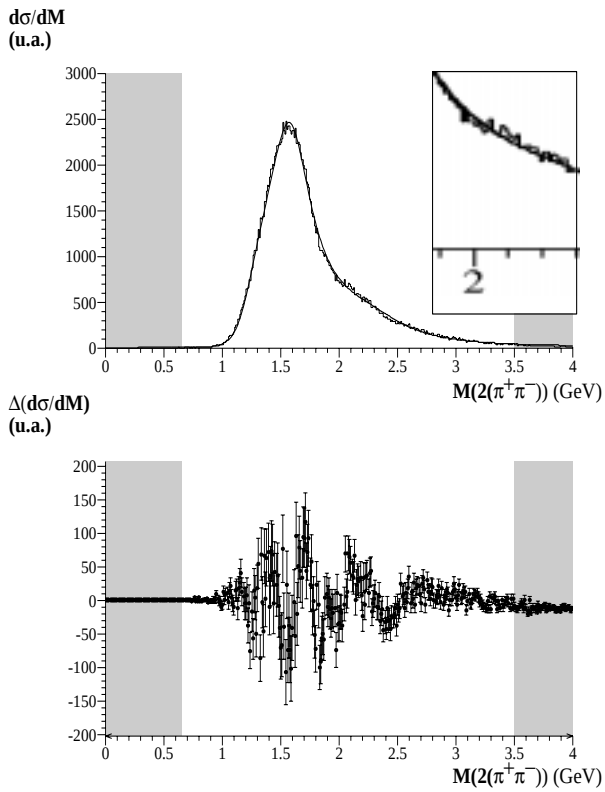

Figure 34: Acceptance corrected $2(\pi^+\pi^-)$ mass (top) and residual (data - fitted values) distributions (bottom).The solid line is the 3 P-Wave Breit-Wigner fit.

This dip could be the long awaited indication of a vector isovector hybrid according to the simple model shown in Fig. 33 and demonstrated in a different context in [142]. Let us assume that the mass region of the E687 dip is populated by broad and prominent ρ recurrences (V_1 resonances) and there is a V_0 resonance with a small production cross

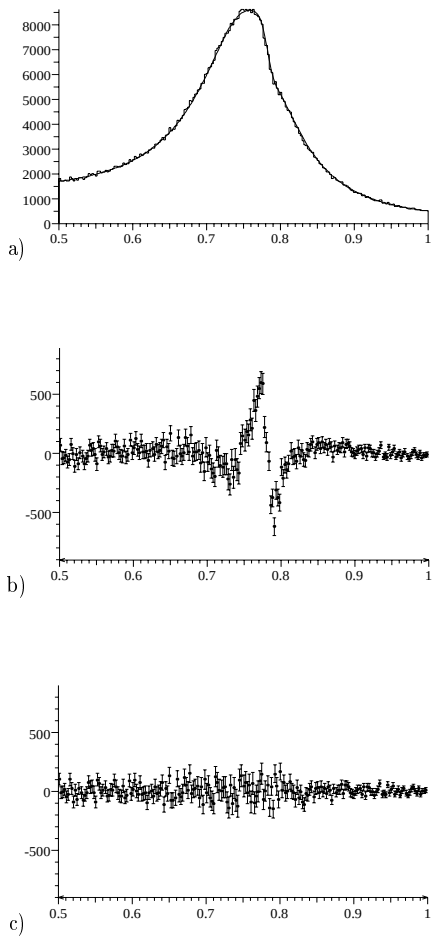

Figure 35: a. the $M_2\pi$ spectrum in the range 0.5-1.0 GeV/c^2, around the $\rho(770)-\omega(783)$ pole mass (top); b. residual (fit-data) once the mixing amplitude is fixed to 0; c. residuals (fit-data) when the interfering amplitude is included.

section. In the extreme limit of full mixing, the corresponding amplitude is given by:

$$A \propto \frac{1}{M^2 - M_1^2} \cdot (1 + a\frac{1}{M^2 - M_0^2} a \frac{1}{M^2 - M_1^2} + ...)$$

$$\propto \frac{M^2 - M_0^2}{(M^2 - M_1^2)(M^2 - M_0^2) - a^2}.$$

Here M^2 is the six pion invariant mass squared, the complex number M_1 stands for the mass and width of any ρ recurrence V_1 near by, M_0 is the same for the narrow resonance V_0 and a is the V_1V_0 coupling constant. This amplitude, with a zero at the unmixed V_0 mass pole in the limit of negligible unmixed width, will produce a narrow dip at $\sqrt{s} \sim M_0$ in the cross section, consistent with what has been observed in the E687 analysis (Fig. 31).

If this interpretation is right, other decay channels have to be identified. Furthermore the isoscalar vector partner, whose production cross section is expected lower than that of the isovector, has to be identified. The aforementioned dip in the total cross section

and the present dip in the $3\pi^+3\pi^-$ channel are separated by 30 MeV. Further data are required to clarify this situation: on one hand it is unlikely that there is a 30 MeV shift in the two energy scales, on the other hand the presence of two similar dips nearby is puzzling.

Evidence for further, unexpected, resonances (maybe an entire new family) comes from results of E687 in diffractive photoproduction of $2(\pi^+\pi^-)$ and preliminary results from FOCUS show the same behaviour [143]. This experiment has collected more than one million diffractively photoproduced $2(\pi^+\pi^-)$ events in a fixed target experiment at FNAL. The acceptance corrected mass spectrum, shown in Fig. 34(top), is dominated by the $\rho(1450)$ vector meson, but the fit (solid line) is not good even when 3 interfering P-wave Breit-Wigner resonances are added coherently: the χ^2 is 467.0 for 274 degrees of freedom. As the acceptance is almost flat for $M_{4\pi} \sim 1.6$ GeV, the many interfering resonance patterns observed in the residual distribution in Fig. 34(bottom) could be of physical origin. The same experiment has very nice evidence of the $\rho - \omega$ mixing effect when plotting the same quantities, data - fitted values (Fig. 35b), for 2π final states[144]. There is no evidence of further interfence patterns in the 2π mass spectrum. A hint for the interpretation of this 4π unexpected pattern could come from the observation that the ratio of the residuals to the total yield in 4π is of the same order of the $\rho - \omega$ mixing effect in 2π[144]. Only high integrated luminosity can look for such a pattern in the cross section. The luminosity forseen in PEP-N should be adequate.

2.8 $\gamma\gamma^*$ and $\gamma^*\gamma^*$ interactions

$\gamma\gamma^*$ interactions are obtained by studying hadroproduction in e^+e^- scattering. Meson production and production of particle-antiparticle pairs in both single-tag and double-tag modes constitute tools for studying the quark-gluon structure of the hadrons and testing the capabilities of QCD in its various formulations. The initial theoretical work in this area was the calculation of single pseudoscalar meson production by Brodsky and Lepage [56] in the Light Cone Approach. Good agreement with theory was observed for $\gamma\gamma^*$ production of π^0 η, and η' (i.e. the pseudoscalar meson-photon transition form factor) in experiments at CLEO [145].

Work in perturbative QCD [146] has shown that the process $\gamma\gamma^* \to h\bar{h}$ in the kinematical domain $W^2 << Q^2$, the continuation of deeply virtual Compton scattering from hadrons, where W^2 is the center of mass energy and Q^2 is the γ^* virtuality, factorizes into a calculable hard scattering amplitude to partons (quark-antiquark or gluon-gluon)and a non-perturbative amplitude for hadronization. The production of a pair of pseudoscalar mesons has been calculated.

In the PEP-N kinematic regime, the processes satisfying the condition $W^2 << Q^2$ are: $\gamma\gamma^* \to \pi^0$ and $\gamma\gamma^* \to \pi^+\pi^-$. The former has been measured[145]. Study of the latter process at PEP-N will supply a description of the $q\bar{q} \to \pi\pi$ process at energies and momentum transfers that are germane to hadroproduction at hadron and electron-positron colliders as well as at neutrino experiments. A further interesting aspect is to test the scaling in Q^2 (the analog of Bjorken scaling for this channel). The helicity structure of the process is predicted by pQCD and can be obtained from the two-pion

angular distribution.

Recently, it has been pointed out that one can study the $\gamma\gamma^* \to \pi\pi$ process (one offshell photon) at the amplitude level through the interference term between $\gamma\gamma^*$ and bremsstrahlung(where a single photon forms a $\pi^+\pi^-$ pair, mainly through intermediate ρ production) subprocesses [147, 148]. One can then completely distinguish the amplitudes A_{++}, A_{+-}, and A_{0+} for different photon helicities. In the kinematical region where the bremsstrahlung is large, the interference term gives the relative phase of these amplitudes with respect to the phase of the pion form factor, known to be the $\pi\pi$ phase shift δ_1.

The $\gamma\gamma^*$ reaction produces $\pi^+\pi^-$ in the C-even channel, and bremsstrahlung leads to $\pi^+\pi^-$ in the C-odd channel. The interference determines the charge asymmetry of the process and disappears when averaged over the pion charge. The interference term can be separated from the pure $\gamma\gamma^*$ and bremsstrahlung contributions in two different ways : 1) It can be obtained by reversing the charge of the lepton in the $e\gamma$ collisions; this can be done with e^+e^- colliders by measuring $\sigma(e^-\gamma \to e^-\pi^+\pi^-) - \sigma(e^+\gamma \to e^+\pi^+\pi^-)$.
2) Alternatively the measurement of the difference between the number of π^+ and π^- mesons makes it possible to measure this interference term.

The time-like pion form factor in the bremsstrahlung term gives the relative weight of the different contributions. It leads to an enhancement of the interference term in a broad energy interval near the ρ mass. For this reason, this process should be investigated in the regime where the invariant mass W of the $\pi^+\pi^-$ system is close to that of the ρ.

Good statistics in a single tag photon mode are available at relatively small Q^2, where the bremsstruhlung process is large and therefore the interference substantial and measurable. The cross section of the process is $\sim$ 8000 fb. The left-right charge asymmetry of the pion pair projects out the interference term [147], yielding a $\sim$ 300 fb cross section (where we have taken $Q^2 > 1$ GeV^2, 300 MeV $<$ W $<$ 1 GeV, the scattering angle of the tagged lepton $<$ 100 mrad, and p_t <500 MeV for the untagged lepton).

The $\pi^0\pi^0$ final state has only a $\gamma\gamma^*$ contribution and therefore no interference. The cross section is $\sim$ 20 fb in the same kinematic region.

Pion pair, kaon pair, proton antiproton and neutron antineutron production for $W^2 \sim Q^2$ are potentially accessible at PEP-N. Although the dynamics in this domain are different from those discussed above, these processes are amenable to the predictions of pQCD and have been analyzed in detail by Brodsky and Lepage [56]. One particularly important topic is pion pair production where the angular dependence of the ratio of $\pi^+\pi^-$ and $\pi^0\pi^0$ differential cross sections gives the dependence of the distribution amplitudes on x, the fraction of the pion momentum carried by the partons.

2.8.1 Exclusive production of Photon Photon into Baryon Antibaryon Pairs

The exclusive production of baryon-antibaryon pairs ($B\overline{B}$) in the collision of two quasi real photons can be used to test QCD predictions. The photons are emitted by the beam electrons and positrons and the $B\overline{B}$ are produced in the process $e^+e^- \to e^+e^-\gamma\gamma \to e^+e^-B\overline{B}$.

The application of QCD to exclusive two-photon reactions is based on the work of Brodsky and Lapage [56]. According to their formalism the process is factorized into a non-perturbative part and a perturbative part. A calculation based on this

ansatz [149, 150] uses a specific model of the proton's three-quark wave function by Chernyak and Zhitnitsky [151]. This calculation predicts cross-sections that are about one order of magnitude smaller than the existing experimental results [152-157], for two-photon center-of-mass energies W greater than 2.5 GeV. Also $\gamma\gamma \to \Lambda\Lambda$ is not in agreement with these expectations, especially with respect to $\gamma\gamma \to p\overline{p}$, appearing almost the same. A crucial test of the theory would be the measurement of $\gamma\gamma \to n\overline{n}$, never done until now.

To model non-perturbative effects, the introduction of diquarks has been proposed [158]. Within this model, baryons are viewed as systems of quarks and diquarks, quasi-elementary constituents which partially survive medium-hard collision. Their composite nature is taken into account by diquark form factors. Recent studies [159] have extended the investigation of exclusive reactions within the diquark model to two-photon reactions [160, 161, 162, 163].

The quark-diquark model seems to work rather well for exclusive reactions in the space-like region [161, 164, 165]. The calculations of the integrated cross-sections for the process $\gamma\gamma \to p\overline{p}$ in the angular region $|\cos\theta^*| < 0.6$, θ^* here is the the polar angle of the $\gamma\gamma$ centre-of-mass system (cms), appears in agreement with the existing data [152]-[157], which are summarized in Table 5.

e^+e^- Experiments	Year	E_{Beam} (GeV)	Integrated Luminosity (pb^{-1})	$W_{\gamma\gamma}$ (GeV)	Number of $p\overline{p}$ events
TASSO (DESY)	1982	$15 - 18.3$	19.685	$2.0 - 2.6$	8
TASSO (DESY)	1983	17	74	$2.0 - 3.1$	72
JADE (DESY)	1986	$17.4 - 21.9$	$59.3 + 24.2$	$2.0 - 2.6$	41
TPC/2γ (SLAC)	1987	14.5	75	$2.0 - 2.8$	50
ARGUS (DESY)	1989	$4.5 - 5.3$	234	$2.6 - 3.0$	60
CLEO (CESR)	1994	5.29	1310	$2.0 - 3.25$	484
VENUS (TRISTAN)	1997	$57 - 64$	331	$2.2 - 3.3$	311
PEP-N (SLAC)	-	$0.771_{(VLER)}$ $3.115_{(LER)}$	200	$1.9 - 3.1$	200

Table 5: The experiments that have measured the $\gamma\gamma \to p\overline{p}$ cross section in e^+e^- collision; the table gives the beam energy, the integrated luminosity, the range of W and the total number of $p\overline{p}$ events. The last line summarizes the expectations for PEP-N which will be able to see also a comparable number of $n\overline{n}$ events.

To understand the possibility of selecting 2γ events and in particular $\gamma\gamma \to p\overline{p}$ events at PEP-N, preliminary Monte Carlo distributions have been studied. Some quantities are plotted in Figure 36. The $\gamma\gamma \to p\overline{p}$ Monte Carlo events have been simulated with the Galuga [166, 167] generator within a range of W between 2 and 3.1 GeV. Due to the beam asymmetry the $\gamma\gamma$ cms receives a larger boost compared to a symmetric e^+e^- machine and therefore the momenta of the final state particles are larger. Figure 36 (top left) shows that the proton momentum distribution varies between $0.6 - 2.0$ GeV instead e.g. of the range $0.4 - 1.0$ GeV observed for the proton momenta in other experiments [152,

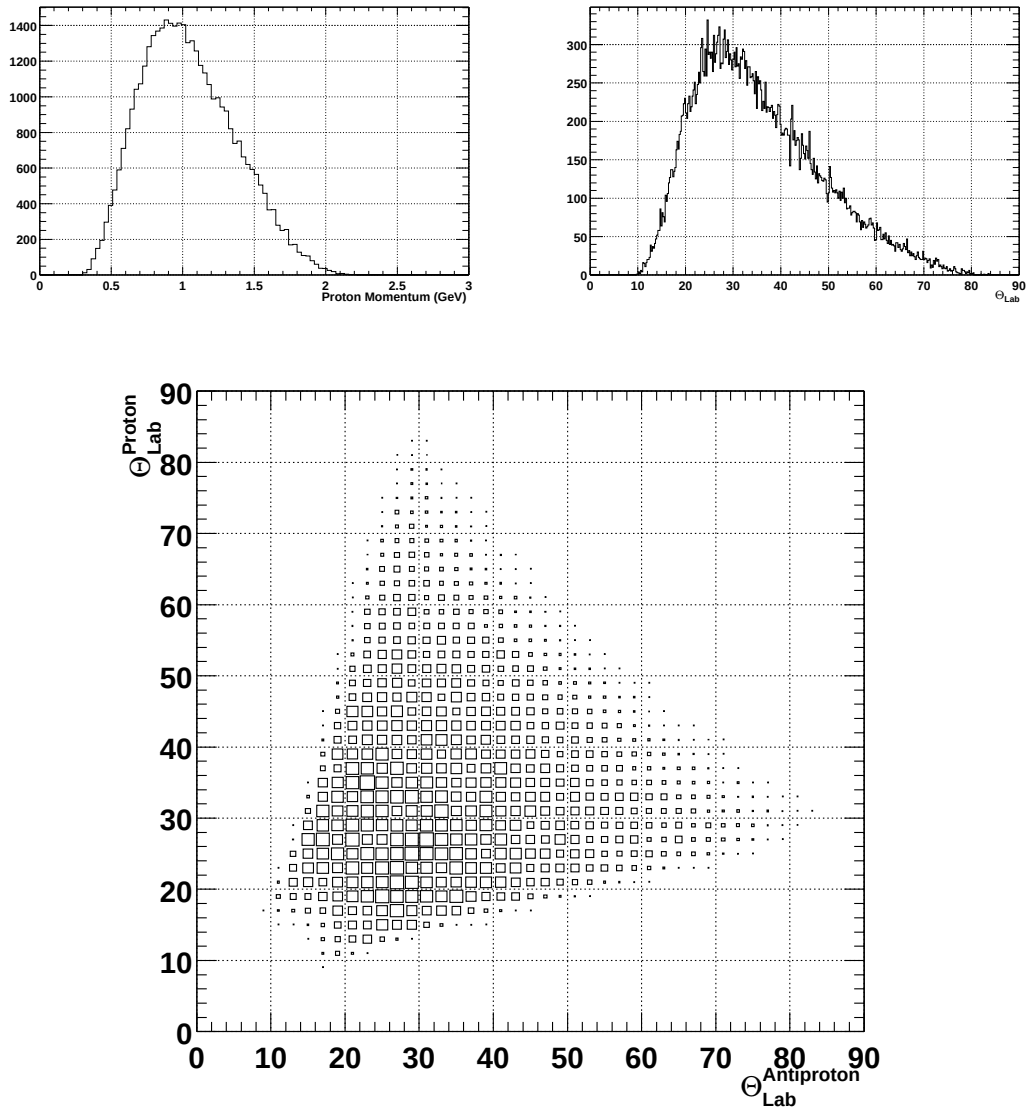

Figure 36: Monte Carlo $\gamma\gamma \to p\overline{p}$ events distributions for PEP-N at $\sqrt{s} = 3.1\,\mathrm{GeV}$, for beam energies of $3.115\,\mathrm{GeV}_{LER}$, $0.771\,\mathrm{GeV}_{VLER}$, and for $|\cos\theta^*| < 0.6$: (top left) proton momentum distribution; (top right) θ_{LAB}; and (bottom) θ_{LAB} of the proton versus the θ_{LAB} of the antiproton.

153, 154, 155, 156, 157]. Figures 36 (top left and bottom) show the θ_{LAB} [1] and the θ_{LAB} of the proton versus the θ_{LAB} of the antiproton distributions. These distributions show the better experimental conditions expected at PEP-N for two-photon events. A high detection efficiency, large angular acceptance, and a good trigger efficiency due to the higher momentum tracks are anticipated. The last row in Table 5 gives the number of $\gamma\gamma \to \mathrm{p\overline{p}}$ events expected at PEP-N within the detector acceptance, see Figures 36 (top right and bottom), but without any trigger and detection efficiency applied, and for a total integrated luminosity of $200\,\mathrm{pb}^{-1}$. The PEP-N detector under study will have the capability to detect also neutrons and antineutrons. Therefore it will be possible to detect also $\gamma\gamma \to \mathrm{n\overline{n}}$, which has never been done before. A priori a number of events quite lower than $\gamma\gamma \to \mathrm{p\overline{p}}$ is expected. It will be interesting to compare $n\overline{n}$ and $\mathrm{p\overline{p}}$ pair production cross sections in $\gamma\gamma$ as well as in e^+e^-.

[1] θ_{LAB} is the polar angle in the laboratory

3 Experimental Considerations

The primary goal of the proposed PEP-N experiment is to make accurate measurements of exclusive hadronic cross sections at a large number of energies between 1 and 3 GeV, leading to a measurement of R with a statistical accuracy of better than 1%. The measurement is planned to ultimately achieve a systematic uncertainty which is also less than 1%, which motivates the following strategy.

We believe that in this energy regime R can be measured accurately only by identifying individual channels and measuring their angular distributions, thereby allowing a determination of the energy-dependent acceptance on a channel-by-channel basis. This is feasible in e^+e^- annihilation because of the relative simplicity of most angular distributions, i.e. all 2 body hadronic processes have angular distributions $1+b_w \times cos\theta + c \times cos^2\theta$. These distributions can be fit and the acceptance accurately calculated. R is then obtained by summing the acceptance-corrected cross sections. In this approach we necessarily accurately measure individual channels. The detector as designed has high efficiency and acceptance for the significant hadronic channels including $e^+e^{\rightarrow}\bar{n}n$ and $\bar{n}n\pi^0$, which represent more than $\sim 2\%$ of the hadronic cross section above 1.9 GeV An additional advantage of the individual channel approach is that it lends itself to the effective use of the τ decay data, which provides information on G+ final states only.

The hadronic cross section falls as s^{-1} to about 20 nb at 3 GeV. The cross sections for the processes $e^+e^- \rightarrow p\overline{p}$ and $e^+e^- \rightarrow n\overline{n}$ are about 1 nb just above threshold, decreasing [57, 68] to about 0.01 nb at 3 GeV. The cross-sections for $\pi^+\pi^-$ and K^+K^- are about 0.5 nb at about 2 GeV and are smaller by at least a factor 10 at 3 GeV; that for K_LK_S is about half that and other meson pair cross-sections are expected to be comparable to that for $\pi^+\pi^-$.

We will collect enough hadronic events so that the statistical error on the hadronic cross section is well below 1% at each energy, which requires several tenths of a pb^{-1} at 1 GeV increasing to about 2 pb^{-1} at 3 GeV. Additional data at the higher energies will be important to define the acceptance for the exclusive channels with small cross sections. If we assume about 40 points, separated by 50 MeV intervals, the total integrated luminosity required is approximately 40-80 pb^{-1}. Taking a nominal instantaneous luminosity of $3 \times 10^{30}\ cm^{-2}s^{-1}$, we estimate 1-2 years for the measurement of R and the exclusive hadronic processes other than those involving baryons. We anticipate dedicated running with particular emphasis on the regions around $B\bar{B}$ thresholds.

The precise measurement of R calls for a detector that is capable of identifying all of the significant hadronic channels and of determining their kinematics to the extent that an accurate acceptance for each can be obtained. It must also be capable of identifying Bhabhas, muon pairs and $\gamma\gamma$ events. Muon, electron and direct photon identification are particularly important for an accurate R measurement because Bhabha scattering and muon and photon pair production are used to determine luminosity and we must obviously distinguish these channels from annihilations to hadrons, in particular from pion and kaon pairs.

The detector must have nearly 4π tracking and electromagnetic calorimetry, plus neutral hadron detection of sufficient acceptance and sensitivity to suitably control the cross section uncertainties due to channels with these (difficult to detect) particles. Fortu-

nately the asymmetric nature of the collision boosts neutrons forward and makes them energetic, limiting the required coverage for neutron detection. Channels with K_Ls are generally related to those with charged Ks and K_Ss. The detector described below is designed to have excellent tracking and good electromagnetic calorimetry in order to meet these criteria at an acceptable cost.

Forward hemisphere muons have momenta greater than 1.6 GeV/c. Muon identification is achieved in the forward $\pm 30°$ where the forward electromagnetic calorimeter represents approximately a nuclear interaction length and is followed by several interaction lengths of additional calorimetry. For $\sqrt{s} < 1.6$ GeV, both muons are identified. At greater $\sqrt{s}$, muon ID is achieved for at least one muon but those events represent the largest part of the cross section. Muon pair events in which both particles either strike a magnet pole or go backward are under study.

Bhabha scatters are identified by 4π calorimetry and kinematics. For nearly all events we will identify at least one electron, in most of them both. Bhabha scatters represent our most accurate measure of luminosity, and the tracking is designed to achieve the resolution required to accurately define the acceptance for this channel, as described in the section on luminosity.

In the model detector described below, we assume a zero degree collision as described in the accelerator design section, where a very-large-aperture dipole magnet is installed at the intersection, supplying the necessary field integral for bringing together and separating the beams.

3.1 VLER or LINAC

While the overall detector configuration is very roughly independent of the source of low-energy electrons, there are several significant differences.

- The expected instantaneous luminosity for the LINAC design might be smaller than the peak luminosity for the ring, but is much less energy-dependent, allowing extension of the range of the machine in both directions.

- In the VLER design the duty factor is approximately 1 as the VLER and LER bunches collide at 4.2 ns intervals. For the LINAC the current design has collisions for 3.5 μs at 120 Hz, for a duty factor of < 0.001. In the latter case cosmic ray and LER beam-gas backgrounds are substantially reduced.

- In the VLER design, $\int Bdl$ in the very-large-aperture dipole magnet must approximately scale with the VLER momentum. For the LINAC design, it is likely that few values for $\int Bdl$ are adequate, greatly simplifying the calibration of the tracking system.

4 Background calculations

The main sources of background for PEP-N are:

- synchrotron radiation;
- beam lost particles;
- beam-residual gas hadronic interactions.

All these background components have been analyzed. For the moment only the positron LER beam has been considered, whereas the study of backgrounds coming from the electron and HER beams is in progress. However these additional backgrounds are expected to be far less important, mainly because both the electron and the HER beams travel in the opposite direction. Furthermore energy and current of the electron beam are about one order of magnitude smaller than in the LER, whereas the HER beam can be shielded.

Synchrotron radiation background is relevant mostly from the point of view of the TPC integration time. Lost particles and beam-gas can affect the trigger rate and the total cross section measurement. In the case of the linac option for the electron beam these rates will be reduced by the linac duty factor.

4.1 Synchrotron radiation

The highest levels of synchrotron radiation come from the designs for the highest electron energies. Even at the highest energies, the low-energy electron beam contributes very little to the total synchrotron radiation. Most of the synchrotron radiation is generated by the LER and the amount of LER synchrotron radiation goes up as the VLER energy increases. This is because more and more of the central dipole field is used to separate the beams as the VLER energy increases. However, the fact that the IP is -25 cm upstream from the center of the main field and that we use the shared offset QDI1 magnet on the upstream side of the detector to further separate the beams means that relatively weak bending magnets can be used to close the upstream LER orbit. The main source of synchrotron radiation power comes from the two closest of the four dipole magnets on the LER beam line. The strength of these magnets for the 780 MeV VLER is 2.1 and 2.0 kG and they generate 465 and 1054 W respectively with a 2.14 A LER beam. The critical energies of these bend magnets are 1.36 and 1.3 keV. These low critical energies greatly reduce possible synchrotron radiation backgrounds in the detector. A complete beam pipe design still needs to include masks for this upstream LER synchrotron radiation. The power levels are low enough to not pose a problem for beam pipe cooling.

The LER orbit is virtually identical for the storage ring design as well as the LINAC design, so synchrotron radiation issues remain unchanged for either design.

More complete studies need to be made, but synchrotron radiation power does not seem to be an issue and detector backgrounds from synchrotron radiation should be very low. Figure 37 shows the fan of radiation coming from these upstream LER magnets.

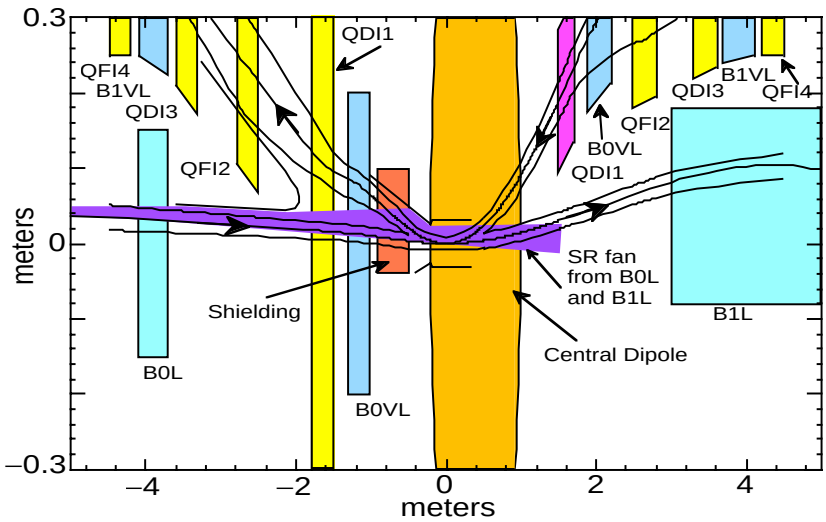

Figure 37: Fan of synchrotron radiation coming from LER upstream magnets.

4.2 Lost particles

Bremsstrahlung and Coulomb scattering of beam particles from the residual gas molecules in the beam pipe can result in high energy beam particles and photons striking masks and the beam pipe near the IP. The resulting electromagnetic showers will cause detector occupancy and possibly unwanted triggers. Hadronic showers from photoproduction can also cause triggers. Initial studies have included only those lost particles from the LER, for which results can be compared to those obtained from similar studies for BaBar at a similar stage of development. These studies are preliminary and do not yet include GEANT simulations, however, this capability will be soon developed. The LER lost particle showers will, in general, point toward the forward calorimeter. In addition, there will be lower energy lost particles from the e^- beam and possibly much higher energy lost particles from the HER where it passes through the bottom part of the forward calorimeter, these possible backgrounds will be the subject of future studies.

The code LPTURTLE [168] was used to estimate the rate of particles from these processes incident on masks and beam pipes near the IP. A scattering point is picked randomly (with optional weighting by a pressure distribution) along the beam line, and the scattered secondary particles are propagated through the beam line until either an aperture is hit or the particle passes completely through the detector region. For bremsstrahlung scattering, the photon and positron are both propagated whereas only the scattered positron is tracked in Coulomb scattering. The kinematic parameters for only the particles of interest, i.e. those which strike in a specified region near the IP, are recorded in an ntuple for analysis using PAW and can also be transformed to the labora-

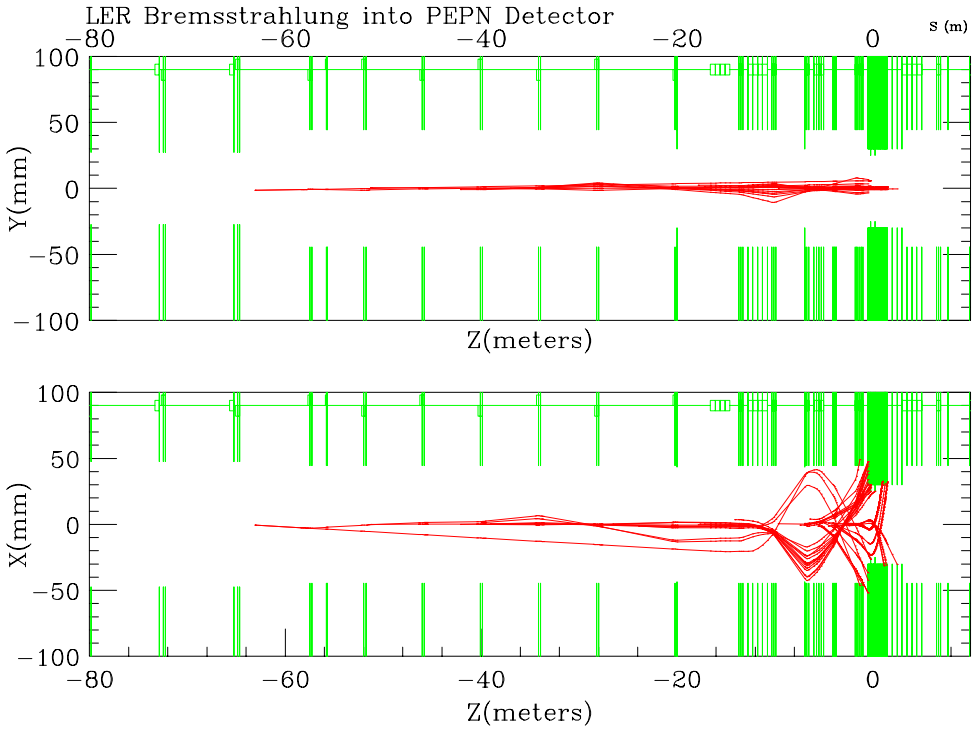

Figure 38: LER beamline with PEP-N and sample of trajectories resulting from Gas Bremsstrahlung.

tory coordinate system and stored for use as input to GEANT. Ntuples are also used to study the efficacy of cuts at possible locations for collimation. In the studies presented here the modified LER lattice is simulated from near the end of the preceding arc to several meters downstream of the IP. In all simulations we assume that the LER has a stored current of 1 Ampere and the residual gas is nitrogen at a constant pressure of 1 ntorr. Placement o f collimators upbeam of the IP reduces the rate of secondaries hitting apertures inside the detector. Multiturn effects have not yet been studied. Optimization of upstream collimation and masking near the experiment is in progress. At this time, only the energy weighted distribution along the beam line is presented. This distribution is then compared to similar calculations for the LER at BABAR.

Figure 38 shows a sample of the positron and photon trajectories in the X and Y planes from bremsstrahlung scattering in the last 80 m of LER upstream of the PEP-N detector that strike a 3 cm radius beam pipe in the region -2.0 m to +3.0 m from the IP. The source of these particles is almost uniformly distributed in Z from -70 m to near -15 m where the distribution then doubles. Looking at the X plane one can see the positrons are deflected far off of the beam axis toward negative values of X at a point near -7 m. These positrons have an energy peaking near 2.4 GeV and can be effectively eliminated by placing a collimator at -7 m with an X offset of about -0.02 m. This collimator will stop most of those positrons that scattered between -70 m and -15 m. The collimator does not violate the Beam Stay Clear (BSC) for the LER and hence should not affect the BaBar Detector but most likely would be one with variable jaw design to allow adjustment for optimization. With this collimator in place the lost positron count is reduced by a factor

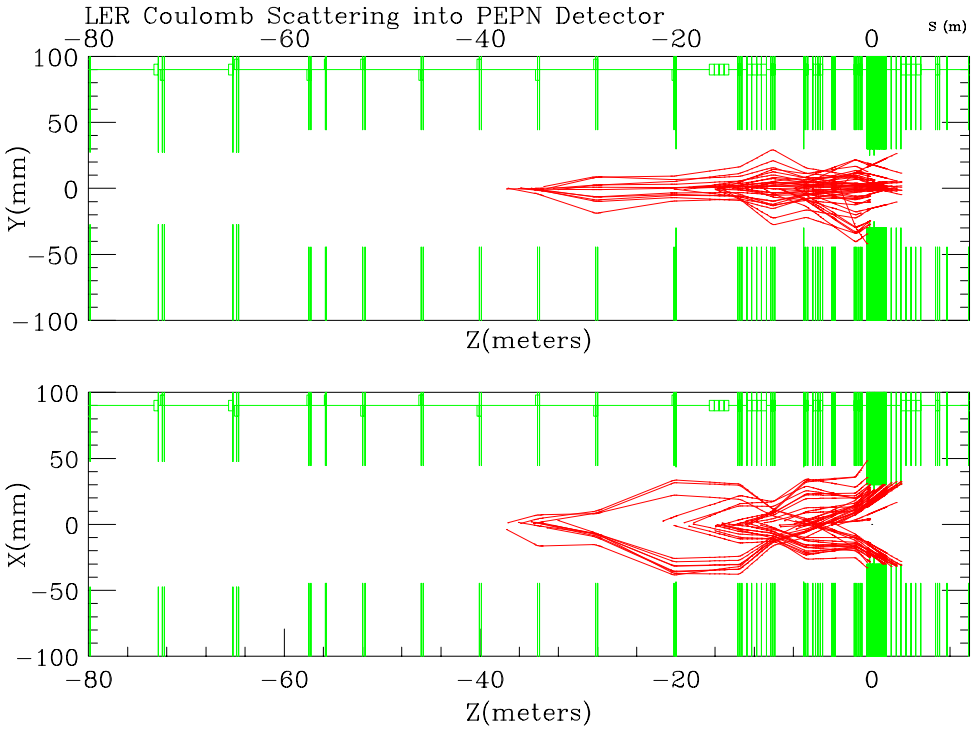

Figure 39: LER beamline with PEP-N and sample of trajectories resulting from Coulomb Scattering.

of two and the energy deposited by a factor of three. At this time, the lattice with which we are doing these studies has not been finalized and thus contains some beta and dispersion function miss-matches. Further, reduction may be possible when the lattice design has been improved. The region between -15 m and +3 m will require that careful attention be paid to the vacuum system, for which it is estimated that levels of 0.3 nTorr are achievable.

Figure 39 shows a sample of the positron trajectories in the X and Y planes for Coulomb scattering off residual gas molecules. Here the Z distribution of scattering points (where the positrons strike within a few meters of the IP) is peaked at -35 m and in the region between -20 m to the IP. By inspection it can be seen that a collimator placed in the X plane at -20 m with double jaws set at X = ± 0.02 m will stop those positrons scattered at -35 m. This collimator will stop about 25% of the total count of 3.2 GeV positrons. A second collimator placed at the same location (-7 m) as that which was found to be efficacious for the bremsstrahlung but now double jawed with X = ± 0.02 m will stop an additional 25% of the positrons that have scattered from Z of -25 m to -15 m.

Figure 40 and Figure 41 can be used for comparison with similar simulations done for BABAR of the energy deposited within ± 1.5 m of the IP. These results [169] were for 1 nTorr Nitrogen gas and 2.0 A of beam current. For comparison, we report both these Babar results and our results normalized to a beam current of 1.0 A and a vacuum of 1 nTorr Nitrogen gas. Thus for Babar, the Bremsstrahlung scattering deposited a total of 4.6 GeV/μs or 1.5 GeV/m-μs. Similarly for comparison the result for Coulomb scattering

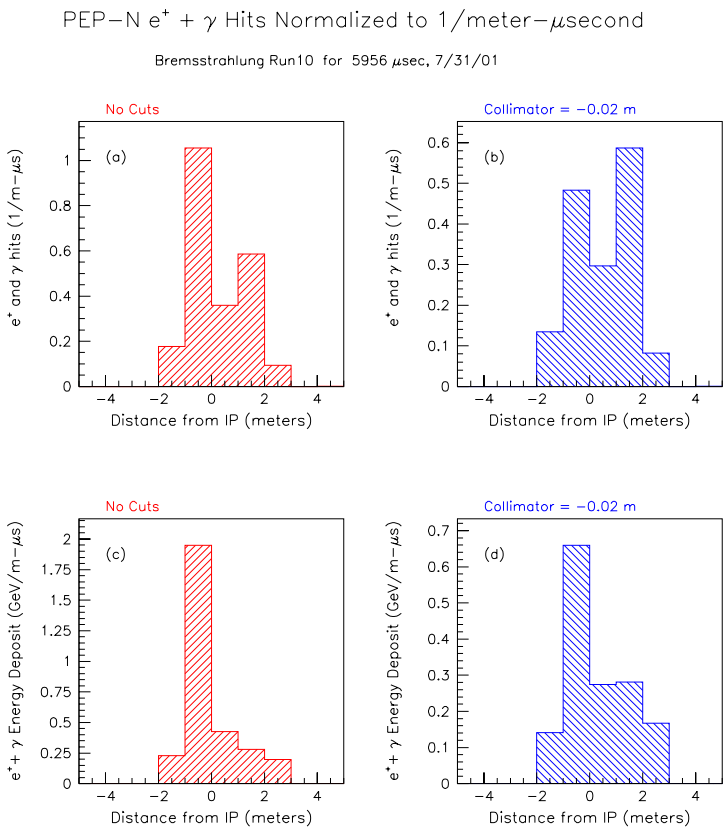

Figure 40: Hit count and energy deposited near IP from Bremsstrahlung photons and positrons.

reported for BaBar was a total of 0.70 GeV/μs or 0.23 GeV/m-μs.

Figure 40 shows the number and energy deposition of positrons and photons hitting a 3 cm radius beam pipe in the region -2.0 m to +3.0 m from the IP from bremsstrahlung. The top two histograms are the number of hits/m-μs for: a) no upstream collimation and b) a single horizontal jaw collimator set at X = -0.02 m from the beam axis near Z = -7 m from the IP. The bottom two plots show the energy deposited in GeV/m-μs for: c) no collimation and d) with this single jawed collimator. With the collimator in place the total LER bremsstrahlung energy deposition in this region is 1.5 GeV/μs with a differential peak of 0.65 GeV/m-μs. These are to be compared with the respective values above for BaBar of 4.6 GeV/μs or 1.5 GeV/m-μs.

Figure 41 is similar to Figure 40 but for Coulomb scattering. Here two horizontal collimators are needed both with double jaws. They are located at -20 m and -7 m upstream of the IP with all four jaws set to X = $\pm$0.02 m. The top two histograms are the number of hits/m-μs for: a) no collimation and b) with collimation. The bottom two plots show the energy deposited in GeV/m-μs for: c) no collimation and d) with collimation. The total LER energy deposition from Coulomb scattering in this region is about 0.4 GeV/μs with a differential peak of 0.19 GeV/m-μs. For comparison, the BABAR simulation gave a total of 0.70 GeV/μs and 0.23 GeV/m-μs, respectively.

These results compare reasonably well with BaBar studies at this early stage of study.

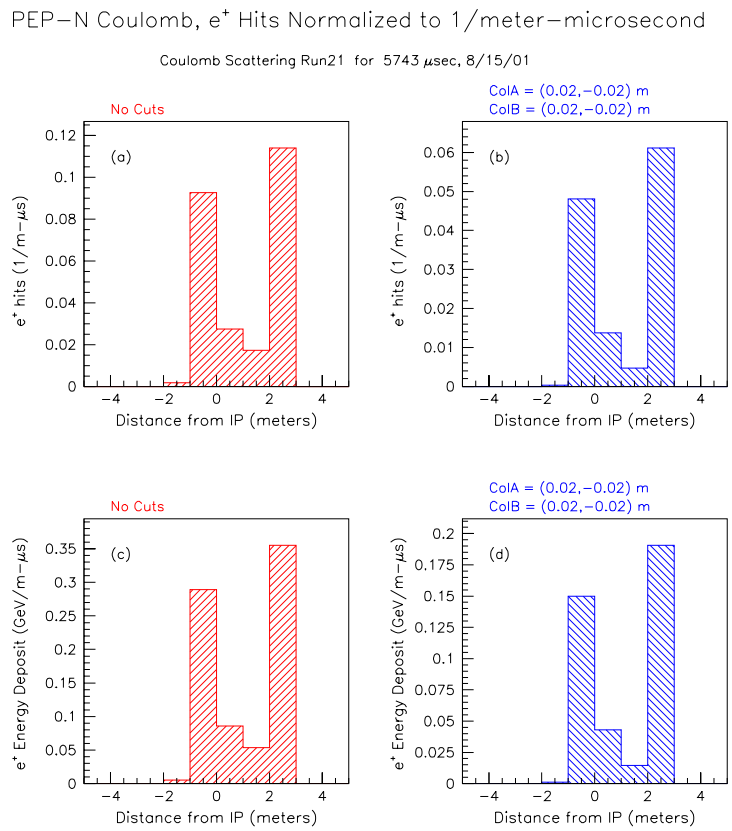

Figure 41: Hit count and energy deposited near IP from Coulomb Scattered positrons.

These studies will be continued as the design of the lattice, masks, beam pipe and the detector become more refined. Work is commencing to use results from these lost particle processes as input to GEANT to study effects on occupancy and triggers rates. Similar studies will be undertaken for VLER and HER.

4.3 Electroproduction

4.3.1 Generator

One of the sources of background for PEP-N detector is the electroproduction from beam-gas interaction in the LER. A first evaluation of this kind of background is done using PYTHIA (version 5.720) and JETSET (version 7.408)[170] codes. The simulated reactions are e^+p and e^+n with 3.12 GeV positrons colliding on fixed target protons and neutrons. The cross sections given from PYTHIA for inclusive final states are $\sigma(e^+p) =$ 3.08mb and $\sigma(e^+n) = 3.02$mb.

Table 6 summarizes the fraction of particles in the final state. A cut on the total energy of the particle $E > 1$MeV has been performed in order to cut the huge amount of low energy bremsstrahlung photons.

Figures 42 to 44 show momentum and angular distributions for background particles.

Part. type	*Fraction*
γ	4%
e^+	33%
π^0	13%
π^+	9%
π^-	8%
n	18%
p	15%
other	$< 1\%$

Table 6: Relative frequency for different kinds of particles generated in e^+p and e^+n interactions from PYTHIA-JETSET code.

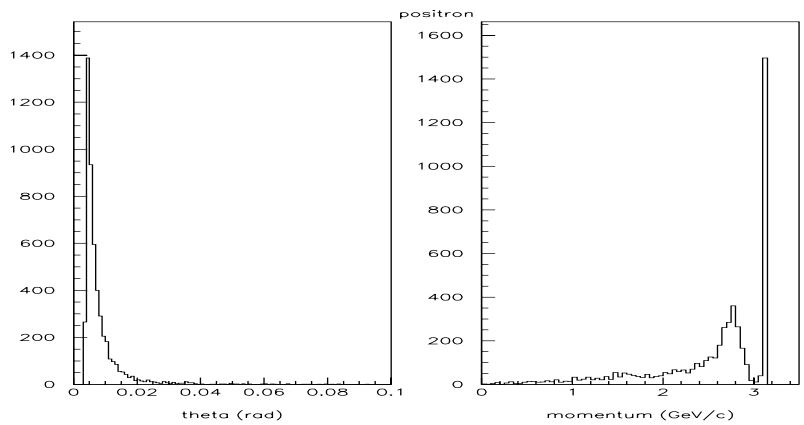

Figure 42: Polar angle and momentum distribution for e^+ in electroproduction background. Note the enlarged scale for θ with respect to the other figures.

4.3.2 Background in the TPC

Final states obtained from e^+N interactions are generated with the interaction vertex uniformly distributed along 6 m of beam pipe (between -4 m and +2 m from the PEP-N interaction region). A density corresponding to 1 nTorr is assumed for the residual gas in the beam pipe.

The background rate is calculated following what was done for BABAR[171]. The target density per unit area is is given by:

$$n/A = \frac{\delta z}{1\text{m}} 3.3 \cdot 10^9 \text{cm}^{-2}$$

and since $\delta z = 6$m, the value to be used for the calculation of the rate is $n/A = 2 \cdot 10^{10}\text{cm}^{-2}$. For different values of the pressure in the beam pipe, the value of n/A can be obtained multiplying it by (p/1 nTorr).

For a positron frequency in the LER of $i = 1.34 \cdot 10^{19}$Hz the rate turns out to be:

$$w = \sigma \frac{n}{A} i = 770\text{Hz}.$$

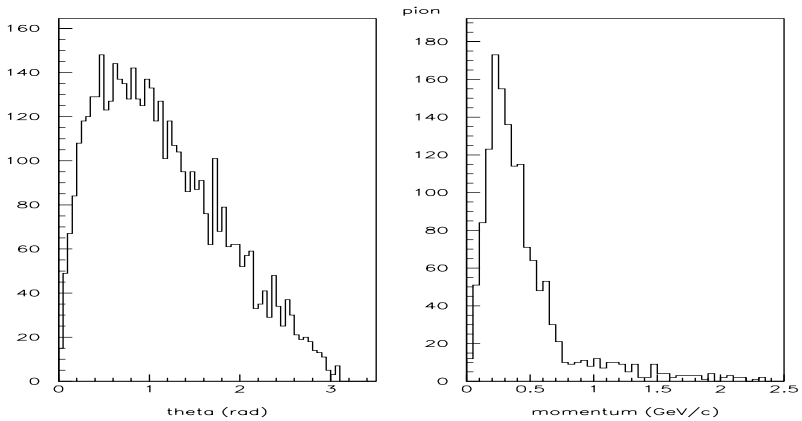

Figure 43: Polar angle and momentum distribution for pions in electroproduction background.

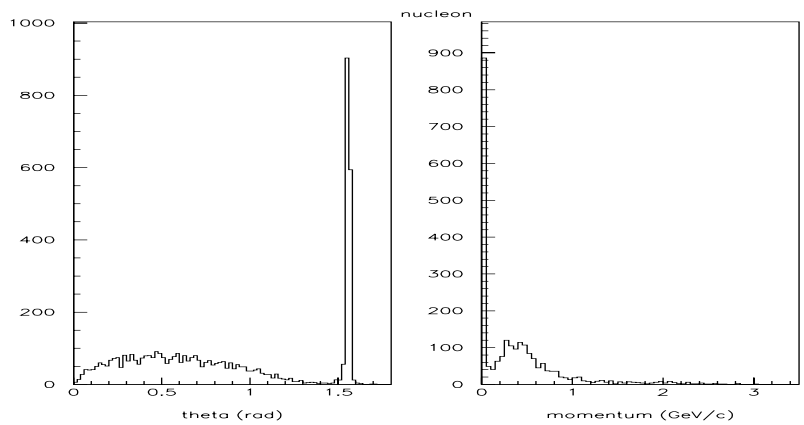

Figure 44: Polar angle and momentum distribution for nucleons in electroproduction background.

As an example we will consider now the effect of this events on the TPC. The effect of electroproduction background on the trigger rates will be analyzed in the trigger section. To calculate the real background rate affecting PEP-N TPC, the produced events are then used as input for the GEANT simulation of the detector. The number of observed charged tracks in the TPC are counted. As shown in figure 45, $\sim$ 1300 events out of 5000 give 1 or more detected charged tracks; this corresponds to a background rate of $\sim$ 200Hz.

Table 7 gives the proportions between the various kind of charged particles detected.

The particles coming from the region of the beam pipe near the interaction region, which can contaminate a real event, are especially pions or nucleons. Positrons come mainly from the pipe region upstream with respect to the detector, as can be noticed from figure 42, so the rate of $\sim$ 200Hz can be considered as an upper limit for the rate of contaminating events.

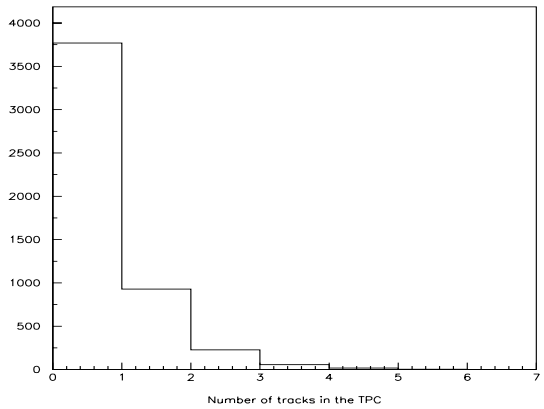

Figure 45: Number of tracks in the TPC.

Part. type	*Fraction*
e^+	29%
e^-	19%
π^+	18%
π^-	16%
p	16%
other	2%

Table 7: Fraction of particles detected in the TPC.

5 Experimental design

The detector is being designed to perform a high precision (2 % or better) measurement of R, a new determination of baryon and meson form factors and study of various multi-hadronic channels. The main design criteria, needed to accomplish these measurements, are: the capability to reconstruct efficiently exclusive final states (for the measurement of R using the exclusive approach) and to detect $N\overline{N}$ events for the measurement of nucleon form factors (as well as R).

5.1 Detector requirements

The detector design must take the following requirements into account:

- **Low mass tracking.** In the energy range of PEP-N multiple scattering contributes significantly to the momentum resolution ($\approx 2\%$);
- **Momentum measurement with good accuracy.** A high-precision measurement of R requires the ability to recontruct efficiently every individual final state. This can be done by means of topological selections and kinematic fitting. The possibility to identify each channel contributing to R will thus depend crucially on a high-precision measurement of the momentum.
- **Electromagnetic (EM) calorimetry.** The EM calorimeter will have to measure direction and energy of photons from neutral pion decays with high precision and accuracy down to very low energy (below 100 MeV). EM calorimetry is also needed to measure Bhabha events, which will be used for the luminosity measurement.
- **Particle ID** is necessary for π/K separation; this feature is crucial to reconstruct efficiently final states containing pions and kaons.
- **Luminosity measurement** with an accuracy of the order of 1 % or better.
- $N\overline{N}$ **capability** needed both for the neutron form factor and the R measurements.

A key feature of the proposed PEP-N facility is the fact that it is an asymmetric machine: the CM system is boosted with respect to the lab frame, with $0.6 < \beta_{cm} < 0.94$. As a consequence even slow particles (in the CM) are boosted to momenta ranging from a few hundred MeV to 1-2 GeV. This makes their detection easier and it enhances the capabilities for particle ID. Moreover the more limited angular coverage needed makes the apparatus smaller and thus less expensive. The asymmetric option is also better from the accelerator point of view, because it makes beam separation easier.

Another important feature of the PEP-N design is the magnet. The magnetic field field required to perform beam separation with minimal interference with PEP-II operations is a weak dipole field ($B \approx 0.3\ T$). This field will also be used by the experiment for the measurement of charged particle momenta; therefore the tracking system will be housed inside the magnet gap which, as a consequence, has to be made big enough to give a suitable acceptance.

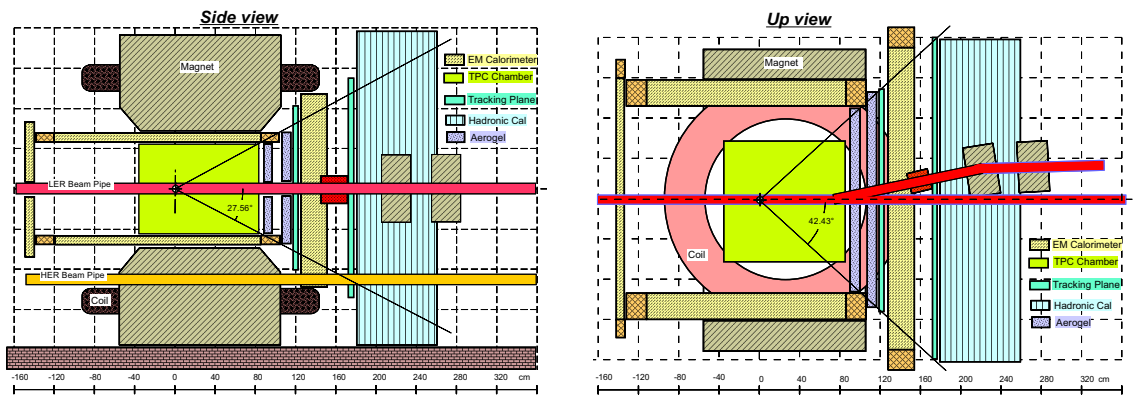

Figure 46: PEP-N detector layout: side view (left) and top view (right).

5.2 Detector Layout

The proposed detector layout is shown in fig. 46. It consists of the dipole magnet and of central (i.e. inside the magnet) and forward detector elements.

The central detector is housed inside the gap of the magnet: it consists of a time projection chamber (TPC) and of EM calorimeter modules located on the magnet poles (PCAL), along the side (BCAL) as well as in the backward direction (RCAL).

The dipole magnet and the central detector are not centered on the interaction point, but they are shifted 25 cm in the forward direction, to increase the path inside the magnetic field for the forward produced particles.

The forward detector consists of two silicon aerogel counters for particle ID, a scintillator hodoscope, additional tracking planes (drift chambers) as well as EM and hadronic calorimeter modules.

Also shown in fig. 46 are the HER (High Energy Ring), LER and VLER beam pipes, as well as various accelerator bending magnets.

The individual detector components are discussed in detail in the dedicated sections. In what follows we only give a brief description of the main features of each element.

Magnet The dipole magnet provides the vertical B field needed for beam separation. It is also used to measure the momenta of charged particles. Its gap houses the central tracking and calorimeter systems, and therefore it must be big enough to give adequate acceptance. As a consequence the B field has a limited degree of uniformity and moreover it extends well outside the magnet itself. The design of the magnet has thus required extensive simulation to maximize the field uniformity, which is very important for a smooth operation of the tracking detector.

The scintillator hodoscope The scintillator hodoscope is composed of two planes segmented in horizontal and vertical strips. Fast logic combines the signals from the strips, and these combined signals are used in the first level for the trigger of charged events. The time resolution of this detector is about 150 ps.

Tracking The tracking system must reconstruct the trajectories of charged particles to measure their momenta with good precision. The main requirements on the tracking are:

- good space resolution (200-300 μm);
- dE/dx capability (for particle ID, particularly at low momenta);
- low mass, to minimize multiple scattering;
- minimize dead spaces (frames, supports etc) which limit the acceptance and reduce the sensitivity to low energy photons.

The central tracking must operate in a non perfectly uniform magnetic field.

A TPC with a slow, He based gas (to minimize distortions due to magnetic field non-uniformity) meets the above requirements. The use of a multi GEM detector (instead of wires) will eliminate the $E \times B$ term in the resolution, leading to better and more uniform spatial resolution.

Forward tracking The forward tracking chambers will be used to correct distortions in the TPC, they will serve as veto for neutrons and they will help with muon identification.

The forward tracker is composed of two drift chambers: one in front of the EM calorimeter, the other behind the hadron calorimeter. Each chamber is made of four sets of two staggered sense wire planes, oriented along four directions, each one rotated by 45° with respect to the previous one, and all orthogonal to the beams. This makes it possible to reconstruct charged tracks without ambiguities, minimizing the effect of wire inefficiencies by providing redundant information. Track positions will be reconstructed with a precision of 100 μm per view.

EM calorimeter The EM calorimeter will be used primarily to identify photons from neutral pion decays and $e^+e^- \to e^+e^-$ Bhabha events. The main requirements are:

- high acceptance;
- good efficiency and good energy resolution (few %) down to low energies (below 100 MeV);
- good time resolution.

A lead and scintillating fiber calorimeter based on the KLOE design meets all the above requirements.

Particle ID Particle identification is achieved by means of two aerogel counters, each 10 cm thick (total thickness 0.2 radiation lengths), which can achieve 4σ $\pi - K$ separation in the momentum range between 600 MeV/c and 1.5 GeV/c. The design of these counters is based on the detectors built for the KEDR experiment in Novosibirsk.

Below 600 MeV/c particle ID will be based on dE/dx in the tracking chambers as well as time-of-flight (TOF) in the forward EM calorimeter.

Hadron calorimeter The hadron calorimeter will be used mainly for $n\overline{n}$ identification, therefore it should be highly efficient both for neutrons and antineutrons. In addition it should provide TOF and position measurements for both n and $\overline{n}$.

The hadron calorimeter can be built as an extension of the electromagnetic calorimeter (based on the KLOE design), with a sampling fraction optimized for the detection of neutrons and antineutrons.

Luminosity monitor The online measurement of the luminosity, required for machine tuning and monitoring, can be implemented using a PEP-II type monitor, based on single Bremsstrahlung at zero degrees.

Offline, the necessary 1 % accuracy in the integrated luminosity measurement can be achieved using Bhabha events.

5.3 The dipole magnet

A vertical magnetic field is required at the PEP-N Interaction Point (IP) to separate positron and electron bunches before and after collision and to provide tools for momentum tracking for the Detector equipping the Interaction Region (IR). Design considerations and simulation results are reported in this chapter resulting from studies performed with the aim of matching the often competing requirements from the Accelerator as well as from the Detector side.

5.3.1 Requirements and Design considerations

Given the LER 3.15 GeV e^+ fixed energy and the wide energy range (0.08 to 0.80 GeV) required for the e^- beam, the PEP-N complex would constitute a very Asymmetric Collider with a CM energy

$$E_{CM} = 1.00 \text{ to } 3.15 \text{ GeV} \tag{6}$$

and a large energy ratio

$$r_E = \frac{E(e^+)}{E(e^-)} = 38.9 \text{ to } 3.9 \ . \tag{7}$$

The relation (7) suggests the concept, already adopted at PEP-II, of a magnetic separation of the colliding bunches. A vertical dipolar field at the PEP-N IP is presently considered to avoid unwanted bunch encounters and strongly reduce long-range beam-beam effects. A good uniformity, large aperture magnetic field is also considered as a valuable ingredient of the PEP-N detector.
Obvious difficulties exist to accommodate the small dipole required for beam separation and the central detector TPC in a solenoidal field. The solution has then been retained to make use of a large IP dipole to contemporarily satisfy both the collider and the detector requirements.

The design of the magnetic structure of the PEP-N IP dipole aims at providing high field uniformity in the gap region occupied by the TPC, together with a considerable angular vertical aperture in the forward direction and a large gap capable of hosting a complex multi-task detector.

A uniformity factor is defined along and transversely to the beam direction (X and Y respectively)

$$\eta_{\mathrm{x,y}} = \frac{B_z(\mathrm{x},\mathrm{y})}{B_z(0,0)} \tag{8}$$

where deviations of the vertical component $B_z(\mathrm{x},\mathrm{y})$ from the central value $B_z(0,0)$ are evaluated to compare the performance of different geometries.

Shims on the pole pieces are usually adopted to improve the field uniformity. To avoid a reduction of the gap height available to detector components a considerable improvement in the field quality can be achieved by means of "anti-shims" using excavations in the poles.

The dipole magnetic center, located 25 cm downstream of the IP in the LER beam direction provides a longer forward field region for a better exploitation of the CM boost. The maximum vertical angular aperture is then defined by the largest dipole gap compatible with the LER-to-HER beams distance and vertical magnet dimensions fitting in the available space in the IR 12 area.

For a given induction $B_\mathrm{o} \equiv B_z(0,0)$ and magnet gap g the DC power consumption scales linearly with the current density δ:

$$P_{DC} \propto g\, B_\mathrm{o} \cdot \delta \tag{9}$$

The excitation coils of the IP dipole are designed to carry low current densities over the full operation range to contain the exploitation costs of the magnet within acceptable limits.

5.3.2 The Modeled Versions

Several dipole versions were conceived and modeled using the TOSCA code [172] to evaluate the field uniformity factor (8). Two main versions are presently retained for final approval. Their characteristics are collected in Tables 5.3.2 and 5.3.2 together with those of the DV.03 dipole [173].

VERSION	**GAP**	**POLE GEOMETRY**		$\mathbf{\Phi_{fw}}$
DV.03	1.2 m	Cyl. ϕ 1.6 m	Tapered / Flat	$\pm 35°$
DV.06	1.6 m	Square 1.6 m	Tapered / Shims	$\pm 37°$
DV.07	1.6 m	Square / Circ.	Tapered / Shims	$\pm 37°$

Table 8: Physical characteristics of IP dipole versions DV.03, DV.06 and DV.07. The forward vertical aperture Φ_{fw} is measured from the IP (not from the magnet centerline, see chapter 5.3.1). Total gap heights in the DV.06 and DV.07 include pole-piece excavations for improved field uniformity.

The DV.06 dipole

The DV.06 dipole shown in Fig. 47 is an evolution of the DV.03 presented at the PEP-N Workshop [173] which better meets the design criteria of section 5.3.1 and the requirements outlined in chapter 5.3.1. The magnet is 1.60 m long in the beam direction and ~ 3 m high to comply with the existing floor in IR 12. The 1.30 m maximum gap provides a reasonably wide forward vertical aperture for the detector and allows adequate shielding for the HER beam, hosted in the lower pole-piece.

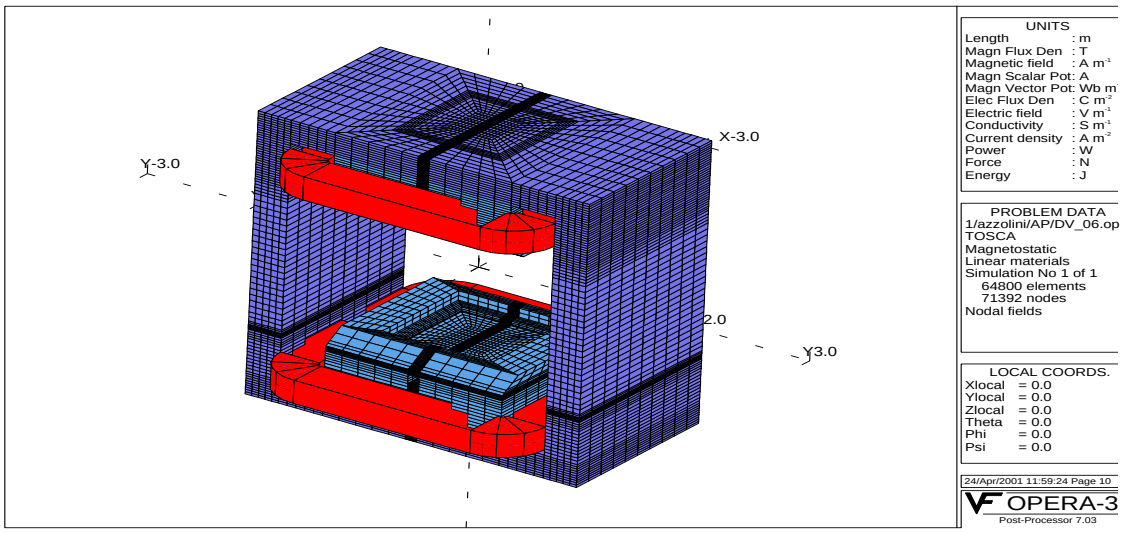

Figure 47: 3D view of the DV.06 dipole. The magnet is about 3 x 3 m (H x W) and 1.60 m long. The HER beam pipe is hosted in the lower pole-piece, above the coil.

Tapered pole pieces improve the vertical forward aperture compared to previous versions (DV.03) and pole excavations provide a fairly good field uniformity (see Table 5.3.2). The field strength for x = ±2.0 m and along the TPC (x = ±0.6 m) are shown in Figs. 48 and 49.

The integrated field strength across the HER beam pipe, shown in Fig. 50, shows the contribution to the field integral seen by the HER beam from the lower coils for which additional shielding is to be provided.

The DV.07 dipole

The physical dimensions of the DV.07 magnet are similar to the DV.06 ones, but the the pole-pieces differ in the front and the back sides of the dipole as shown in Fig 51. The tapering of the pole-pieces in the front (outgoing e^+ direction) follows a circular profile centered at the IP to make the Φ_{fw} vertical aperture fully available across the horizontal aperture. Conversely, the back-side pole tapering has been removed to extend the uniform field region without penalizing the backward vertical aperture.

Breaking the magnet symmetry in the X direction caused some problems with the TOSCA package. The field strength and uniformity of the DV.07 dipole were then inferred from those of two symmetric dipoles with same gaps, shims and coil geometry: a DV.07**s** with **s**quare/non-tapered poles, and a DV07**r** with **r**ound/tapered poles. Individ-

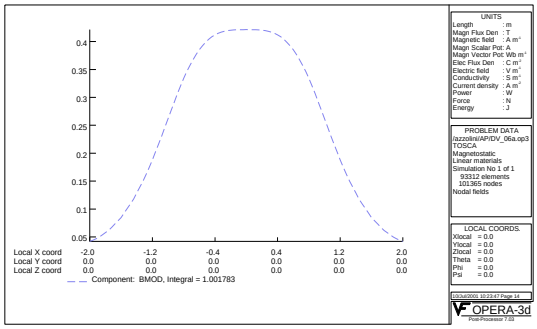

Figure 48: Dipole DV.06: total field integral for $B_o = 0.42\,\mathrm{T}$.

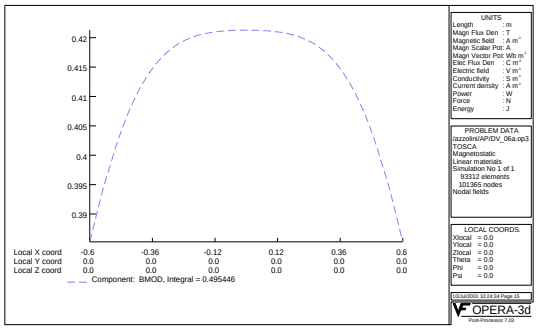

Figure 49: Dipole DV.06: field integral for x = $\pm 0.6\,\mathrm{m}$. $B_o = 0.42\,\mathrm{T}$, $\eta_x(\pm 0.6\,\mathrm{m})$ =91.7%.

ual field integral plots and associated numerical tables, matched at the vertical symmetry plane, represent the behavior of the asymmetric DV.07 dipole.
Field uniformity figures inferred from the DV.07**s** and DV.07**r** dipoles are collected in Table 5.3.2.

5.3.3 Operational Scenarios

A **scaling-field** scenario requires the IP magnetic field to vary with the electron energy $E\,(\mathrm{e}^-)$. In this case the incoming and outgoing trajectories of the electron beam at the

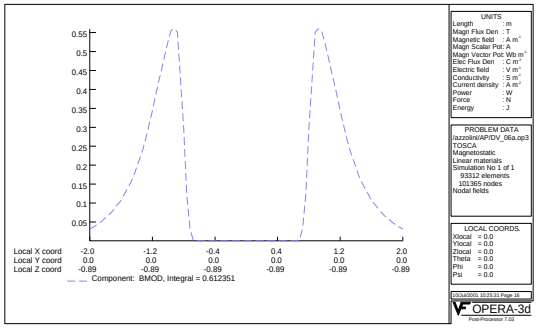

Figure 50: Dipole DV.06: total field integral along the HER beam pipe for $B_o = 0.42\,\mathrm{T}$.

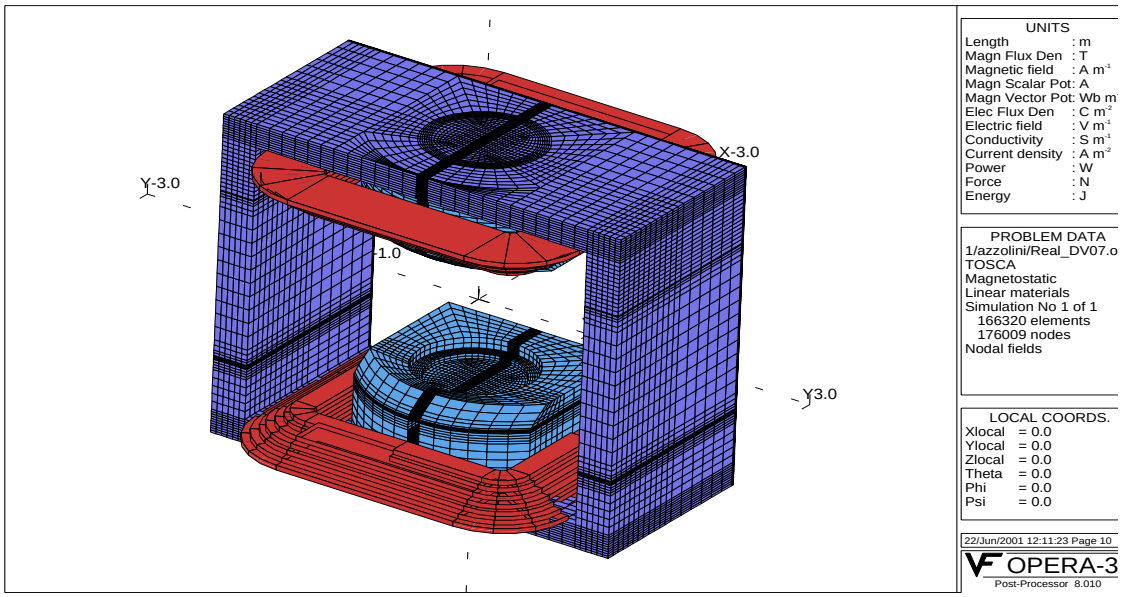

Figure 51: Front 3D view of the DV.07 dipole. LER positron beam travels out of page. Pole-pieces show the circular tapered profile for full vertical aperture across the horizontal plane and shim excavations.

IP are frozen and the IR layout is uniquely defined.
This option presents some disadvantages. The compensation of the LER beam closed orbit distortions induced by the dipolar field would depend on the electron energy and might become difficult at high $E\,(\mathrm{e}^-)$ values. Moreover, the magnetic field mapping should be performed at several field levels.

Alternatively, a fixed-field scenario can be envisaged where the IP dipole is operated at one or two field levels (highlighted in Table 9). The integrated strengths needed to provide the right IR layout at the different $\mathrm{e}^- -$ beam energies are obtained by shielding the original field distributions. Two different IR layouts might nevertheless be envisaged

DIPOLE	$\mathbf{B}_\mathrm{o}$=0.30 T		$\mathbf{B}_\mathrm{o}$=0.42 T	
	η_x (%)	η_y (%)	η_x (%)	η_y (%)
DV.03	81.1	79.0	81.1	76.8
DV.06	92.7	91.0	91.7	89.8
DV.07	91.8	94.8	91.8	94.8

Table 9: Field uniformity $\eta_{\mathrm{x,y}}(\pm 0.6\,\mathrm{m})$ for two B-field values. Figures for the DV.07 dipole are inferred from those evaluated for the DV.07**s** and DV.07**r** symmetric ones.

to cope with the large electron energy range.
This solution offers the considerable advantage of reducing the number of magnetic configurations in the IR and simplifies the field mapping task.
The main parameters associated to the two scenarios are collected in Table 10.

ENERGY		**FIELD**	**DV.03**		**DV.06**		**DV.07**	
E_{CM} (GeV)	$E\,(e^-)$ (GeV)	B_o (T)	I (A)	P_{DC} (kW)	I (A)	P_{DC} (kW)	I (A)	P_{DC} (kW)
1.000	0.080	0.048	127	2.5	136	4.6	136	4.8
1.935	0.300	0.180	478	35.0	510	63.7	510	69.0
2.498	0.500	**0.300**	**796**	**96.0**	**850**	**176.7**	**850**	**191.8**
2.993	0.700	**0.420**	**1114**	**188.5**	**1190**	**347.2**	**1190**	**376.5**
3.160	0.800	0.480	1274	246.0	1360	455.8	1360	490.1
Coils: Cu / 20 x 20 mm^2 Φ 8mm			$\mathbf{N_c} = \mathbf{180}$ turns / coil		$\mathbf{N_c} = \mathbf{225}$ turns / coil		$\mathbf{N_c} = \mathbf{225}$ turns / coil	

Table 10: Main parameters for the scaling and the fixed-field (highlighted) scenarios. Figures for P_{DC} are evaluated for standard Copper conductor. N_c is the number of turns in each coil.

5.4 Central tracking

The difficulties with various choices of tracking concepts in the PEP-N dipole magnet can be summarized as follows:

- A classical wire chamber with wires parallel to beam pipe would have very asymmetrical drift as a function of cell azimuth.
- A classical wire chamber with wires parallel to magnetic filed would have rather "ugly" vertex coverage, and a large mass right in the vertex region caused by the wire supporting end plate.
- A classical TPC with the electric field aligned with the magnetic field would have very large distortions because E versus B angle was as much as 18° at radial distance of 50 cm in the initial design, and possibly large low energy background, which normally goes through the beam pipe, can follow the magnetic field into the TPC active volume.

We have decided to pursue the TPC concept hoping that the TPC distortions can be dealt with a choice of gas and sophisticated laser calibration system, and the large background can be dealt with the robustness of the TPC concept if one runs very low gas gain. Furthermore, it was believed that the non-uniformity of the magnetic field would be improved by modifications of pole shapes.

5.4.1 Field Uniformity of the Dipole Magnet

At the time of the workshop there were three magnetic field maps available: DV02 (initial design), DV03 (the first improvement) and DV06 (the best by the time of the workshop). Figure 52 shows the successive improvements in the field uniformity. The improvement is characterized in terms of Br and angle α between the magnetic field and the vertical electric field direction. One can see that the α angle is almost 18° in the DV02 design, and less than 5° in the DV06 design.

5.4.2 Calculation of TPC Distortions

The Bagboltz-Monte program [174] has been used to calculate the drift velocity components $v_{x,y,z}$ (E,B). This particular program is presently considered the most correct method to calculate this problem, if one is dealing with the reasonably conventional gases. Once one knows the drift velocity components as a function of z-vertical (aligned with the dipole's field), one can calculate the distortions in the detecting plane using the following numerical integration:

$$\begin{aligned} dx &= \int_{t_1}^{t_2} v_x \, dt = \sum_i \langle v_x \rangle_i \frac{(dz)_i}{\langle v_z \rangle} \\ dy &= \int_{t_1}^{t_2} v_y \, dt = \sum_i \langle v_y \rangle_i \frac{(dz)_i}{\langle v_z \rangle}. \end{aligned} \tag{10}$$

In the following, we calculate the worst case distortion at $r = 50$ cm for the total drift of 50 cm. Figure 53 shows an example of such calculation for 80%He + 20%CO_2 gas, which is considered a slow gas. The maximum distortion is less than 1 cm for the nominal field map DV02. Table 5.4.2 shows a summary of all calculations. One can see that fast gases have distortions at a level of up to 5 cm, the distortions in the slow gases can be brought to a level of a few mm. The slow gases have clearly smaller distortions, however, one can utilize their advantage only if the background is sufficiently low to allow the total drift times up to 50μs, and the field cage has small distortions. Otherwise, one should use the fast gas. Table 1 shows that for the improved field map DV06, the ALEPH fast gas gives $\sim$ 1 cm of distortion.

Table 12 compares the PEP-N TPC distortions with other typical TPC designs. The table also shows the final reduction factor either already achieved to reach the final resolution. The NA-45 experiment proves that with a very good laser calibration system and with a lot of software effort one can achieve great improvements in the drift distortions [175]. To be able to reach the planned resolution in PEP-N TPC, the experiment needs (a) a good laser calibration system, (b) good external tracking, (c) keeping electrostatic distortions to minimum, and (d) keeping the systematic misalignments to minimum.

One should say that the similar dipole geometry has been tried in the past at LBL [176].

a) Distortions = f(gas choice):

Gas	Field map	E-drift [V/cm]	dx [cm]	dy [cm]
$80\%Ar + 20\%CH_4$	DV.02	400	-4.2	-4.9
$80\%He + 20\%CO_2$	DV.02	400	$-.07$	-0.9
$80\%He + 19\%CO_2 + 1\%CH_4$	DV.02	400	-0.1	-0.91
$80\%He + 15\%CO_2 + 5\%CH_4$	DV.02	400	-0.12	-1.03
$80\%He + 15\%CO_2 + 5\%iC_4H_{10}$	DV.02	400	-0.1	-1.0
$80\%He + 20\%iC_4H_{10}$	DV.02	400	-0.3	-1.5

b) Distortions = f(TPC drift field):

Gas	Field map	E-drift [V/cm]	dx [cm]	dy [cm]
$80\%Ar + 20\%CH_4$	DV.02	400	-4.2	-4.9
$80\%Ar + 20\%CH_4$	DV.02	200	-6.8	-4.2
$80\%He + 20\%CO_2$	DV.02	400	$-.07$	-0.9
$80\%He + 20\%CO_2$	DV.02	200	-0.1	-0.9

c) Distortions = f(field map):

Gas	Field map	E-drift [V/cm]	dx [cm]	dy [cm]
$80\%Ar + 20\%CH_4$	DV.02	400	-4.2	-4.9
$80\%Ar + 20\%CH_4$	DV.03	400	-2.7	-2.9
$80\%He + 20\%CO_2$	DV.02	400	$-.07$	-0.9
$80\%He + 20\%CO_2$	DV.03	400	$-.04$	-0.5
$80\%Ar + 20\%CH_4$	DV.06	400	-1.0	-1.04
$80\%He + 20\%CO_2$	DV.06	400	$-.08$	-0.25

Table 11: Summary of distortion calculations in the PEP-N TPC for electron drift of 50 cm at radial distance of 50 cm.

a) DV02 field map (initial design):

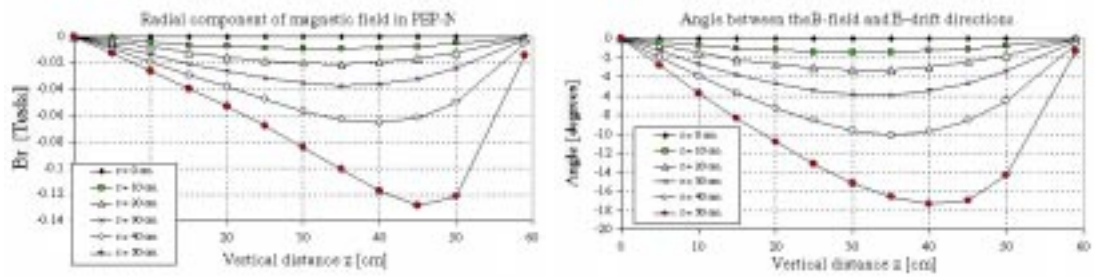

b) DV03 field map (iteration #1):

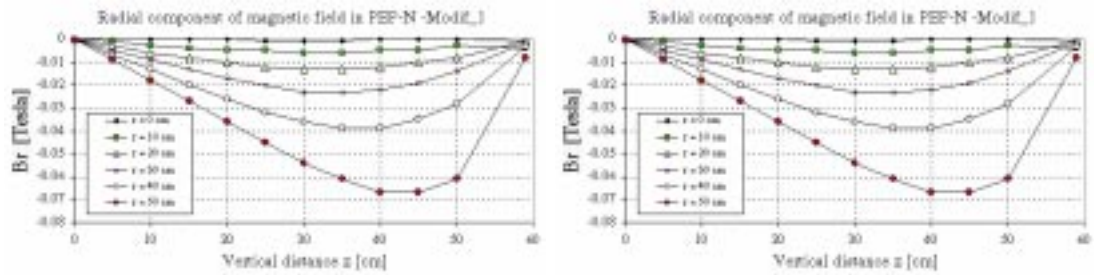

c) DV06 field map (the best design by the time of the workshop):

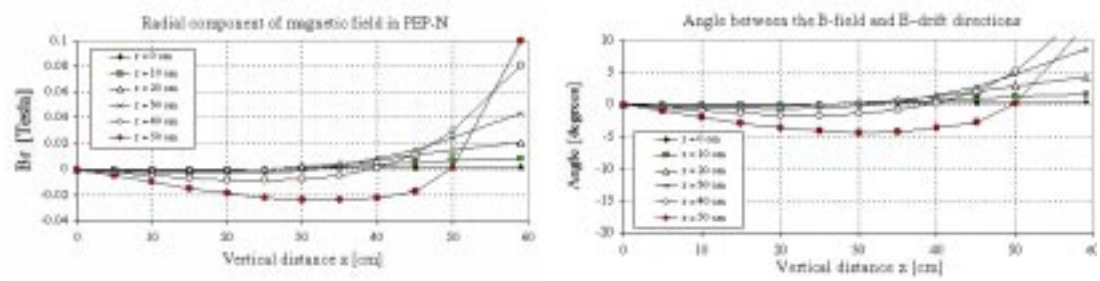

Figure 52: Prediction of magnetic field uniformity in the dipole magnet for three proposed solutions.

5.4.3 Expected Resolution Per Single Point

Following Bloom and Ronaldi [177], one arrives to the following expression for the single resolution point in the TPC with a typical wire & pad design:

$$\sigma^2_{\text{resol}} \approx \frac{1}{N(h,w,b,\sigma_{\text{single}})}\frac{\sigma^2_{\text{single}}}{\cos^2\alpha} + \frac{b^2(\tan\Theta - \tan\Psi)^2\cos^2(\Theta-\alpha)}{12N_{\text{eff}}(h,w,b,\sigma_{\text{single}})} \tag{11}$$

where

σ_{single} - single electron transverse diffusion,

h - pad length,

w - pad width,

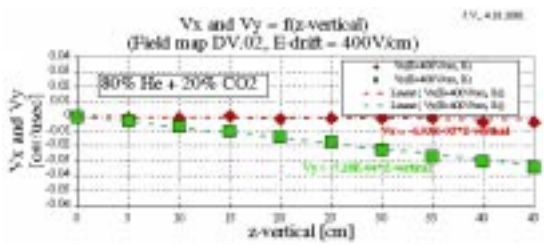

(a)

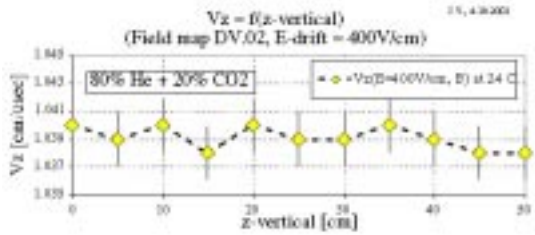

(b)

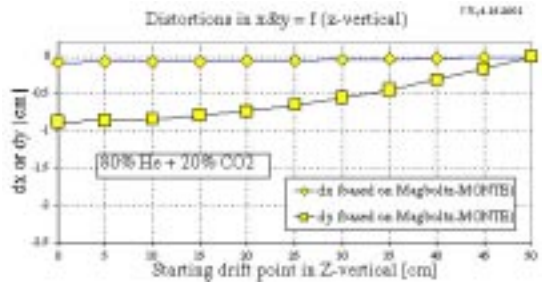

(c)

Figure 53: Calculation of the drift velocity components using the Bagboltz-MONTE program (a,b) and result of the subsequent numerical calculation of distortions in the detecting plane for a drift of 50 cm at radial distance of 50 cm, and for the magnetic field map DV02.

b - wire pitch,

$N(h)$ - effective number of electrons per sample,

$\mathrm{N_{eff}}(h)$ - effective number of clusters per sample.

Figure 54 shows the wire, pad and track geometry needed to understand the resolution Equation (3) for the TPC design employing the standard wire/pad design. Figure 55 shows the application of this equation to the PEP-N design, assuming the following parameters: 53 electrons/sample, 19 clusters/sample, drift of 50 cm, single electron diffusion of $450\mu m/\sqrt{\mathrm{cm}}$, wire pitch of 0.4 mm, pad length of 3 cm, pad width of 0.5 cm and magnetic field of 0.32 T. One can see that resolution blows up at large Θ and α angles as is typical in the standard TPC designs. Table 3 summarizes the expected number of electrons and clusters in various gases, which is useful if one would want to consider the He-based gases. If one would use a conventional fast gas, it is possible to choose a smaller pad size. The 3 cm pad length is probably necessary for the He-based gases.

TPC	Maximum distortion [cm]	A final reduction factor achieved
CRID	~ 1	~ 10
STAR	$\sim 0.2 - 0.3$	~ 5
NA-45	~ 11	$\sim$ 600 within a factor of 2 of achieving this)
PEP-N	~ 1 (fast gas, DV.06)	$\sim$ 50 (planned)
PEP-N	~ 0.2 (slow gas, DV.06)	$\sim$ 10 (planned)

Table 12: Typical maximum distortion in various TPC designs and a final reduction factor achieved to get a final required resolution.

Gas	No. of electrons per 3 cm sample	No. of clusters per 3 cm sample
$80\%Ar + 20\%CH_4$	~267	~74
$80\%He + 20\%CO_2$	~78	~28
$80\%He + 19\%CO_2 + 1\%CH_4$	~77	~28
$80\%He + 15\%CO_2 + 5\%CH_4$	~72	~27
$80\%He + 15\%CO_2 + 5\%iC_4H_{10}$	~98	~36
$80\%He + 20\%C_4H_{10}$	~158	~58

Table 13: Typical expected number of electron and clusters in various gas candidates for the PEP-N TPC.

So far, we assumed the detector based on a standard TPC readout based on the wires and pads such as STAR TPC [178]. However, recently new technologies emerged. For example, if one would use a wireless design based on the GEM concept, the second term in the resolution equation would not contribute at all.

5.4.4 Triple-GEM Detector with Pads

In view of the resolution argument presented in the previous section, it is tempting to propose the detection design with no wires. On could consider, for example, a detector based on three GEMs in tandem with a pad readout shown in Figure 56. The GEM concept was pioneered by F. Sauli [179] and is being used in the COMPASS experiment [180].

The tracker for the COMPASS experiment at CERN includes twenty Triple-GEM

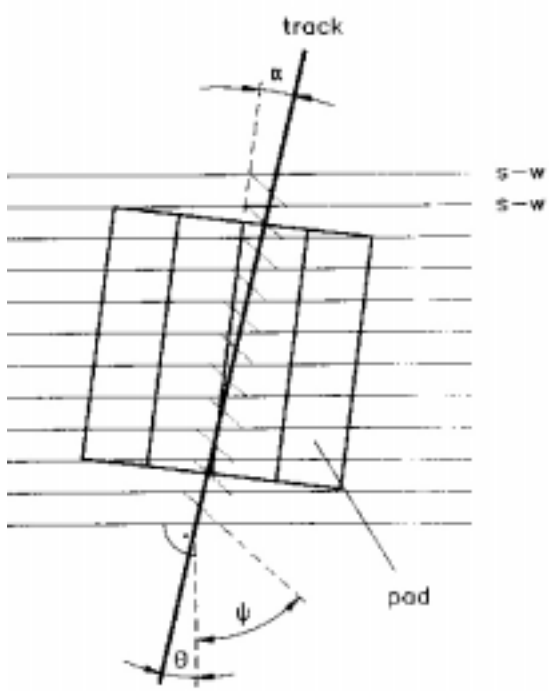

Figure 54: Track, pads and wires and angles needed to understand the resolution calculation.

chambers, mounted in pairs (rotated by 45deg). Each chamber has an active are of 31×31 cm^2 and two-dimensional projective read-out. At the present day, and after extensive prototyping, ten chambers have been manufactured and tested, and are being installed in the experiment; ten more are in construction. The major experimental requirements, that affected the detector design, are:

- High rate capability: the primary beam has $2{\cdot}10^8$ particles per 2.2 s spill, and crosses the central region of the chamber (that can be disabled, see later). Integral event rates exceed one MHz over the active area.
- High background levels, particularly of heavily ionizing tracks (showers, neutron conversions, nuclear fragments).
- Very light construction required, to reduce secondary interactions.
- Two-dimensional coordinate readout with good space accuracy ($\sim 50\ \mu$m) and good multi-track resolution (¡ 1 mm).
- Operation in non-flammable gas (for safety reasons): Ar-CO2 70-30

The requirements have led to the choice of the triple-GEM geometry, with an assembly scheme making use of light honeycomb plates and thin frames with internal spacers to preserve the thin gaps uniformity. The total thickness of a chamber is 9 mm, with 3 mm drift and conversion and three 2 mm gaps between electrodes (Fig. 56). The GEM electrodes are segmented in 12 partitions, individually powered through protection

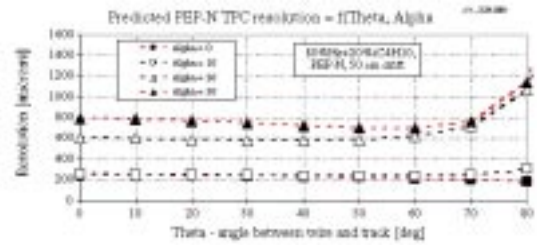

(a)

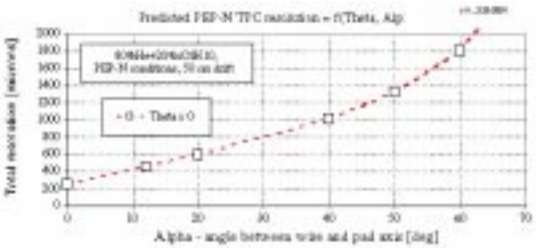

(b)

Figure 55: Predicted resolution per sample in the PEP-N TPC in a slow 80%He + 20%C_4H_{10} gas a function (a) Θ and (b) α angles, defined in Figure 54.

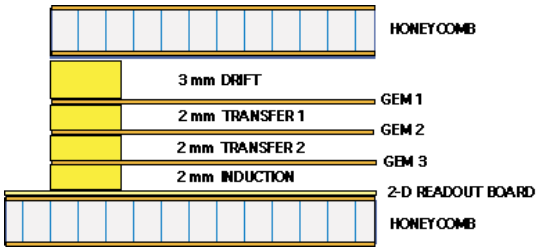

Figure 56: Schematics of the Triple GEM detector.

resistors, to prevent damages due to accidental discharges; a central circular partition permits to de-activate the beam area. The last electrode is a special 2-D readout board, with 720 strips per projection at 400 μm pitch.
The gain of each production chamber is mapped in before final assembly; Fig. 57 gives a typical gain curve. The uniformity of gain over the full area is $\pm 15\%$, due to the accepted tolerance in the GEM hole diameter in manufacturing.

The readout electronics makes use of the APV25 128-channels chip, with 128-deep analogue memory where the input charge on each strip is sampled and stored every 25 ns. Fig. 58 gives efficiency and signal/noise recorded in a beam run. Full efficiency for minimum ionizing tracks (in 3 mm of gas) is obtained at a gain of $8{\cdot}10^3$ ($4{\cdot}10^3$ per coordinate). The cluster size for perpendicular tracks is around 3 strips over threshold (1.2 mm). A very good correlation in recorded charge on the two projections allows to resolve most of the ambiguities of the projective readout.
The discharge probability as a function of gain and conditions has been studied exposing the chambers to heavily ionizing alpha particles, emitted internally by the decay of ^{220}Rn

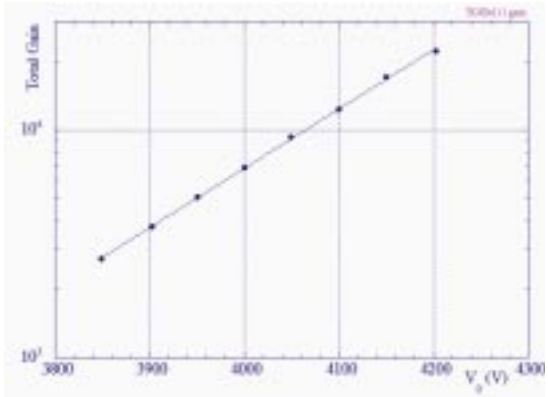

Figure 57: Typical gain dependence on operating voltage.

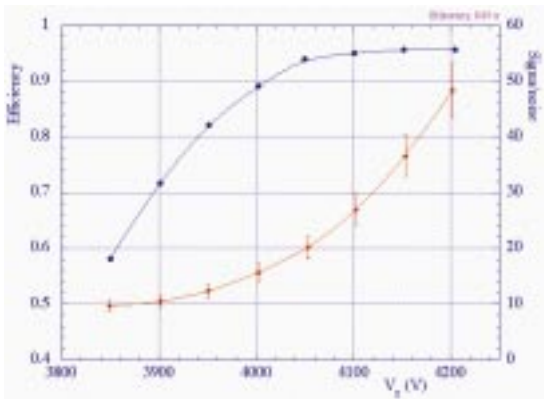

Figure 58: Efficiency and signal/noise vs voltage for one coordinate.

added to the gas. The probability has a strong dependence on the balance of voltage in the three GEMs, the condition of higher gain in the first being the most favorable; Fig. 59 shows an example of discharge probability on alphas as a function of gain for symmetric (A=0) and asymmetric voltage. Note that at the operating gain (8000) the discharge probability is not measurable. During these studies, discharges were repeatedly induced in the large T-GEM chambers, without any damage. This is a consequence of the choice of sector size, external fields and power supply scheme.

In summary, the GEM manufacturing technology is now well developed, with production of large foils consistently of good quality. Operating performances of large area GEM detectors are well understood and satisfy the experimental requirements.

Use of a dedicated GEM structure for signal readout in a TPC has a number of advantages as compared to a classic MWPC:

- Simplicity of assembly (foils against wires); no edge problems.
- Complete symmetry in coordinate localization properties in the plane of readout; the geometry of the readout pad row can be optimized according to requirements,

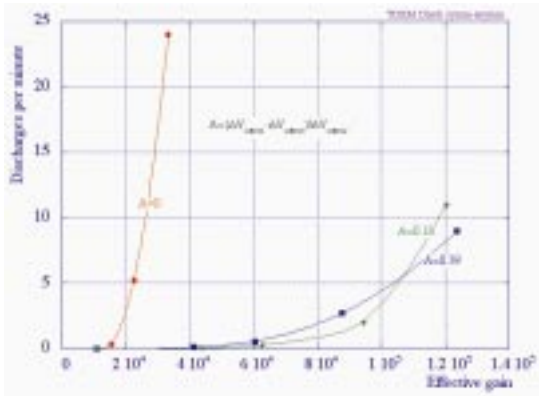

Figure 59: Discharge probability vs asymmetry of voltage on GEMs.

and even varying across the detector.

- Virtual absence of ExB effects.
- Strong reduction of positive ion feedback in the drift volume: $\sim$ 98% suppression has been measured in standard conditions, and optimization of geometry and fields should bring this above 99%.
- If needed, gating of the first GEM is very easy and only requires about 100 V for complete feedback suppression.
- Direct ionization in the end cap section (after the first GEM) is not detected.
- Narrower width of the pad response function; adjusting gaps and fields, it can be adjusted from below one mm to 4-5 mm. This results in an improved two-track resolution.
- The detected signals are only due to electron collection: no ion tails. This results in better time response and resolution. Moreover, signals provided by close track segments are clean, as there is almost no cross-talk due to induced signals.
- Odd shapes are easy to make, simply designing the GEM foils as desired.
- Long-term operation: GEM detectors have been demonstrated to be far less sensitive to aging problems than any other micro-pattern device.

The technology has some possible disadvantages:

- Gain uniformity: as indicated, the present manufacturing technology results in a spread of gain around the surface of about 30%. This can be however mapped and corrected. Presumably, the system of laser calibration needed to map the magnetic field distortions will also allow correcting for gain variations.

- Charging-up: to obtain a good yield, the etching process used to make holes in kapton produces slightly double-conical holes. These charge up when exposed to radiation with a gain increase of about 30%. Some improvement in quality control during manufacturing should allow to obtain conical holes, non-charging up.

- Reliability: originally considered fragiles because of damages produced by discharges, the improvement in design and operation of GEMs has to a large extent eliminated this problem. Further tests in the TPC geometry and conditions are however needed.

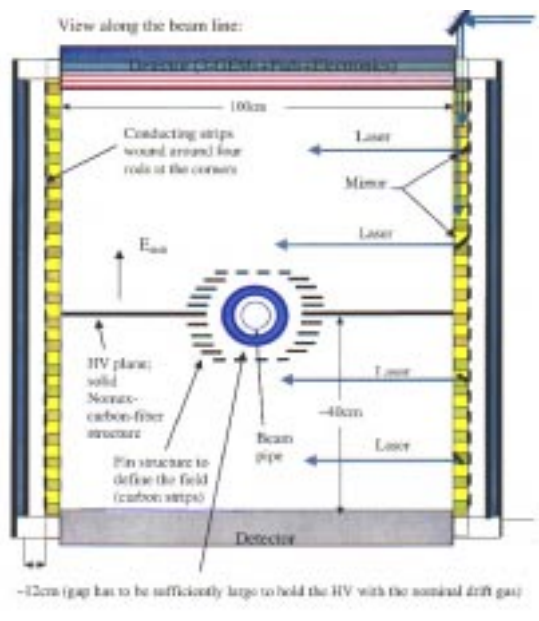

(b)

Figure 60: Field cage–a view along the beam pipe. The field cage is assumed to be built as one unit around the trapped section of the beam pipe to minimize the systematic misalignments. The central HV plane is solid Nomex carbon fiber structure. There are two identical detector sections, each containing nine segments of the triple-GEM detectors with pad readout.

To guard against damages, one would want to run at as small gas gain as possible, i.e., less than $2 - 3 \times 10^3$. As an example, PEP-N would have $\sim 3 \times 53$ electrons per 3 cm-long sample in 80%He + 20%iC_4H_{10} gas. With gas gain of 2×10^3, it will have $\sim 3 \times 10^5$ electrons available to the amplifier input, which should be possible to obtain a good measurement provided that the electronics noise is kept near $\sigma_{\text{noise}} \sim 1000$el. In PEP-N TPC, one can use longer shaping times (200–250ns).

The gating would be necessary only if the backgrounds would be very large.

One could choose the COMPASS experiment size GEM foil, which would fit well the field cage design proposed in the next chapter.

5.4.5 Field Cage Design

The field cage design is extremely critical for the successful operation of the PEP-N TPC, especially, if one decides to use the slow gases. After considering several possible design choices, I would propose to follow ideas from the ALICE TPC design, which is the most recent TPC application. The main reason is that it provides a very low mass for low energy particles, which is very important for the PEP-N experiment, and also it provides a convenient way to introduce multiple laser beams for the calibration purposes.

The proposed field cage design is shown in Figures 60 and Figure 61. The aluminized Mylar strips are wound around four ceramic rods. With a single layer of these strips, the expected electric field distortions are expected to be less than 10^{-4} about 2 cm away from the strips in the ALICE design [181]. The TPC high voltage central plane made of solid Nomex carbon fiber structure, the effect of the grounded beam pipe is de-coupled with field cage structure made of solid self-supporting carbon strips. The laser beams are distributed into the TPC volume by reflections from many mirrors placed in the ceramic rods. The outer field cage is surrounded with a grounded cage made of Hexel panels, which also served as gas envelope. Figure 7 shows the top view and indicates the modular structure of the GEM detectors. The size is chosen to be that same as the COMPASS experiment [180] to simplify the production. The individual modules are identical to allow easy maintenance.

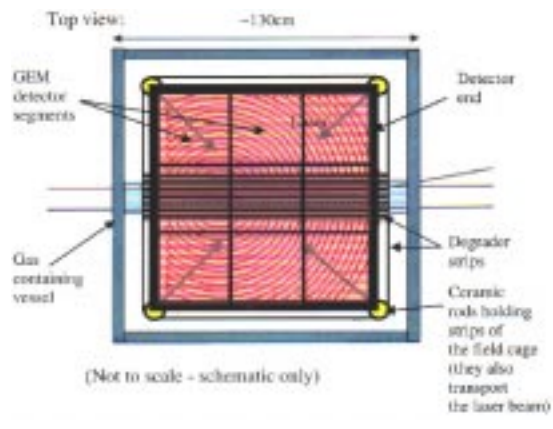

(b)

Figure 61: Field cage–top view. The picture also shows the radial pattern of the GEM readout strips ($\sim$ 3 cm long, $\sim$ 5 cm wide), carbon strips along the beam line, field cage with ceramic rods and Mylar strips, and outer Hexel gas containing enclosure.

In summary:

- The present design seems to be practical.
- The detector is using a novel triple-GEM structure with the pad readout, which would eliminate the wire-induced $E \times B$ resolution degradation in the detecting plane. It is proposed to use the COMPASS experiment [180] size GEM foils, which would mean $2 \times 9 \times 3$ of such foils per entire PEP-N TPC readout.

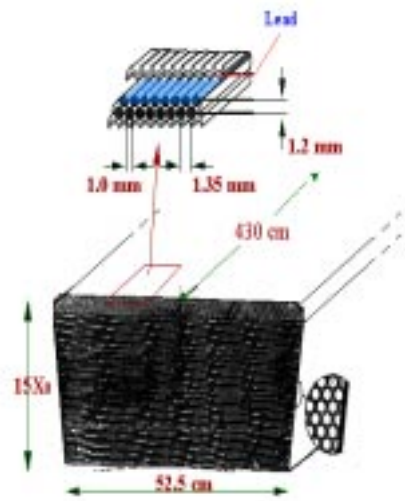

Figure 62: Sketch of a lead-scintillating fiber module.

- The maximum predicted distortions are less than 1 cm for the fast gases using the DV.06 field map, and less than a few mm for the slow gases. This means that the fast gases are the option if necessary.
- The expected resolution is about 300μm per single point in track.
- The typical track has 15 points, each sampled with a pad length of 3 cm, which should allow to use the He-based gases.
- The field cage design follows the ALICE design which provides a low mass and easy entry of the laser calibration beams into the TPC volume.
- The capability of a TPC concept to handle a very large number particle densities was clearly demonstrated by the STAR [177] and NA-49 [182] TPC detectors. This is because of a very low gas gain operation reducing the avalanche saturation effects and the ion field distortions to minimum.

5.5 The PEP-N electromagnetic calorimeter

Simulation studies for the R measurement lead to the following minimal requirement for PEP-N calorimeter:

- Hermeticity, in order to have high acceptance for all final states.
- Full efficiency for photons down to 20 MeV.
- Good (few %) energy resolution for photons.

- Good time resolution and good efficiency for $\overline{N}$ in order to identify n$\overline{\text{n}}$events.

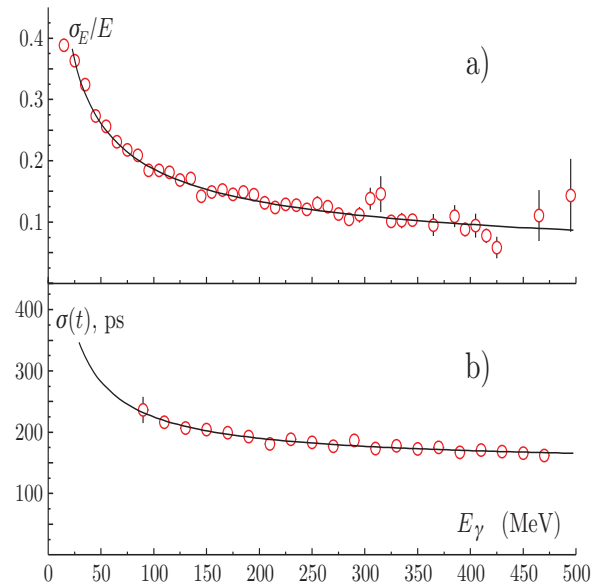

Figure 63: Energy and time resolutions as function of the photon energies.

As a guide for our design we have considered the KLOE electromagnetic calorimeter[183] that has been successfully operating at DAΦNE since 1998, detecting photons in a similar (20-500) MeV energy range. This detector provides a fast and unbiased first level trigger for KLOE, with high acceptance for final states with low energy photons.A good K/π separation has been achieved and also some attempts at π/μ discrimination have been made.
The KLOE calorimeter is a fine sampling lead and scintillating fibers calorimeter. The barrel modules have trapezoidal cross section, 4.3 m long, 60 cm wide and 23 cm thick. Each module is obtained gluing 0.5 mm thick lead foils worked to house the 1 mm diameter fibers. The resulting structure (Fig. 62) has fiber:lead:glue volume ratio of 42:48:10, an average density of 5 g/cm^3, a mean radiation length 1.5 cm, and a sampling fraction of $\sim$ 15% for minimum ionizing particles. The readout granularity is $\sim (4.4 \times 4.4)$ cm^2, for a total number of 4880 read-out channels. A precision in measuring the photon conversion point in the direction perpendicular to the fibers (transverse direction) $\sigma_{\rm t} = 1.0\,$cm has been achieved.The coordinate along the fiber (longitudinal direction) is measured using the relation: (x,y) $= \mathrm{v}_f \cdot \frac{\Delta T}{2}$, with ΔT the time difference at the two module ends and v_f the effective light propagation speed in the fibers. The measured effective light propagation speed is $v_f = 17.2\,$cm/ns. The obtained performances (Fig. 63) are summarized as follows:

- detection efficiency for photons with energy between 20 MeV and 500 MeV of about 99%.

- resolution in the photon conversion point position in the transverse direction of $\simeq 1$ cm and in the longitudinal direction (x,y) $\sigma_{\rm x,y} = \frac{1.24\,\rm cm}{\sqrt{E(\,\rm GeV)}}$.

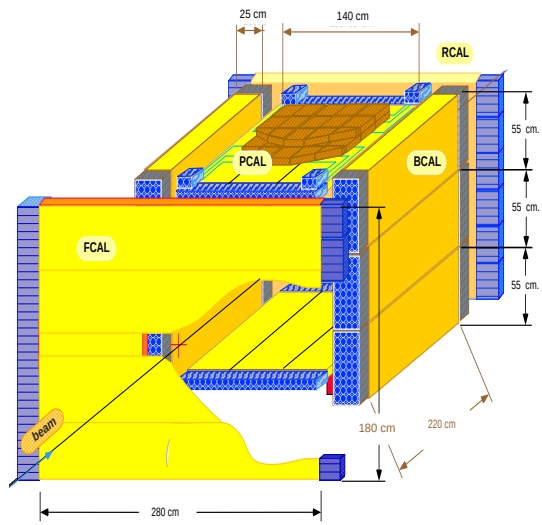

Figure 64: Exploded view of the PEP-N calorimeter.

- energy resolution $\frac{\sigma_E}{E} \simeq \frac{5.7\%}{\sqrt{\mathrm{E(GeV)}}}$.
- time resolution $\sigma_t \simeq \frac{54\,\mathrm{ps}}{\sqrt{\mathrm{E(GeV)}}} + 50\mathrm{ps}$.

The calorimeter is inside a 0.6 T magnetic field with a consequent residual magnetic field up to 0.2 T in the photomultipliers (PM) area and with an angle with respect to PM axis up to 25°; for this reason fine mesh photomultipliers, Hamamatsu R5946, were specially designed for KLOE.

5.5.1 The design

In Fig. 64 an exploded view of the calorimeter design is shown. It consists of barrel, forward and backward detectors.

- Each of the vertical sides of the *barrel* have 3 modules with rectangular cross section, 220 cm long, 55 cm high and 23 cm thick (15 r.l.), with fibers parallel to the beams (BCAL detector). Also the horizontal sides have 3 modules 220 cm long, 50 cm wide, 15 cm thick, positioned above and below the TPC chamber, in order to complete the coverage of the azimuthal acceptance (PCAL detector). The angular region covered by the barrel modules is $27° < \theta < 135°$.

  Due to space limitations the PCAL detector is only 15 cm thick (10 r.l.). The efficiency, simulated with Monte Carlo, is shown in Fig. 65. The efficiency is greater than 99% for energies higher than 40 MeV. The gamma energy resolution is $\frac{\sigma_E}{E} \simeq \frac{11\%}{\sqrt{\mathrm{E(GeV)}}}$.

  With the DV07 magnet design it is possible to increase the PCAL energy resolution, by instrumenting it with tile type modules , similar to the QCAL detector that is

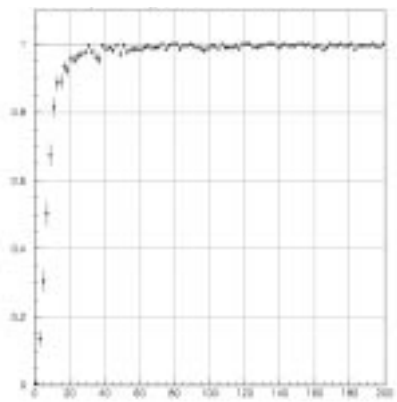

Figure 65: Efficiency for PCAL detector.The γ energies are in MeV.

taking data in KLOE with good performances (Fig. 66) [185]. Each module, 6 cm wide and 220 cm long, is made of 15 scintillator layers, 1 mm thick and 16 lead planes, 2 mm thick, resulting in five additional radiation lengths for normally incident photons and a total thickness of 5.2 cm.The scintillator layers are divided into 3 equal tiles, so 4, 220 cm long WLS fibers run along the sides of the tiles for a total of 60 WLS fibers per module. The light is collected with PM from both ends.

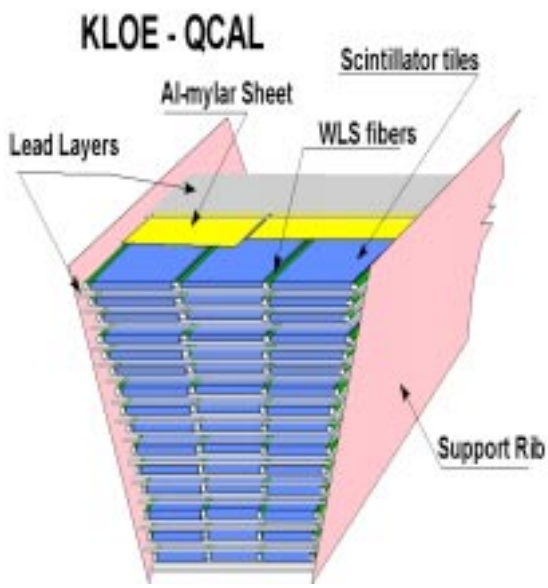

Figure 66: Design of the KLOE tile module QCAL.

- The *forward detector* (FCAL) modules are 30 cm thick (20 r.l.). They are located at ($130 < z < 155$) cm, cover an area of $280\times180\text{cm}^2$, with polar angle range $6^\circ < \theta < 27.5^\circ$ (Fig. 67).

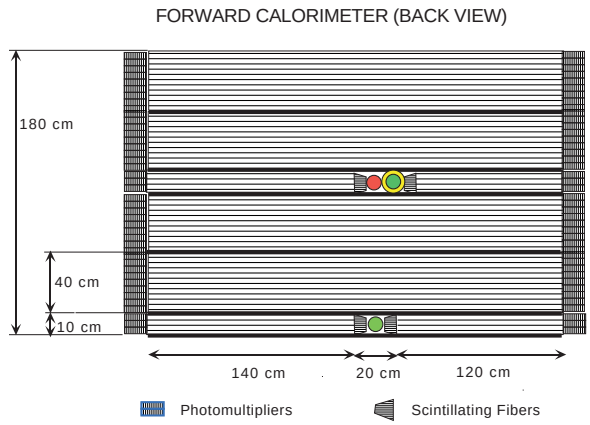

Figure 67: FCAL detector.

	DX	DY	DZ	Mod.	Photom.
PCAL	50	15	220	6	10*3*2*6
QCAL	120	5.2	220	40	20*1*2*2
BCAL	25	55	220	6	11*5*2*6
FCAL	280	40	30	4	8*6*2*4
	120	10	30	1	2*6*2*1
	100	10	30	1	2*6*2*1
	140	10	30	2	2*6*2*2
RCAL	120	54	15	2	11*3*2*2

Table 14: Sizes(cm),modules and photomultipliers for each detector.

- The *backward detector* (RCAL) is composed of 2 modules positioned at z= -140 cm. They are 120 cm long, 54 cm high and 15 cm thick, specially designed to detect very low energy photons. The total area covered is 120×120 cm^2 ($135^\circ < \theta < 180^\circ$).

In Table 5.5.1 the dimensions, number of modules and number of photomultipliers requested are summarized. We have assumed the same readout granularity as KLOE, that is $\sim (4.4 \times 4.4)$ cm^2, so that the total number of photomultipliers is 1712.

5.5.2 Calorimeter performances

The inclusive photon energy distributions in the four detectors, at $E_{cms} = 2.25$ GeV, are shown in Fig. 68. Since average photon energies are higher than in KLOE we expect better performances. The energy and the spatial resolutions are also better because, compared to the 4.3 m of the KLOE modules, BCAL and PCAL are only 2.2 m long and RCAL is even shorter (120 cm). The gain in photoelectrons can be estimated from the attenuation curve to be about 30% ; thus we obtain for BCAL, RCAL,PCAL (if equipped with the tile modules):

- energy resolution $\frac{\sigma_E}{E} \simeq \frac{5.0\%}{\sqrt{\mathrm{E(GeV)}}}$.

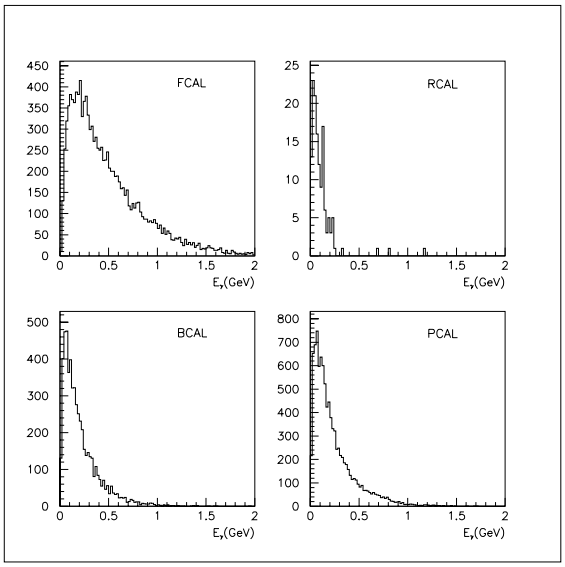

Figure 68: Photon energy distributions in the calorimeters.

- time resolution $\sigma_t \simeq \frac{44\,\mathrm{ps}}{\sqrt{\mathrm{E(GeV)}}} + 50\mathrm{ps}$.
- resolution in the photon conversion point position in the transverse direction of $\simeq 1$ cm and in the longitudinal direction (x,y) $\sigma_{\mathrm{x,y}} = \frac{1.0\,\mathrm{cm}}{\sqrt{E(\,\mathrm{GeV})}}$.

These performances are consistent with the results achieved by KLOE [186].

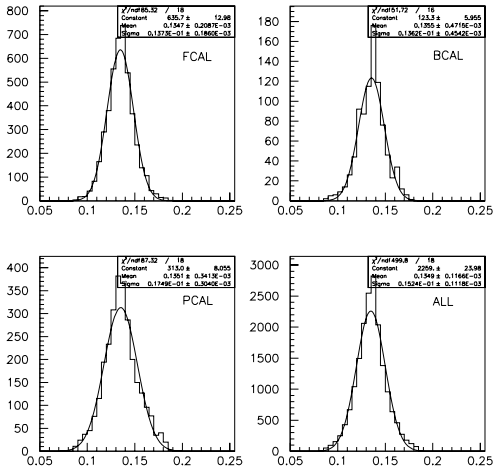

Figure 69: π^0 mass resolution when both photons hit FCAL,BCAL,PCAL (first 3 plots). Taking all photons we get a π^0 mass resolution of 15 MeV/c^2 (last histogram).

The gain for FCAL is only 10% so for this detector we assume the KLOE resolutions. Putting these values in the Monte Carlo, we have studied the calorimeter performances concerning

- π^0 mass resolutions
- K-π separation
- n$\overline{\text{n}}$ detection

π^0 mass resolutions
The π^0 mass resolutions obtained are shown in Fig. 69. In the first 3 histograms we plot the mass resolutions when both photons hit the same detector. Taking all photons we get a π^0 mass resolution of 15 MeV/c^2 (last histogram).
K-π separation
PEP-N is equipped with an aerogel detector for K-π separation in the momentum range ($0.6 < P_{tot} < 1.6$) GeV/c. The TPC chamber can be used to separate particles with momenta lower than 0.6 GeV/c (dE/dX measurement).Unfortunately the TPC measures badly the dE/dX of particles hitting the pole calorimeter PCAL where, due to lack of space, it is difficult to insert a specific particle identification detector. Because of very good time resolution,better than 0.2 ns for m.i.p., TOF information from PCAL can be used. In Fig. 70 the time-momentum separation for the process KK$\pi\pi$ is shown for FCAL,BCAL and PCAL at $E_{cms} = 2.25$ GeV.A 3 σ separation is shown for these process till 0.8 GeV/c momenta.

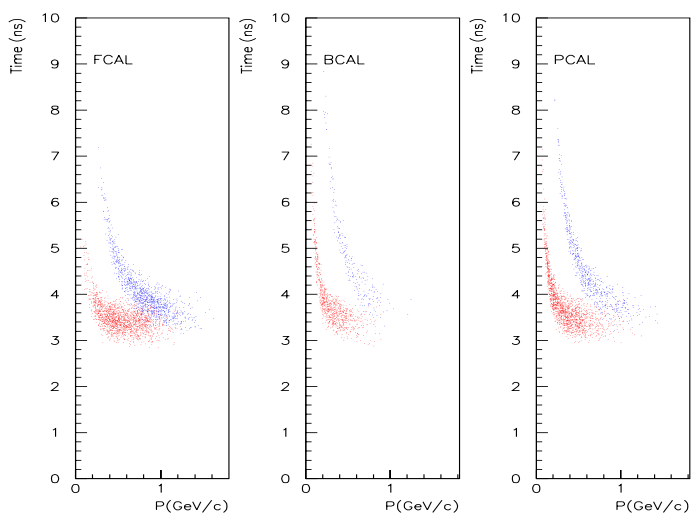

Figure 70: Time(ns) - momentum (GeV/c) correlation for KK$\pi\pi$ events for FCAL,BCAL and PCAL at $E_{cms} = 2.25$ GeV.

$n\overline{n}$ detection
In addition to the neutron form factor measurement the possibility to use the forward calorimeter to detect $n\overline{n}$ events is particularly interesting because 2% of the contribution to the hadronic cross section comes from this process. To this purpose neutrons and antineutrons have been generated impinging perpendicularly on FCAL. They are considered detected when at least 50 MeV energy release is observed in a cone surrounding

P (GeV/c)	Neutrons	Antineutrons
0.5	0.18	0.94
1.0	0.42	0.86
1.5	0.49	0.83

Table 15: Neutron and antineutron efficiency as a function of the particle momentum

the particle direction. Table 15 gives the observed efficiency for both particles for three momentum values.Antineutron detection seems to work rather well, while neutron efficiencies are lower and strongly dependent on the impinging particle momentum. Most of the efficiency loss for neutrons is due to neutrons that do not interact at all (between 25% and 40%, decreasing with momentum) and that give very small and not easily detectable energy releases.

Figs. 71 and 72 show energy and velocity spectra for antineutrons and neutrons at three values of momentum. Velocity is measured using a 2 m long flight distance. All quantities are well measured for antineutrons but not for neutrons.
These studies indicate that the proposed calorimeter, based on the KLOE design, can be used both for the detection of hadronic events for the measurement of R and of $n\overline{n}$ events for the form factor measurement. The detector in its present design provides very good antineutron detection. In order to increase the efficiency for neutrons a careful optimization of the detector parameters has to be done.

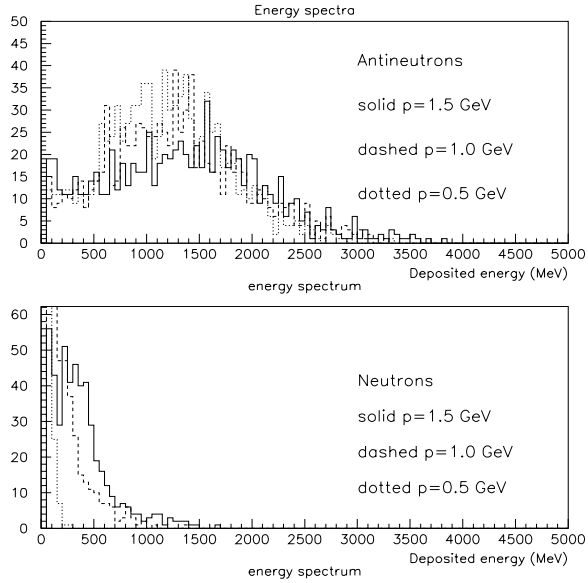

Figure 71: Antineutrons and neutrons released energy spectra at the three values of momentum.

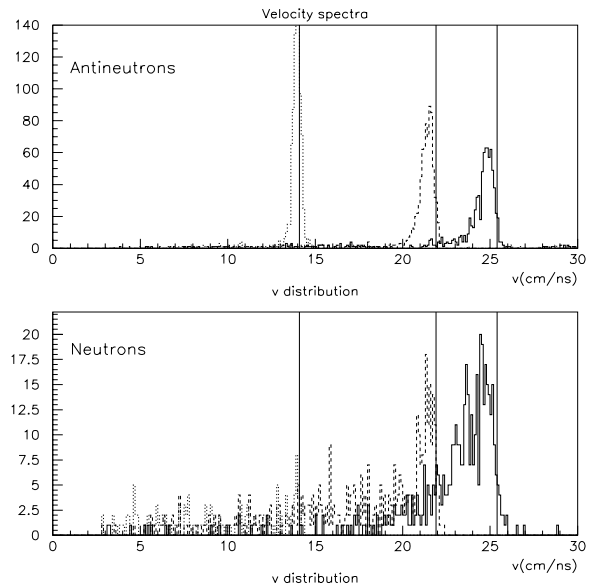

Figure 72: Antineutrons and neutrons velocity distributions. Particles have a 2 m long flight path. The solid vertical lines correspond to the true values of velocity at three momenta.

5.6 Aerogel detector

The idea of the method is to use light guides with the wavelength shifting admixture for light collection on PMT (ASHIPH technique) [187]. As compared with the direct light collection on PMT, this method allows the number of PMTs to be reduced drastically [188, 189, 190, 191].

In order to simulate the processes of light collection and propagation inside the aerogel Cherenkov counter a special code was developed in Budker Institute of Nuclear Physics [192, 187, 193]. This code simulates the following processes: Rayleigh scattering inside the aerogel, Lambert angular distribution of the reflected light from the walls, Fresnel refraction on the boundary of two continuous media, and a light absorption inside the aerogel and on the walls. Using this code we optimize the counter design and calculate the number of photoelectrons without production of series of prototypes.

The ASHIPH system [191] is being used for the KEDR detector [194]. It consists of 160 counters: 80 barrel and 80 endcap counters (Figure 73). The total volume of aerogel is 800 liters. The use of aerogel with the refractive index 1.05 gives the possibility to separate pions and kaons in the momentum range $0.6 \div 1.5$ GeV/c.

The detector uses the aerogel SAN-96 [195, 196, 197] produced at Novosibirsk by collaboration of Boreskov Institute of Catalysis and Budker Institute of Nuclear Physics. The data on the light absorption (Labs) and scattering (Lsc) lengths in the SAN-96 aerogel are shown in Figure 74,compared with aerogel samples produced at KEK(Japan) [198].

An important feature of the detector is a two-layer design. The counters are arranged in such a way that a particle from the interaction point with a momentum above 0.6 GeV/c does not cross shifters in both layers simultaneously. It is possible to use the information from both layers for the majority of particles.

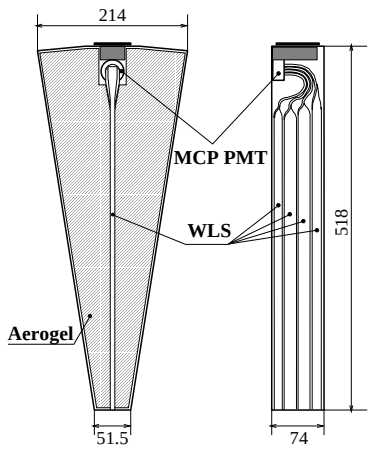

Figure 73: The endcap ASHIPH counter of the KEDR detector.

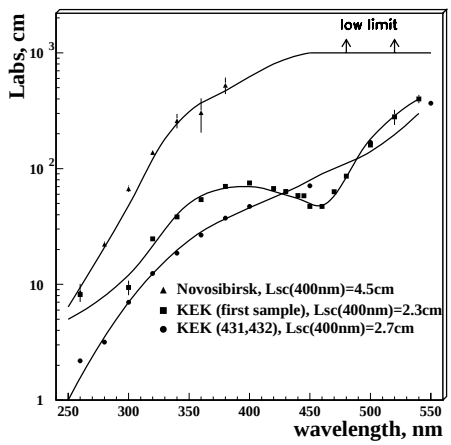

Figure 74: Labs and Lsc for Novosibirsk and KEK aerogels (see text).

The multi-layer PTFE film from Tetratex is being used as a reflector. The results of measurement [188] of the reflection coefficient for the different thickness of reflector are shown in Figure 75. The PTFE teflon has four times larger radiation length than the KODAK paint,therefore the use of teflon reduces significantly the amount of material in front of the calorimeter.

The absorption spectrum of BBQ is shown in Figure 76 together with the spectrum of collected Cherenkov photons and the absorption spectrum of POPOP (KN-18). The production of plexiglass plates doped with BBQ was mastered in Institute of Polymers at Dzerzhinsk. The cutting, polishing, and twisting were organized in Budker Institute of Nuclear Physics.

The readout of the detector is performed with microchannel plate (MCP) PMTs with multialkali photocathode produced in Novosibirsk by “Ekran” plant [190, 191]. The size of this device is small: 31 mm diameter and 17 mm thickness. The photocathode is 18 mm in diameter. Our measurements of quantum efficiency (QE) of this PMT and the

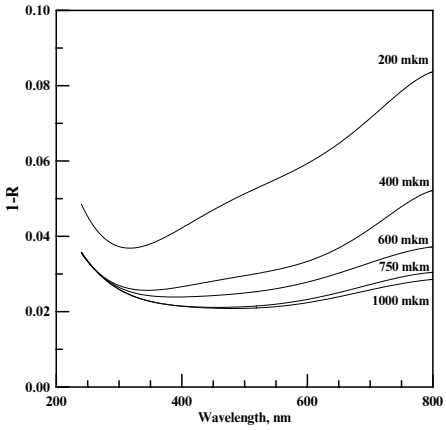

Figure 75: Reflection R of PTFE teflon.

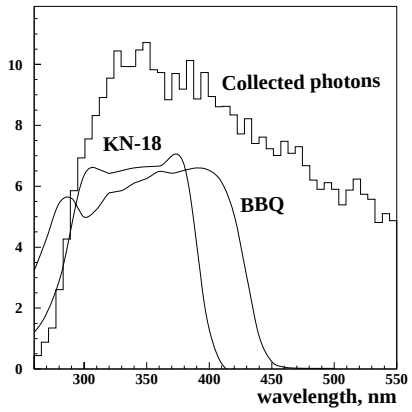

Figure 76: The absorption spectra of BBQ and KN-18 (POPOP) wavelength shifters, collected Cherenkov photons spectrum.

FM PMT R6150 are shown in Figure 77. The shift of spectral response to the region of longer wavelengths is the essential advantage of MCP PMTs in respect of detecting BBQ emission.

The decrease of MCP PMT multiplication gain in high magnetic field is not so strong as for fine mesh PMTs of Hamamatsu. In the magnetic field of 1.5 Tesla the gain drops in some 5 times.

The amount of material in the KEDR ASHIPH system is 24 % of a radiation length.

The endcap counters of the KEDR detector were tested on the particle beam at the Dubna accelerator.

The dependence of the detected Cherenkov light on momentum was measured with pions (Figure 78). The theoretical fit to the experimental point gives the resulting number of photoelectrons at $\beta = 1$ as 10.6 pe.

The homogeneity of the light collection was measured with the 0.83 GeV/c pions over the whole area of the counter. As shown in the Figure 79, the signal varies from 7.1 pe

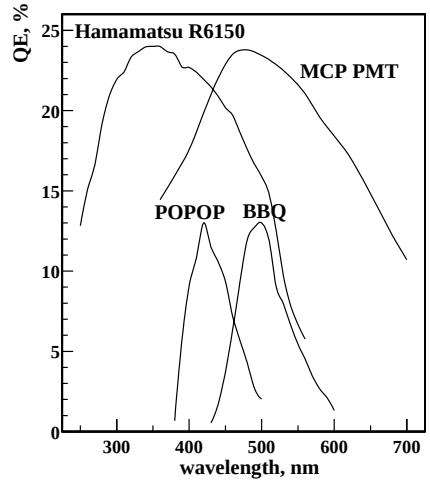

Figure 77: Hamamatsu R6150 $N^{\underline{o}}$ZH2673 and Katod MCP PMT $N^{\underline{o}}$1570 quantum efficiencies. POPOP and BBQ emission spectra.

up to 9.7 pe.

Figure 80 illustrates kaon and pion amplitude spectra obtained from the counter at P=0.86 GeV/c.

In Figure 81 the probabilities of kaon and pion misidentification are shown as a function of threshold for 0.86 and 1.2 GeV/c momenta. For 0.86 GeV/c at the zero threshold on the amplitude the signal pion suppression factor is 860, with kaon detection efficiency being equal to 94% (separation is 4.7 σ). And for 1.2 GeV/c pion suppression factor is 1300, with kaon detection efficiency being 90% (4.5 σ).

5.6.1 ASHIPH for PEP-N

The Aerogel Cherenkov Counter system is provided for π/K separation in the forward direction of the detector.

The proposed system is analogous to the KEDR ASHIPH system. Total volume of aerogel is 350 liters. We suggest to use MCP PMTs in the counters. The refractive index of aerogel is 1.05. This provides the π/K identification in the momentum range from 0.6 to 1.5 GeV/c. Identification below 0.6 GeV/c is provided by dE/dX in coordinate system and TOF measurements with calorimeter.

The Monte Carlo calculations were performed for the $e^+e^- \to K^+K^-\pi^+\pi^-$ reaction at $E_{c.m.}$ = 2 GeV. The momentum distribution of kaons in laboratory coordinates is shown in Figure 82. One can see that the identification region of the ASHIPH system covers the main part of the events.

The results on identification acceptance for 4 track events is presented in Table 16. The tracker acceptance for this reaction is 88% for 4 tracks and 12% for 3 tracks.

The amount of material in the PEP-N ASHIPH system is about 20% of X_0.

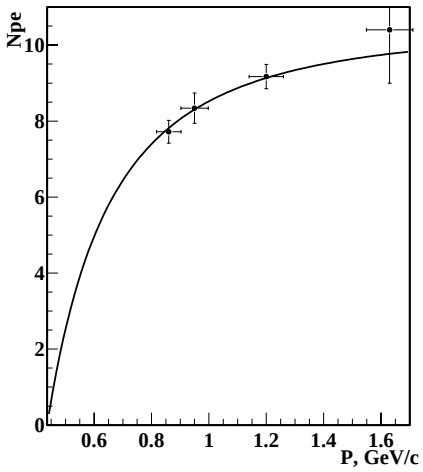

Figure 78: The number of photoelectrons for pions versus momentum. The curve represents the theoretical formula fit.

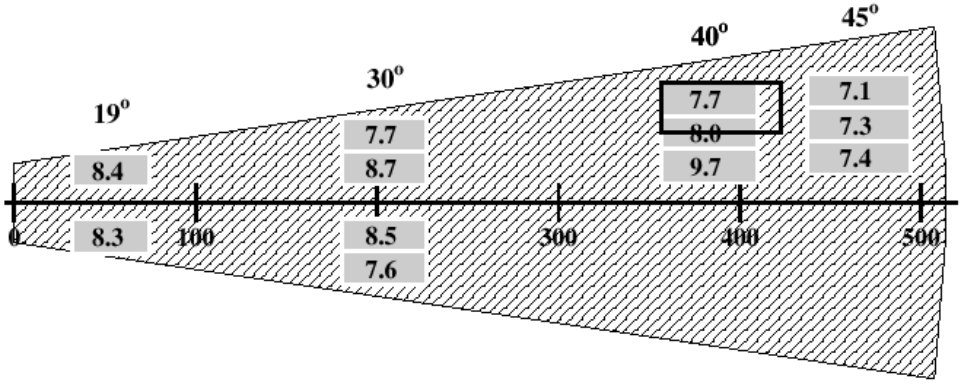

Figure 79: The number of photoelectrons in different points of the counter. The open rectangle designates the area where the π/K separation was measured.

5.7 The luminosity monitor

5.7.1 On-line luminosity

An on-line monitor is required for tuning and monitoring the machine. It is desirable that it provide a measurement with 10% or better accuracy, and fluctuations of less than 1% at a refresh time of less than 1 second. The PEP-II monitor, based on observing single bremsstrahlung at zero degrees to the positron direction at collision, described in Ref. [199] seems appropriate.

Single bremsstrahlung, or radiative Bhabha scattering, has a differential cross section, integrated over electron and positron angles, of:

$$\frac{d\sigma}{d\omega} = \frac{4\alpha r_0^2}{\omega}\frac{E-\omega}{\omega}(V-2/3)[ln\frac{m}{q_{min}} - 1/2] \tag{12}$$

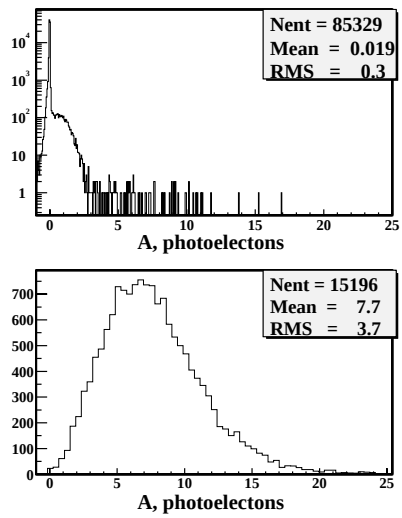

Figure 80: Amplitude spectra for kaons (top) and pions (bottom), P=0.86 GeV/c.

N_{ID}	Identification systems	Acceptance
4	dE/dX + TOF	2%
4	dE/dX + TOF + ASHIPH	48%
≥3	dE/dX + TOF	41%
≥3	dE/dX + TOF + ASHIPH	93%

Table 16: Identification acceptance for 4 track events. N_{ID} is the number of particles identified.

where $V = \frac{E-\omega}{E} + \frac{E}{E-\omega}$ and $q_{min} = \frac{m}{4\gamma^2}\frac{\omega}{E-\omega}$. Here E is the initial electron or positron energy, $\gamma = E/m$ and $r_0 = e^2/m$. The angular distribution of the γs is strongly forward with angular width $\sim \gamma^{-1}$. $\frac{d\sigma}{d\omega}$ is a function only of ω/E so the flux of γs at $\sim 0°$ to the LER is independent of s. For PEP-N conditions we have used the program BBBREM [200] to estimate the cross section for $\omega > 400$ MeV radiation from the e^+ beam to be 76 mb.

The momentum transfer for this process can be remarkably small, corresponding to a very large impact parameter ρ and leading to screening effects which must be taken into account. If we choose E=3 GeV and $\omega > 300$ MeV, $q_{min} = 0.4 \times 10^{-9}$ MeV and $\rho_{max} = 0.05$ cm which is greater than the transverse size of the beams in PEP-N. The consequence is that the cross section is cut off at a momentum transfer $\sim q_{min}$. This problem has been treated by various authors and the following result by Burov and Derbenev is quoted by Ref. [201] for the case of a for a Gaussian beam density where the transverse beam size is smaller than characteristic impact parameters:

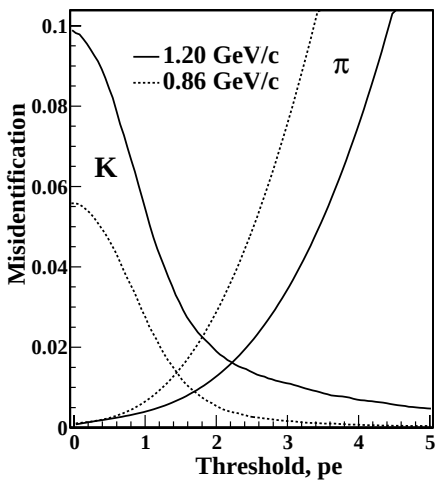

Figure 81: Probability of misidentification for kaons and pions as a function of threshold. P=0.86 GeV/c, 1.2 GeV/c.

$$\frac{d\sigma}{d\omega} = \frac{4\alpha r_0^2}{\omega}\frac{E-\omega}{\omega}(V-2/3)[ln\frac{\Delta_y\Delta_z}{\lambda_C(\Delta_y+\Delta_z)} + ln2 + c/2 + \frac{V-5/9}{V-2/3}] \qquad (13)$$

where $c = 0.577$, Δ_y and Δ_z are the rms transverse beam dimensions; λ_C is the electron Compton wavelength (m^{-1}). The sensitivity of this effective cross section to variation of the PEP-N beam is approximately a 3.5% increase for a doubling of the radius. Despite this modest sensitivity, the dependence on beam size and shape introduces uncertainty that is undesireable for an absolute luminosity measurement. The background to radiative Bhabhas at 0° is synchrotron radiation and beam-gas bremsstrahlung. At PEP-II, a Čerenkov shower counter is used with a threshold sufficiently high to be immune to the SR. The beam-gas background is apparently not a problem.

The interaction region should be designed so that such a monitor can be installed, which requires a clear aperture, suitable window, and space for the monitor. At PEP-II, the monitor is installed at 8 m from the interaction point. We also want this monitor well downstream of the detector.

5.7.2 Off-line luminosity

The accurate and precise determination of integrated luminosity required for the experiment will be obtained from QED processes observed in the detector. We require a 1% or better measurement for each inverse picobarn of running. The available processes are Bhabha scattering and annihilations into muon pairs and gammas. We consider them individually in the context of the standard detector design. Our luminosity determination will be similar to that of BABAR, described for example in Touramanis' talk at the 2/2001 BABAR Collaboration Meeting. The BABAR determination is based on wide-angle ($> 45°$) Bhabhas and muon pairs. The systematic error is contributed to by the Monte Carlo (1-2%) and cut stability (1%), for an overall 2%. The annihilation to 2

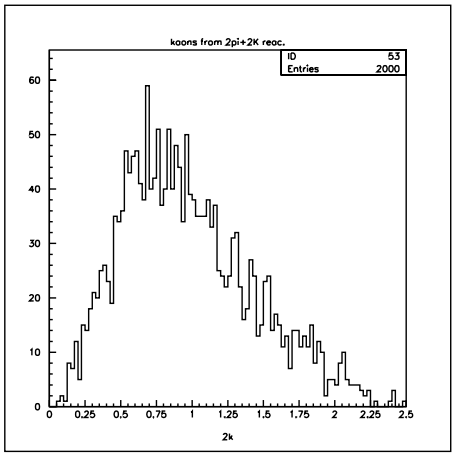

Figure 82: The momentum distribution of kaons in laboratory coordinates in the reaction $e^+e^- \to K^+K^-\pi^+\pi^-$ at $E_{c.m.} = 2$ GeV.

photons has a greater systematic uncertainty, at least 3%, since the event rate is sensitive to mass and the geometrical acceptance is less well defined (angles for photons are not measured as well as those for charged particles).

In PEP-N the experimental situation is somewhat different. Since the calorimeter has relatively coarse spatial resolution ($\sigma \sim 2.5$ cm), it is not possible to accurately define the acceptance for photons, leading to an unacceptably large systematic error for the 2 photon annihilation rate. Since the luminosity is much smaller than for BABAR and we seek 1% uncertainties on a point-by-point basis, we must accept Bhabha and especially muon pair events at smaller polar angles, which requires good angular measurements at small angles to adequately define the acceptance. To obtain a 1% statistical error for each inverse pb we require $> 10,000$ events for an integrated cross section of > 10 nb. On the other hand the PEP-N detector is simpler and we expect to do better in the Monte Carlo simulation, which is the dominant error for the BABAR luminosity. In particular one particle for all Bhabha and muon pair events will be seen by the forward planar tracking chambers and electromagnetic and hadron calorimeters.

5.7.3 Geometry

The detectors used for the luminosity measurement are shown in fig. 83. The beam pipe is assumed to have a 5 cm radius and the default is 1 mm of aluminum. We assume 4π tracking with 200 μm resolution for radii < 60 cm , planar forward tracking with 200 μm resolution at z=120 cm with unhindered aperture of $\pm 23°$, planar forward electromagnetic calorimetry at z=180 cm with $\pm 36°$ aperture and planar forward hadron calorimetry at z=220 cm with $\pm 27°$ aperture. The forward hadron calorimeter will be used for muon ID.

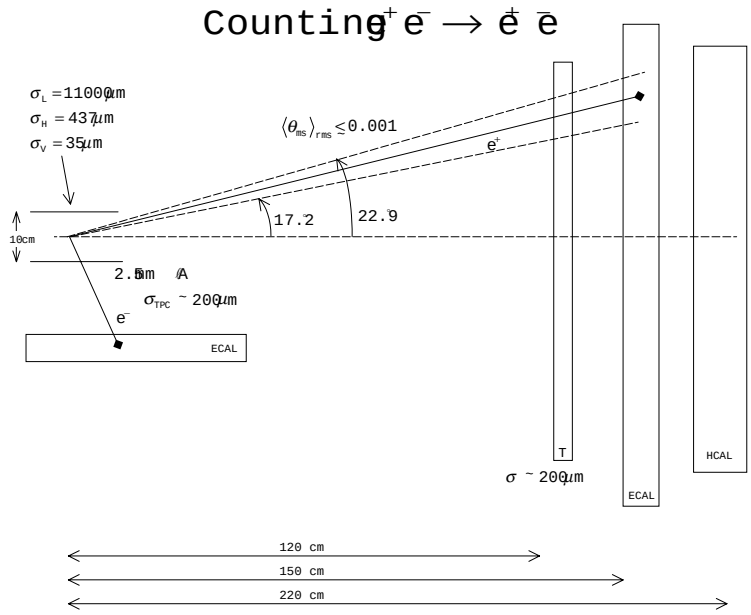

Figure 83: Geometry for counting Bhabha scatters.

5.7.4 Bhabhas

Both electron and positron can be identified at all angles since we have nearly 4π tracking and electromagnetic calorimetry. In order to get adequate statistics we must take advantage of the large forward cross section and count events in which one particle strikes the forward tracking chamber and forward electromagnetic calorimeter. It will certainly be helpful to identify the backward electron as well. The cross section, as seen in Table 18 is well over 100 nb at all energies. For good control of systematics, it will be useful to define an acceptance at a relatively large positron angle. This avoids relying on events in which the e^+ passes very obliquely through the beam pipe and reduces the angular accuracy and precision required to define the acceptance. However we wish events in which the forward track passes directly into the forward tracking chamber, missing the barrel calorimeter, as shown for example in Fig. 83. We give cross sections integrated between positron laboratory angles of 0.3 (17.2°) and 0.4 (22.9°). As seen in Figure 84, the corresponding electron appears at 28°-40° at $\sqrt{s} = 1.4$ GeV and 97°-114° at $\sqrt{s} = 3$ GeV, and is detected in the barrel calorimeter which extends backward to 157°. We will not be limited statistically in the Bhabha measurement. The acceptance determination requires that we measure angles to about 1.5 mr which should be relatively straightforward using the well defined interaction point and the forward tracking chamber about 120 cm from the interaction point with spatial resolution $\sim 200\mu$m. Multiple scattering is a consideration here. At 17.2°, the effective thickness of the 1 mm Al beam pipe is 0.038 radiation lengths for a rms multiple scattering angle of 0.7 mr.

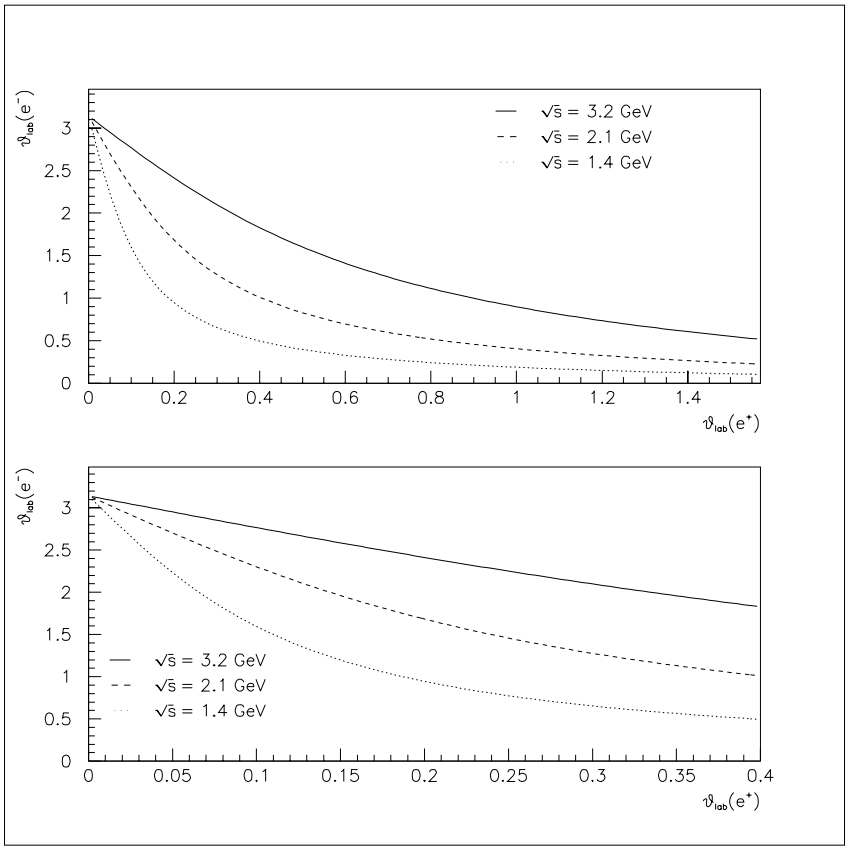

Figure 84: Bhabhas: electron v. positron laboratory angles.

5.7.5 Muon pairs

The muon pair cross section is much smaller and to obtain adequate statistics we would have to accept events at much smaller angles. Table 19 gives the integrated cross section between laboratory angles of 0.1 (5.7°) and 0.4 (22.9°). Even so the statistics will be marginal at the largest center of mass energies. The smaller angles would then require more precise angular measurements for the acceptance determination, i.e. about 0.5 mr. However the multiple scattering for a very forward muon passing obliquely through the beam pipe is much larger, i.e. at 5.7°, the effective beam pipe thickness is about 11% of a radiation length and the rms multiple scattering angle is about 1.2 mr. A thinner beam pipe would be desirable, or one with an angled window which is not obviously feasible at small angles. Muon pairs will be useful as a rough check of the Bhabha measurement but it will hard to obtain a precise luminosity because of statistical and systematic uncertainties.

5.8 Trigger

The experiment needs a very efficient trigger in order to minimize the systematics. In particular, the exclusive approach is very demanding from this point of view, requiring a

e^- energy	E_{cm}	θ^l_{min}	θ^l_{max}	$\cos(\theta^{cm}_{max})$	$\cos(\theta^{cm}_{min})$	σ(nb)
0.100	1.114	0.300	0.400	0.171	-0.120	280.499
0.200	1.575	0.300	0.400	0.477	0.222	174.436
0.300	1.929	0.300	0.400	0.618	0.404	152.080
0.400	2.227	0.300	0.400	0.699	0.517	143.612
0.500	2.490	0.300	0.400	0.752	0.594	139.480
0.600	2.728	0.300	0.400	0.789	0.650	137.151
0.700	2.946	0.300	0.400	0.816	0.692	135.706
0.800	3.150	0.300	0.400	0.837	0.725	134.748
0.900	3.341	0.300	0.400	0.854	0.752	134.080
1.000	3.521	0.300	0.400	0.868	0.774	133.596

Table 17: Cross sections for Bhabhas.

e^- energy	E_{cm}	θ^l_{min}	θ^l_{max}	$\cos(\theta^{cm}_{max})$	$\cos(\theta^{cm}_{min})$	σ(nb)
0.100	1.114	0.100	0.400	0.856	-0.120	62.416
0.200	1.575	0.100	0.400	0.925	0.222	25.226
0.300	1.929	0.100	0.400	0.950	0.404	14.103
0.400	2.227	0.100	0.400	0.962	0.517	9.093
0.500	2.490	0.100	0.400	0.969	0.594	6.372
0.600	2.728	0.100	0.400	0.974	0.650	4.721
0.700	2.946	0.100	0.400	0.978	0.692	3.641
0.800	3.150	0.100	0.400	0.981	0.725	2.895
0.900	3.341	0.100	0.400	0.983	0.752	2.358
1.000	3.521	0.100	0.400	0.985	0.774	1.958

Table 18: Cross sections for μ pairs.

well known efficiency for each channel. Moreover, luminosity measurement requires full efficiency for bhabha events. On the other hand, rejection of unwanted events due to cosmic rays and machine background is a crucial requirement.

A simple minimum bias trigger based on energy releases in the electromagnetic calorimeter has been studied to demonstrate the possibility to build a very efficient trigger for multihadronic events. However, calorimetric criteria are not sufficient to provide a good background rejection. A trigger based both on calorimetric and topological information is required in order to deal with the backgrounds.

The trigger efficiency has been studied generating some thousands of events for each channel and following the particles up to the electromagnetic calorimeter. The energy releases have been simulated according to the experimental data from the KLOE calorimeter for forward and barrel modules, having the same thickness as the ones from KLOE. An accurate Monte Carlo, based on GEANT, describing calorimeter modules, including lead, fibers and glue, has been used to parametrize the behavior of the pole and backward modules, comparing its results with KLOE. Impact angles and border effects have been

taken into account.

As a minimum bias trigger criterion, two energy deposits over a given threshold have been required. The EM calorimeter if fully efficient for photon energies above 40 MeV. Below this energy the appropriate efficiency curve has been used The simulation has been done accepting events with at least two releases over 2 MeV in fibers (corresponding to about 15 MeV incident gammas). This requirement is very realistic, being based on the behaviour of the 4m long modules of the KLOE calorimeter, which is now working in Frascati.

The main sources of background and their trigger rates with the minimum bias trigger are:

- Electroproduction on residual gas in the beam pipe: given an event rate of 770 Hz and a rejection factor of 2.8, the trigger rate is about 280 Hz.
- Cosmic rays: the trigger rate from this source is about 600 Hz.

In order to reduce the background without loosing efficiency some kind of topological information is required.

A very useful constraint would be to require that the particles originate from the beam crossing region. This in turn can be determined by measuring the mean z coordinate of the particles crossing the beam pipe. If we look at the distribution of the mean z position for different kinds of events, we obtain, as expected, an almost flat distribution along the beam pipe for the background events. Moreover, most of the particles come from the region upstream of the detector. On the other hand, the events produced in e^+e^- interaction show a well defined structure. In fig. 85 electroproduction events are compared with the global distribution of good events at 200 MeV and 500 MeV electron energy.

By cutting in z between -50. cm and +50. cm we can achieve a significant reduction of the background without losing in trigger efficiency. This cut allows to reduce electroproduction and cosmic trigger rate but is not efficient for some channels like, e.g., $e^+e^- \rightarrow K_S K_L$. The resulting rates are 120 Hz for electroproduction and 20 Hz for the cosmic rays. The overall efficiency ranges from 97.4% at 200 MeV e^- energy up to 99.3% at 800 MeV.

The trigger efficiencies for the some of the most significant hadronic channels at two different electron energies are shown in table 19.

The expected trigger rates are summarized in table 20.

If background levels are significantly higher than anticipated, special charged and neutral triggers will have to be used to keep the rates at acceptable levels.

The charged trigger could be designed as a two-level system. At the first level it requires the coincidence of fast signals from the hodoscope, hit multiplicity in the forward tracker and energy depositions in the calorimeters. The second level consists of a farm of microprocessors reconstructing tracks from the TPC and the forward chambers.

The neutral trigger will require at least three clusters in the EM calorimeters with suitable energy cuts.

A special trigger will be required for $n\overline{n}$ events, based on the energy depositions in the calorimeters and time-of-flight information at the second level.

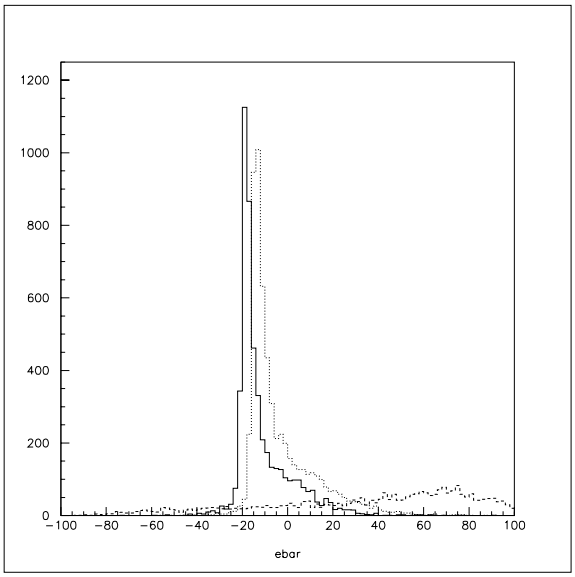

Figure 85: Mean z coordinate of particles crossing the beam pipe (in cm) for electroproduction (dashed line) and $e^+e^- \rightarrow hadrons$ events at 500 MeV (solid line) and 200 MeV (dotted line) electron beam energy.

Reaction	e^- **energy (MeV)**	**Efficiency**
$\pi^+\pi^-2\pi^0$	200	.990 ± .002
	800	.995 ± .002
$2\pi^+2\pi^-$	200	.987 ± .002
	800	.995 ± .002
$2\pi^+2\pi^-2\pi^0$	200	.995 ± .002
	800	.998 ± .002
k^+k^-	200	.770 ± .002
	800	.887 ± .002
Bhabha	200	.874 ± .002
$(0.3 < \theta < 0.4)$	800	.832 ± .002

Table 19: First level trigger efficiency for some hadronic channels at 1.6 and 2.1 Gev in the centre of mass.

hadrons + muons	$\sim$ 1 Hz
bhabha	$\sim$ 20 Hz
cosmics	$\sim$ 20 Hz
electroproduction background	$\sim$ 120 Hz

Table 20: Trigger rates.Cosmic and electroproduction rates are given for the VLER option.

6 Study of hadronic channels

A Monte Carlo program based on GEANT 3.21 has been developed. It includes:

- a detailed description of the detector geometry and materials and the beam line elements;
- an event generator for all relevant physics channels and beam gas background with the possibility to superimpose the latter on physics events;
- a simplified hit scoring;
- a fast treatment of resolutions and efficiencies.

No trigger requirements are taken into account. In all the simulations reported below we assume a spatial hit resolution of 200 μm for the TPC, 300 μm for the forward chambers and 1.5 cm/$\sqrt{\mathrm{E(GeV)}}$ for the calorimeters. The energy resolutions are 6%/$\sqrt{\mathrm{E(GeV)}}$ for the forward, barrel and rear calorimeter and 11%/$\sqrt{\mathrm{E(GeV)}}$ for the two pole calorimeters. Some of these values are slightly more conservative than those reported in the detector section.

All relevant physics processes are taken into account and in particular all electromagnetic and hadronic showers are fully developed.

One example of simulated $\pi^+\pi^-2\pi^0$ reaction in the detector is shown in figure 86. The same figure shows the TPC pad layout consisting of a number of concentrical layers, centered on the interaction region, varying from 24 (forward direction) to 8 (backward direction).

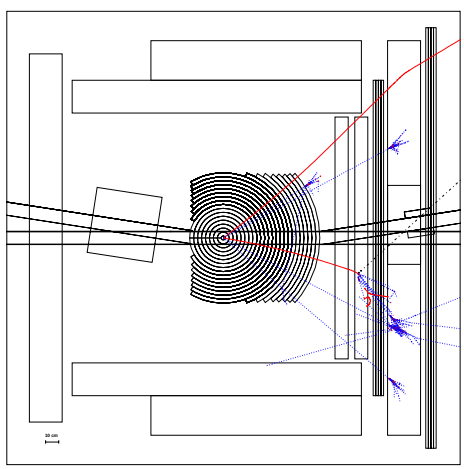

Figure 86: Top section of PEP-N detector. A $\pi^+\pi^-2\pi^0$ reaction is simulated. The charged pions are represented by solid lines and photons by dotted lines.

6.1 Features of multihadronic channels

A first estimate of the detector acceptance can be obtained by applying a Lorentz boost to a uniform distribution of charged particles and looking at the number of particles that are lost into the beam pipe. From figure 87 it can be noted that the geometric acceptance for a 100 mrad cut in the forward direction is ∼98%.

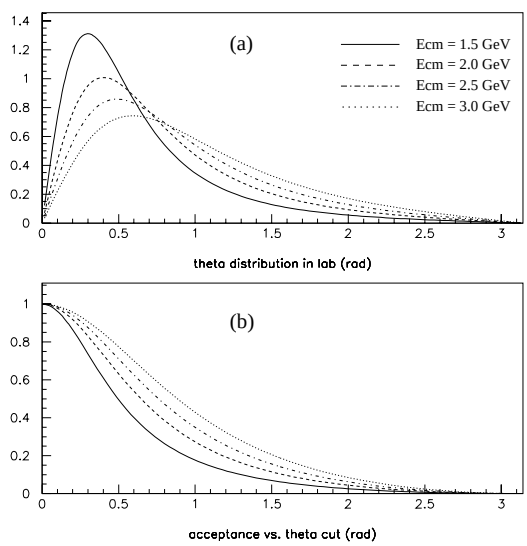

Figure 87: (a) Single particle θ distribution and (b) particle acceptance as a function of the polar angle cut for some values of the energy in CM. Cutting at 100 mrad the acceptance turns out to be about 98%.

In order to illustrate the main features of the multihadronic final states we show, in what follows, the results of simulations for the $\pi^+\pi^-2\pi^0$ channel, which is one of the most important reactions in our energy range.

6.1.1 Charged particles

Figures 88 and 89 show typical momentum and polar angle distributions for $\pi^\pm$ for various E_{cm} values. As expected the high momentum particles are located mostly in the forward direction, as shown in figure 90.

Particles moving close to the vertical direction hit few TPC layers so their momentum can not be measured. In any case the fraction of particles being emitted at small angle with respect to the vertical is small: as an example, for the 4π channel at 2.0 GeV, 0.5% of pions have a direction within $\pm 10°$ from the vertical, 1.4% within $\pm 15°$ and 2.4% within $\pm 20°$.

Figure 91 shows the TPC track detection efficiency as a function of the azimuhal angle for particles emitted with $10° < \theta < 120°$ if only tracks with a number of hit pad layers greater than 4 are selected. A lower efficiency affects the tracks emitted close to the vertical direction.

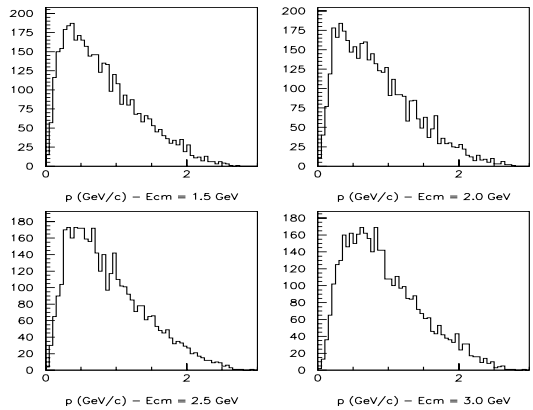

Figure 88: Momentum distribution of charged pions from $\pi^+\pi^-2\pi^0$ reaction for four values of CM energy.

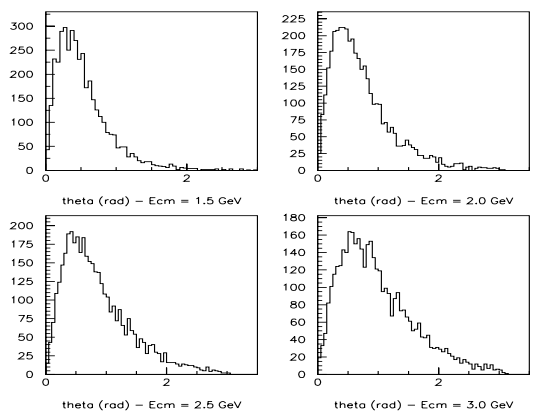

Figure 89: θ distribution of charged pions from $\pi^+\pi^-2\pi^0$ reaction for four values of CM energy.

6.1.2 Photons from π^0 decay

Figures 92 and 93 show typical energy and polar angle distributions for photons coming from a π^0 decay for various E_{cm} values. The peak of the distribution is at very low energy (below 300 MeV), moreover the high energy photons (above 1 GeV) are located in the forward direction at $\theta < 60°$, as shown in figure 94.

The distribution of photons in the various calorimeters varies with the energy. The results are summarized in table 21.

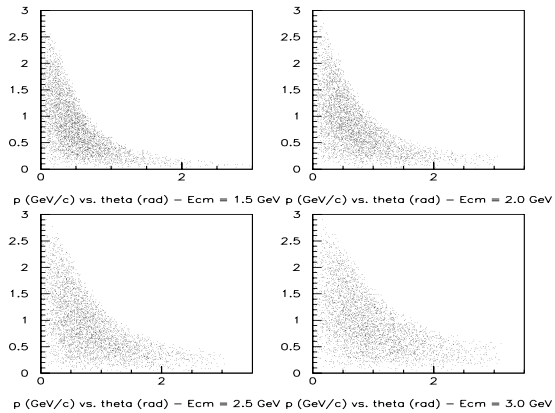

Figure 90: Scatter plot of momentum vs. θ distribution for charged pions from $\pi^+\pi^-2\pi^0$ reaction for four values of CM energy.

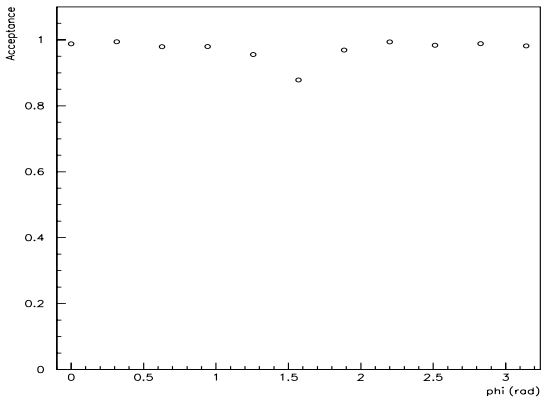

Figure 91: TPC track detection efficiency as a function of ϕ.

CM Energy	FCAL	BCAL	PCAL	RCAL	Not detected
1.5 GeV	54.3%	11.1%	29.9%	0.6%	4.1%
2.0 GeV	44.3%	15.7%	36.6%	0.8%	2.6%
2.5 GeV	37.3%	18.3%	41.7%	1.0%	1.7%
3.0 GeV	29.7%	20.9%	46.4%	1.1%	1.9%

Table 21: Distribution of photons in calorimeter system for four values of CM energy.

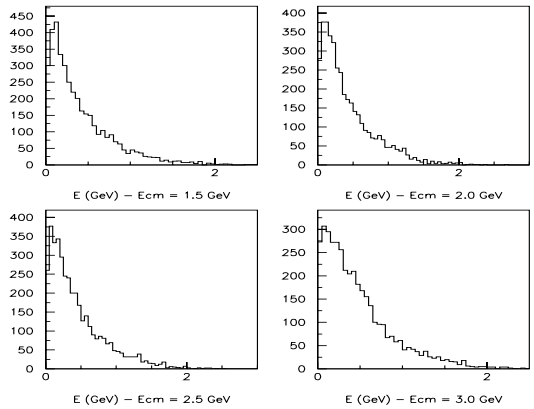

Figure 92: Energy distribution of photons coming from π^0 decay from $\pi^+\pi^-2\pi^0$ reaction for four values of CM energy.

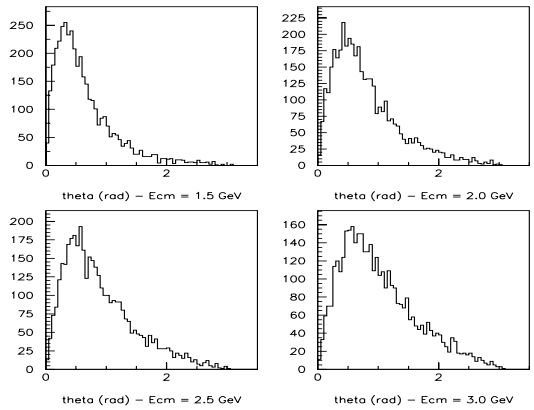

Figure 93: θ distribution of photons coming from π^0 decay from $\pi^+\pi^-2\pi^0$ reaction for four values of CM energy.

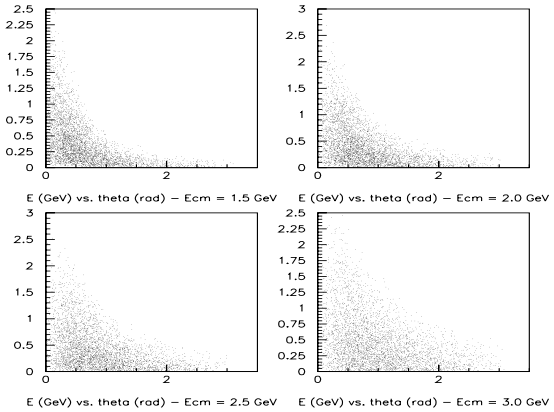

Figure 94: Scatter plot of energy vs. θ distribution for photons coming from π^0 decay from $\pi^+\pi^-2\pi^0$ reaction for four values of CM energy.

6.2 Contributions to hadron cross section

Table 22 gives an approximate estimate of the contribution to the total cross section for the most important hadronic final states at 1.5 GeV and 2.0 GeV.

Final state	1.5 GeV	2.0 GeV
$\pi^+\pi^-$	3%	-
$\pi^+\pi^-\pi^0$	4%	1%
$\pi^+\pi^-2\pi^0$	40%	21%
$2\pi^+2\pi^-$	36%	16%
$2\pi^+2\pi^-\pi^0$	2%	1%
$\pi^+\pi^-3\pi^0$	1%	0.5%
$2\pi^+2\pi^-2\pi^0$	6%	24%
$3\pi^+3\pi^-$	1%	5%
$\pi^+\pi^-4\pi^0$	2%	6%
K^+K^-	4%	1%
$K^+K^-\pi^0$	1%	3%
$K^+K^-\pi^+\pi^-$	-	8%
$K^+K^-2\pi^0$	-	4%
K_SK_L	-	0.5%
$K_SK_L\pi^+\pi^-$	-	4%
$K_SK_L2\pi^0$	-	1%
$p\,\overline{p}$	-	2%
$n\,\overline{n}$	-	2%

Table 22: Contribution to the total cross section for the most important hadronic final states at 1.5 GeV and 2.0 GeV.

6.3 Detector acceptance for multihadron

In order to calculate the acceptances for the various channels we used the following requirements for the identification of the various type of particle:

- $\pi^\pm$ or $K^\pm$: 5 or more TPC pad layers hit. Identification of π and K for $p < 1.5$ GeV is assumed to be done with dE/dx or time of flight (TOF) ($p < 0.6$ GeV) or aerogel (0.6 GeV < p < 1.5 GeV);
- γ: cut at 20 MeV and calorimeter efficiency applied.
- π^0: two photons with invariant mass equal to the π^0 mass within 2σ (see figure 95).

Table 23 gives the detection efficiency in the two cases in which all particles are detected or one particle is lost. For the detection of channels with $K^\pm$, at least one of the two is required to be identified by dE/dx, TOF or aerogel.

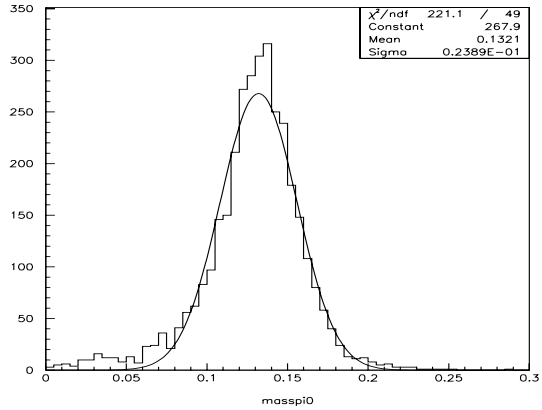

Figure 95: π^0 reconstructed invariant mass.

Final state	All detected	$\leq$ 1 lost
$\pi^+\pi^-\pi^0$	77.5%	96.6%
$\pi^+\pi^-2\pi^0$	66.1%	92.3%
$2\pi^+2\pi^-$	82.3%	98.6%
$2\pi^+2\pi^-\pi^0$	67.6%	93.6%
$\pi^+\pi^-3\pi^0$	54.4%	86.9%
$2\pi^+2\pi^-2\pi^0$	56.3%	88.6%
$3\pi^+3\pi^-$	70.6%	95.7%
$\pi^+\pi^-4\pi^0$	46.5%	81.0%
K^+K^-	24.4%	28.2%
$K^+K^-\pi^0$	58.3%	72.4%
$K^+K^-\pi^+\pi^-$	70.1%	87.9%
$K^+K^-2\pi^0$	57.0%	82.9%

Table 23: Detection efficiency for some multihadronic final states when all particles of the final state are detected and when at most one charged particle or one photon from π^0 decay is lost. For final states in which a $K^\pm$ is present, at least one of them is required to be identified as a kaon. The results are obtained for a CM energy of 2 GeV.

6.4 Some considerations on systematic errors on σ_{tot}

In the following we report some considerations on the accuracy that can be reached in the evaluation of the total cross section. Only fully reconstruted events are used. The sources of systematic errors we have considered are:

- the photon geometrical acceptance;
- misidentified final states;
- dynamical effects due to intermediate resonances;

- background contamination.

6.4.1 Geometrical acceptance for photons

One major source of uncertainty on the geometrical acceptance is the finite spatial resolution of the apparatus. The calorimeters are the detectors with the worst spatial resolution, hence the uncertainty on geometrical acceptance is mainly affected by the photon detection. The calorimeter system is hermetic except in the forward direction, therefore the dominant effect comes from the definition of the fiducial region around the 60×20 cm^2 hole in the forward calorimeter. Since the calorimeter spatial resolution is better than 2 cm, we have calculated the number ΔN of events with at least one particle in a 2 cm wide region around the hole. The fraction of detected events falling in this region is:

$$\frac{\Delta N}{N_{det}} \simeq 4.5\%.$$

The number of collected events will be at least $N_{det} \sim 10000$ for each energy point, therefore the events in this 2 cm boundary region will be $\Delta N \sim 450$. As a consequence the error on the determination of the number of events due to this boundary effect is:

$$\frac{\sqrt{\Delta N}}{N_{det}} \sim 0.2\%,$$

which is enough for our purposes.

6.4.2 Misidentified final states

Misidentified, lost or fake photons can lead to the misidentification of final states, in that they alter the number of reconstructed π^0. This effect will be less important if the detection efficiencies for the different channels involved are similar.

Contaminating channel	$\%\sigma_{tot}$	ϵ_{full}	Contaminated channel	$\%\sigma_{tot}$	ϵ_{full}	$\Delta\epsilon/\epsilon$
$\pi^+\pi^-2\pi^0$	21%	66.1%	$\pi^+\pi^-\pi^0$	1%	77.5%	0.17
$2\pi^+2\pi^-2\pi^0$	24%	56.3%	$2\pi^+2\pi^-\pi^0$	1%	67.6%	0.20

Table 24: Examples of contamination. ϵ_{full} is the detection efficiency for fully reconstructed events at $E_{cm} = 2.0$ GeV. The two channels listed are the ones having the highest cross sections at this energy.

Let us consider the examples in the table 24: due to the effect discussed above the $\pi^+\pi^-2\pi^0$ final state can be misidentified as $\pi^+\pi^-\pi^0$. Similarly $2\pi^+2\pi^-2\pi^0$ events could be wrongly recostructed as $2\pi^+2\pi^-\pi^0$. The relative error in the total cross section is related to the fraction $\Delta N_{mis}/N$ of misidentified events through the relation:

$$\frac{\Delta\sigma}{\sigma} = \frac{\Delta N_{mis}}{N}\frac{\Delta\epsilon}{\epsilon}$$

where ϵ is the detection efficiency of the contaminated channel, and $\Delta\epsilon$ is the difference in detection efficiencies between the two channels. In order to determine the expected level of misidentification we have performed a preliminary analysis on Monte Carlo events generated at the two values of E_{cm} = 1.36 GeV and E_{cm} = 2.09 GeV. We found a misidentification of the order of 2% or less. According to the above formula this translates into an error on the cross section

$$\frac{\Delta\sigma}{\sigma} \simeq 4 \times 10^{-4}$$

which is perfectly adequate for our purposes.

6.4.3 Dynamical effects

We have explored the variation of the detection efficiency due to resonances among the produced particles and the capability of separating the different intermediate states. As an example let us consider the reaction $e^+e^- \rightarrow \pi^+\pi^-2\pi^0$. This reaction can proceed via the two intermediate resonant states $\omega\pi^0$ (approximately 2/3 of the times) and $a_1\pi^0$ ($\simeq 1/3$), as illustrated in table 25.

	Prop.	ϵ_{full}	Generated events	Reconstructed events
$\omega\pi^0 \rightarrow \pi^+\pi^-2\pi^0$	$\sim 2/3$	58.0%	5980	5880 ± 390
$a_1\pi^0 \rightarrow \pi^+\pi^-2\pi^0$	$\sim 1/3$	64.1%	3140	3110 ± 380

Table 25: The numbers of reconstructed events are obtained from the fit on the mass spectrum in figure 96. The c.m. energy considered is E_{cm} = 1.36GeV. The detection efficiency for the non resonant case is 60.0 %.

The overall detection efficiency is different in two cases, the difference being mainly due to geometrical acceptance. If all $\pi^+\pi^-2\pi^0$ final states were reconstructed without any resonance, i.e. using only phase space to determine the acceptance, the error on the cross section measurement would be given by:

$$\frac{|\epsilon_{ps} - \epsilon_{res}|}{\epsilon_{ps}} \simeq 7\%$$

where ϵ_{res} and ϵ_{ps} are the overall detection efficiencies for the resonant and non resonant cases respectively.

However a preliminary analysis, whose results are presented in table 25, shows that we are able to distinguish between ω and a_1 production with a precision better than 12%.

Therefore an upper limit for the uncertainty due to this effect can be evaluated by multiplying the error on the detection efficiency by the error on the number of reconstructed events:

$$\frac{\Delta\epsilon}{\epsilon} \cdot 12\% \simeq 0.8\%.$$

The analysis of this channel indicates that the dynamical effects are under control. The study of additional final states is in progress.

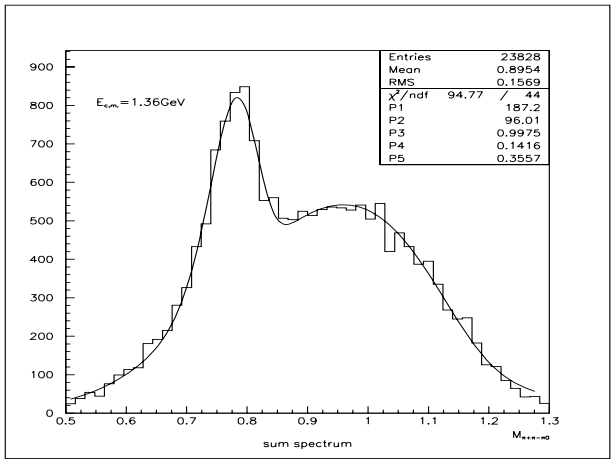

Figure 96: Invariant mass spectrum of $\pi^+\pi^-\pi^0$.

6.4.4 Background contamination

The most dangerous background is expected from the LER beam-residual gas multihadronic reactions near the interaction region. In order to study the effect of this component background events have been superimposed to multihadronic events This overlap will generate fake photons in the final state. The probability P that this overlap occurs is:

$$\text{background frequency} \cdot \epsilon_{\text{cal}}\ \text{T}_{\text{cal}} \simeq\ 300\text{Hz} \cdot 500\text{ns} \simeq\ 1.5 \cdot 10^{-4}.$$

It turns out that these fake photons can affect the fully reconstructed events at most in 10% of the cases, as we obtained in an analysis similar to the one described in subsection 6.4.2. In conclusion the effect of this background component on the total cross section measurement is completely negligible.

7 Nucleon antinucleon final states

The neutrons and anti-neutrons produced in symmetric e^+e^- collisions close to the $n\overline{n}$ threshold are characterized by a very low kinetic energy in the center of mass system ranging between a few MeV and several hundred MeV. Such neutrons are hard to detect with reasonably high efficiency using the same technique for all energies. In this respect the use of an asymmetric configuration where the two particles are boosted forward, each of them taking on average half of the energy of the most energetic beam, is a significant advantage. In the following we describe the main features of $n\overline{n}$ and $p\overline{p}$ final states in the proposed asymmetric configuration.

7.1 Kinematics

Assuming that we operate with the positron beam (LER) at a fixed energy $E_1 = 3.1$ GeV, and with the electron beam ranging between $E_2 \sim 100$ and 800 MeV, the processes $e^+e^- \rightarrow N\overline{N}$ can be studied from threshold, that is $s = (2 \times M_N)^2 \sim 3.5$ (GeV)^2 corresponding to $E_2 = 285\ MeV$ up to about $s \sim 9.0$ (GeV)^2. Data can be taken below threshold for background studies. Due to the boost from the center of mass to the laboratory reference system, the nucleons are emitted in the forward hemisphere with momenta ranging from hundreds of MeV to a few GeV. The distributions in the laboratory polar angle θ_{lab} with respect to the LER beam direction at four values of $E_{c.m.}$ are shown in Fig. 97. The distributions are obtained assuming an isotropic distribution in the center of mass system. The θ_{lab} distributions are characterized by sharp peaks at maximum angles θ_{max} whose values increase with $E_{c.m.}$. In order to have acceptance covering $-0.9 < \cos(\theta_{cm}) < 0.9$ an angular coverage from about 2° (for $E_{cm} = 1.9$) up to 90^o(for $E_{cm} = 2.8$) would be needed. The present detector has more limited coverage. Just above threshold, almost all the particles are below 5^0 and thus have low efficiency for detection in the TPC and forward calorimeter.

The distributions of laboratory momentum p are shown in Fig. 98. The higher the E_{cm} the larger the momentum spread. In particular, very close to threshold the particles are emitted at rest in the center of mass system, so each of them gets exactly half the total energy $(E_1 + E_2)$ when they are boosted to the laboratory system. We stress again that due to the boost, particles with momenta in the GeV range are obtained for all the values of E_{cm} even very close to threshold. This is a significant advantage of the asymmetric beam configuration over the symmetric one because the same detection technique can be used for all the values of E_{cm}. Fig. 99 shows the laboratory angle vs momentum for several different values of the center of mass energy. As the energy increases, the ranges of both nucleon momenta and angles also increase significantly.

7.2 Identification and measurement of $N\overline{N}$ final states.

Identifying $N\overline{N}$ The main features of $n\overline{n}$ and of $p\overline{p}$ final states are summarized below:

1. There is an angular correlation between the two particles. In the laboratory system the two particles emerge with opposite azimuthal angle ϕ (assuming perfectly head-on e^+e^- collisions) and with correlated values of θ_{lab} as shown in the plots of

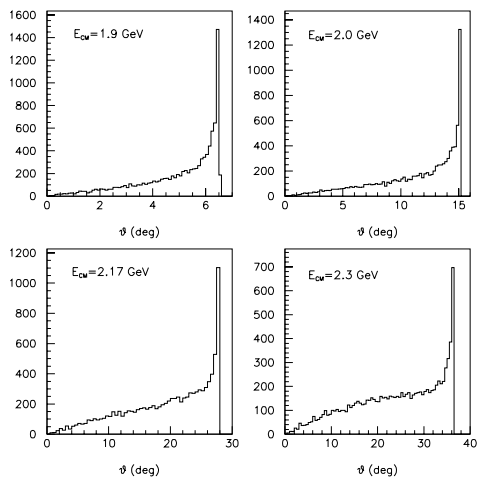

Figure 97: Examples of polar angle distributions in the laboratory system of nucleons and anti-nucleons at four different center of mass energies.

Fig. 100. These correlations can be used to identify the events provided the emission angles are measured with sufficient accuracy. It can be seen that this method is more difficult at small E_{cm} where small angular differences are involved. In Fig. 101 the angular correlation for $N\overline{N}$ at $E_{cm} = 2.5$ GeV is compared with $K\overline{K}$. They are well separated. Two body reactions with lighter particles are even further separated from $N\overline{N}$.

2. The velocity of the two nucleons in the laboratory system is significantly smaller than c in most of the region of interest, so that time of flight can be used to identify events and reject prompt photons and other fast backgrounds. In Fig. 102 the time of prompt particles and that of nucleons is shown as a function of p for a 2 m flight path. For the highest momentum, there is a difference of only 0.5 ns. At the lowest momentum the separation is just slightly longer than the 4.2 ns bunch separation. So at the extremes when one nucleon has very high momentum (and small angle) and the other low momentum there is a potential ambiguity with two prompt particles from adjacent bunches. However, in this case, the angular separation with other processes is particularly large (Fig. 101).

3. In the case of $p\overline{p}$, momentum analysis of both particles allows identification of the event, since the sum of energies of the two particles must equal E_1+E_2. Rejection of pions can be done by kinematics as well as using the dE/dx and Aerogel detectors described in the tracking section.

4. The interactions of 1 GeV nucleons and anti-nucleons with calorimeter materials allows in principle their distinction from electromagnetic showers based mainly on longitudinal shower profile. The size of the shower separates annihilating $\overline{N}$ from N.

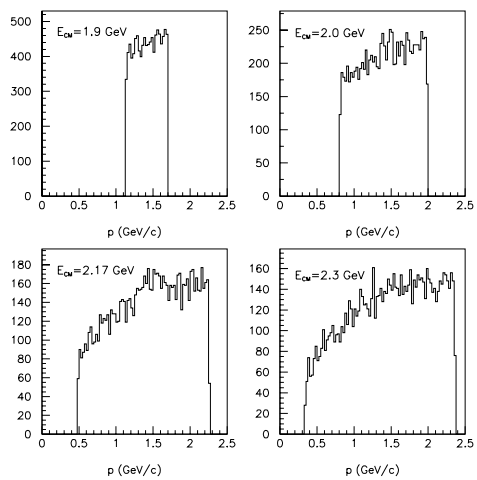

Figure 98: Examples of momentum distributions in the laboratory system of nucleons and anti-nucleons at four different center of mass energies.

5. The reaction $e^+e^- \to n\overline{n} + \pi^0$ can be separated from the two body reaction by the detection of the $\gamma\gamma$ from the π^0 in the electromagnetic calorimeter and by kinematic constraints described above. If $\pi^+\pi^-$ are produced, the kinematic separation is even cleaner.

Machine Backgrounds At PEP-N, $N\bar{N}$ pairs can be made in the process $e^+A \to e^+AN\bar{N}$, where A represents a nucleus present in residual gas or in the beam pipe. Even if the scattered e^+ is not observed in the detector, kinematical measurements (angles, energies, momenta) makes it possible to clearly distinguish these processes. This is particularly true for formation of $p\bar{p}$ where the fit is a four-fold constraint and the interaction point is well measured. For $n\bar{n}$, a signature that includes n and $\bar{n}$ is also highly over-constrained and background events are easily distinguished. A one-particle signature (e.g. $\bar{n}$ angles plus time of flight) is potentially vulnerable to background and has not been considered for the experimental signature.

Angular distributions The measurement of G_E and G_M requires a determination of the center of mass angular distributions. The combination of angles, momenta, TOF and baryon number measurements over-determines the kinematics. The measurement of θ_{lab} of only one particle is not sufficient to evaluate θ_{cm} because of a two-fold ambiguity due to the boost.

The current detector design imposes constraints on the acceptance for the proton and for the neutron with combined efficiency for the two particles of 80%(p) and 20%(n). Figure 103 shows the number of $N\overline{N}$ counts for 5 (pb^{-1}) under various assumptions. The rate drops with increasing E_{cm} because of the steeply dropping form factors, assumed here to be of the dipole form. Figure 104 shows the number of days of running required

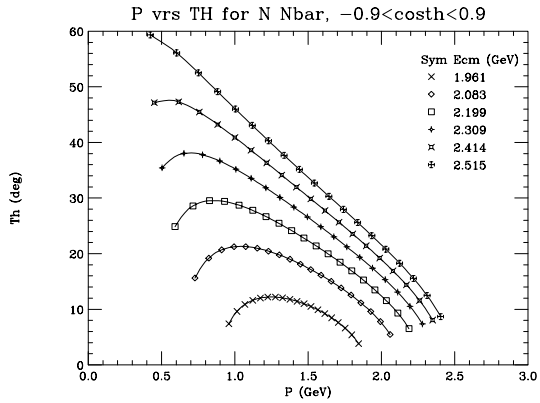

Figure 99: Laboratory momentum vs angle for several different values of center of mass energy.

to determine G_E^2/G_M^2 with an error of about 15 % with a luminosity of 5×10^{30} $cm^{-2}s^{-1}$. The time increases with increasing E_{cm} because of the lower counting rate and because of the decreasing relative contribution of G_E compared to G_M to the cross section. The time is longer for the neutron because of the low detection efficiency. A dedicated neutron detector with significantly higher efficiency and coverage to smaller angles would reduce the running time and enable us to make the measurement at higher E_{cm}. Some solutions are reported in the Appenidix IV.

In conclusion, it is possible to make an accurate determination of G_E^2/G_M^2 in the time like region using the same detector as for other physics. Better measurements are possible using a dedicated detector, especially for the neutron. The study of the region very close to threshold requires detection at very small angles not completely covered by the present detector.

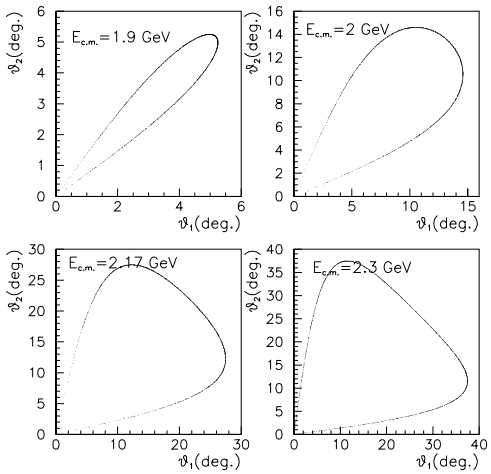

Figure 100: Angular correlations between the two nucleons at four different center of mass energies. θ_1 and θ_2 are the polar angles of the nucleons in the laboratory system.

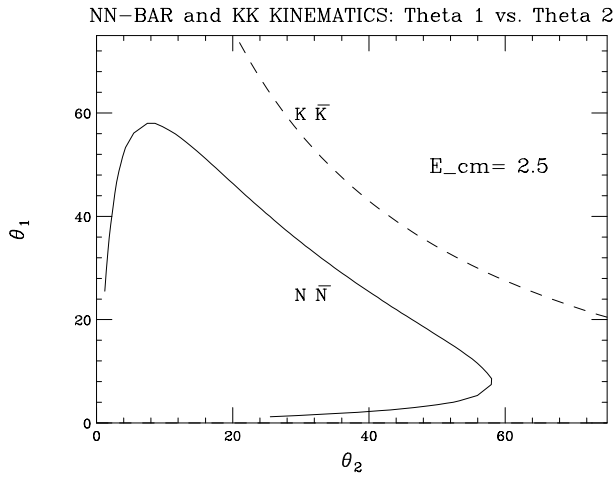

Figure 101: Angular correlation in the center of mass system for two-body final states $N\overline{N}$ and $K\overline{K}$.

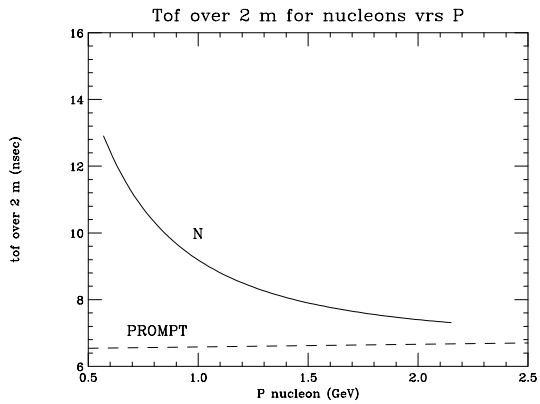

Figure 102: Time of flight of a nucleon and that of a photon for a 2 m distance as a function of particle momentum.

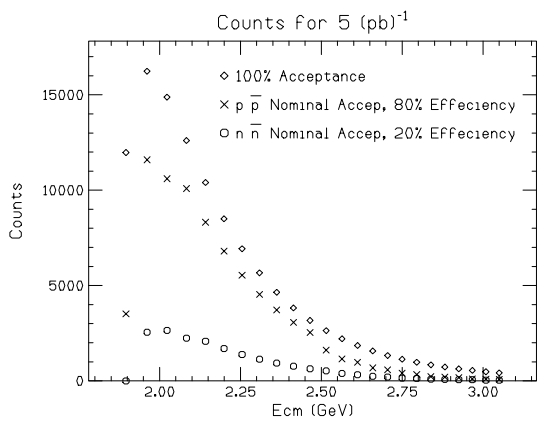

Figure 103: Number of $N\overline{N}$ events for 5 pb^{-1} as a function of E_{cm}.

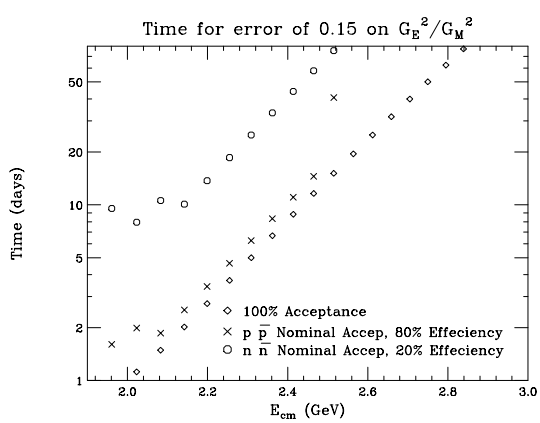

Figure 104: Days of running time at a luminosity of $5 \times 10^{30} s^{-1}$ to obtain an error of 0.15 on G_E^2/G_M^2 as a function of E_{cm}. Only statistical uncertainty is considered.

8 Conclusions

We have presented a comprehensive physics program at an asymmetrical electron-positron collider covering the energy range $1 < \sqrt{s} < 3$ GeV. There is a wide variety of important measurements that can be carried out in this energy regime: the high-precision (2 % or better) measurement of R, a complete study of nucleon, hyperon and meson form factors, vector meson spectroscopy and 2 photon processes.

We have presented a detector design capable of performing these measurements with the required levels of accuracy. A study of machine backgrounds indicates that these are well under control. Preliminary evaluations of the systematic uncertainties in the measurement of R show that these are within the requirements.

We envision what is effectively a program, rather than a single measurement, and we expect the active data taking period to last several years.

Appendix I
Nucleon time-like form factors

For $e^+e^- \to N\overline{N}$ the differential cross section in the c.m. is given by [202]:

$$\begin{aligned}\frac{d\sigma}{d\Omega} &= \frac{\alpha^2\beta C}{4s}\left[(1-P_LP_L')\left(|G_M(s)|^2(1+\cos^2\theta)+\frac{4M_N^2}{s}|G_E(s)|^2\sin^2\theta\right)\right.\\ &\left.+P_TP_T'\left(|G_M(s)|^2-\frac{4M_N^2}{s}|G_E(s)|^2\right)\sin^2\theta cos2\phi\right] \qquad (14)\end{aligned}$$

where β is the nucleon velocity in the c.m., s is the c.m. total energy squared, $G_M(s)$ and $G_E(s)$ are the magnetic and electric form factors, respectively , expected to be the analytical continuation of the space-like form factors $G_E(Q^2)$ and $G_M(Q^2)$. P_L and P_L' are respectively the longitudinal polarizations of the electron and positron and P_T and P_T' are the respective polarizations perpendicular to the storage ring plane. $G_E(0)$ is 1 for the proton and 0 for the neutron and $G_M(0)$ is 2.79 for the proton and -1.91 for the neutron, giving the static charge and magnetic moment of the nucleons. For the proton, $C \sim \frac{\pi\alpha}{\beta}/(1-e^{-\pi\alpha/\beta})$ is a Coulomb correction significant at very small nucleon kinetic energy and makes the cross section at threshold non-zero; $\sigma_p(4M_N^2) \simeq \pi^2\alpha^3|G_E|^2/(2M_N^2)$. Assuming that the Dirac form factor, $F_1 = (G_E - \frac{s}{4M_N^2}G_M)/(1-\frac{s}{4M_N^2})$, and the Pauli form factor, $F_2 = (G_M - G_E)/(1-\frac{s}{4M_N^2})$, are analytical through the $N\overline{N}$ threshold, we have $G_M(4M_N^2) = G_E(4M_N^2)$, i.e. exactly at threshold only S wave is present and the angular distribution is isotropic. At very high s the contribution from G_E is reduced by the helicity factor $4M^2/s$.

The proposed experiment at PEP-N anticipates separately obtaining G_E and G_M by studying the angular distribution given above. Most prior experiments in the time-like regime, with limited statistics and limited angular acceptance, were not able to separate G_E and G_M and data were analyzed to obtain $|G_M|$ only, using the scaling *ansatz* $|G_E| = |G_M|$ at all values of s. Experiment PS170 (LEAR) made an effort to separate G_E and G_M and with relatively large uncertainties report that $|G_E|/|G_M|$ falls with increasing (time-like) $|Q^2|$, contrary to *form factor scaling*. Recent TJNAF data [203] shows that in the space-like regime the ratio $|G_E|/|G_M|$ also falls with increasing $|Q^2|$. These data suggest that in the time-like regime, $|G_E|/|G_M|$ may fall by as much as 30% as $\sqrt{s}$ increases from threshold to ~ 6.25 GeV^2.

If transversely polarized colliding beams are available, additional power to separate $|G_E|$ and $|G_M|$ is obtained by studying the ϕ distribution of the differential cross section.

The cross sections for $e^+e^- \to N\overline{N}$ are roughly comparable; each is ~ 1 nb at a $\sqrt{s}$ of 2 GeV.

Appendix II
Meson time-like form factors

For $e^+e^- \to \pi^+\pi^-$, the differential cross section in the c.m. is given by:

$$\frac{d\sigma}{d\Omega} = \frac{\alpha^2\beta^3}{8s}\left[|F_\pi(s)|^2 \sin^2\theta\right] \tag{15}$$

where F_π is the pion form factor which is again the analytical continuation of the space-like form factor and $F_\pi(0) = 1$ A similar expression describes $e^+e^- \to K^+K^-$ where the kaon form factor is $F_K(s)$ and $F_K(0) = 1$. For $e^+e^- \to K^0\bar{K}^0$ we again have the same expression where $F_{K_0}(0) = 0$.

The reaction $e^+e^- \to V^+V^-$ where V is the ρ or K^* is not consistently described in QED, reflecting the well-known problem with renormalization in spin-one electrodynamics. One can describe the cross section either in terms of s-dependent helicity amplitudes that are coefficients of the following terms in the differential cross section: $sin^2\theta$, $(1+cos\theta)^2$ and $(1-cos\theta)^2$, or in terms of charge, magnetic moment and quadrupole moment form factors. Renard [202] gives the differential cross section for the formation of vector meson pair for the general case of polarized beams in terms of the latter. In either description the parameters are determined by the quark wave function of the vector meson in question.

The cross section for $e^+e^- \to \pi^+\pi^-$ at a $\sqrt{s}$ of 2 GeV based on existing data is ~ 0.5 nb and that for $e^+e^- \to K^+K^-$ is comparable. The cross section for annihilation to pairs of vector mesons is also expected to be roughly comparable as their wave functions are spatially similar to those of the vector mesons.

Appendix III
Form factors via initial state radiation at BABAR

We examine the possibilities for studying form factors in the low energy regime at BABAR, using events with hard initial state radiation, i.e. $e^+e^- \to \gamma + f$.
The rate of such events in the center of mass interval ΔW, $\dot{n}$, is :

$$\dot{n} \sim L_{PEPII} \cdot \sigma_W(e^+e^- \to f) \cdot \beta \frac{\Delta k}{k}[1 - \frac{2k}{W_0} + \frac{1}{2}(\frac{2k}{W_0})^2] \cdot \epsilon_{BABAR}$$

where:

- $W = \sqrt{W_0^2 - 2kW_0}$ is the c.m. energy after a photon of energy k has been emitted (W_0 is the PEPII c.m. energy),
- $\sigma_W(e^+e^- \to f)$ is the cross section for a final state f at a c.m. energy W,
- $\beta = \frac{4\alpha}{\pi}[log(\frac{W}{m_e}) - 0.5] \sim$ 0.083 is the Bond factor,
- $\Delta k = -\frac{W}{W_0} \cdot \Delta W$ is the radiative photon energy range corresponding to the c.m. energy interval ΔW,
- ϵ_{BABAR} is the BABAR detection efficiency for this kind of events.

The PEPII asymmetric configuration and the forward and backward BABAR acceptance are such that the detection efficiency is much higher in case of initial state radiation emitted by the high energy beam [204][205][206]. In this case the boost of the hadronic final state, because of the photon emission, is opposite to the PEPII boost ($\beta_{PEPII} = 0.49$) and it is, in the lab, $\beta_f = -0.81$ at $W = 2GeV$ and $\beta_f = -0.62$ at $W = 3\ GeV$.

For most of the reactions of interest it is necessary to detect the initial state radiative photon to suppress backgrounds from $\gamma\gamma$ interactions. The BABAR angular acceptance for these photons is $p_\gamma \sim 10$ %.

The BABAR effective luminosity L_{eff} for these events is then

$$L_{eff} \sim L_{PEPII} \cdot \beta \frac{\Delta k}{k}[1 - \frac{2k}{W_0} + \frac{1}{2}(\frac{2k}{W_0})^2] \cdot \frac{1}{2} \cdot p_\gamma \cdot \epsilon_{BABAR} \sim 2 \cdot 10^{27}\ cm^{-2}s^{-1}$$

where we take $L_{PEPII} \sim 3 \cdot 10^{33} cm^{-2}s^{-1}$, $\Delta W \sim 100\ MeV$ and $\epsilon_{BABAR} \sim 0.1$ [207].

The final state $p\overline{p}$ is considered first. Detection of the radiative photon may not be required for this simple topology as it may be possible to reject backgrounds by requiring equality of the forward missing energy and missing momentum, thanks to the very good DCH momentum resolution. To identify a several GeV $p\overline{p}$ pair the DIRC and several layers of the DCH must be hit. Therefore a minimum opening angle of the $p\overline{p}$ pair is required, which we estimate to be $\pm 30^o$, corresponding to a minimum $p\overline{p}$ invariant mass $M_{p\overline{p}} \geq 2.5\ GeV$. For higher $M_{p\overline{p}}$ the minimum opening angle corresponds to a cut in the $p\overline{p}$ c.m. angle θ^*. For $M_{p\overline{p}} \sim 3\ GeV$ we have $|cos(\theta^*)| \leq 0.28$, which precludes separation of the electric and magnetic form factors.

The expected number of events $N_{p\overline{p}}$ in the center of mass energy interval $2.35 \div 3.0\, GeV$ is no greater then 100- 200. Here we do not require that the radiative photon be detected and take a PEPII integrated luminosity of 100 fb^{-1} and cross sections of $\sim 70\ pb$ at $2.44\ GeV$, as measured by DM2 [68], and $\sim 6\ pb$ at $3\ \ GeV$, as measured by E835 [68] at FNAL by means of $p\overline{p} \to e^+e^-$. Detecting the radiative photon a similar rate can be foreseen: the loss of efficiency in detecting the photon will be compensated by the increase in $p\overline{p}$ detection efficiency.

A much smaller number of identified $n\overline{n}$ events is expected. In this case the radiative photon must be detected, due to the absence of a neutron (antineutron) momentum measurement, and the overall BABAR detection efficiency for a several GeV $n\overline{n}$ pair is less than ~ 10 % [206].

The prospect for an R measurement is under study [207]. For such a measurement the radiative photon must certainly be detected, for instance to suppress $\gamma\gamma$ multihadronic events.

Appendix IV
Dedicated hadron calorimeter for $n\overline{n}$ detection

We have studied which kind of hadron calorimeter is needed in our case for detecting with good efficiency both neutron and antineutron. It is under study the integration of this hadron calorimeter with the previously reported e.m. calorimeter as well as the best way to built this hadron calorimeter, eventually interleaved with tracking devices. Of course the extension in depth of the e.m. calorimeter would be the simplest solution, apart from the cost. We consider plastic scintillation counters with or without lead or iron absorbers. Further trackers can be inserted between the layers of plastic scintillator to allow tracking of the products of $\overline{n}$ annihilation and improve particle identification.

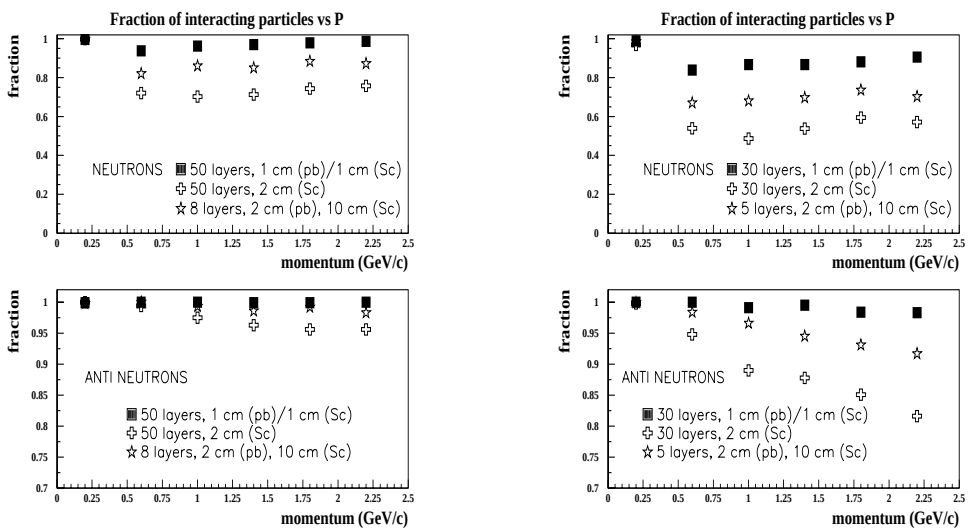

Figure 105: Probability of interaction for neutrons and antineutrons in the simulated calorimeter structure as a function of the particle momentum. 1 m thick calorimeters (configurations C1a, C2a and C3a) are shown in the upper plots, thinner calorimeters (configurations C1b, C2b and C3b (60 cm)) in the lower plots.

The efficiency for neutrons and antineutrons has been studied with a GEANT Monte Carlo simulation of lead-scintillator structures in the following configurations:

C1 : 1cm Pb + 1cm Scint. (a) 50 layers (b) 30 layers

C2 : 2cm Pb + 10cm Scint (a) 8 layers (b) 5 layers

C3 : only scintillator (a) 1 m thick (b) 60 cm thick

Option C2 is motivated by the possibility of using scintillator bars $10 \times 10 \times 160 cm^3$ equipped with photomultipliers at both ends available from another experiment [208]. Options (a) correspond to an overall thickness of 1 m, options (b) of 60 cm.

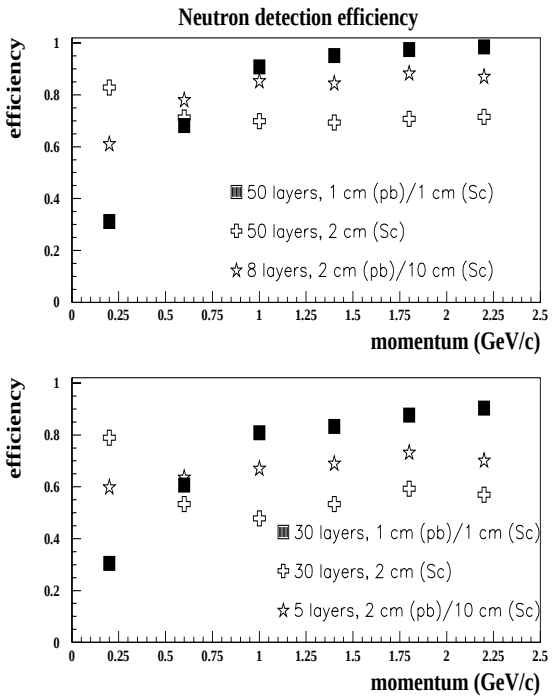

Figure 106: Efficiency for neutron detection as a function of neutron momentum for the considered calorimeter configurations.

Fig. 105 shows the probabilities of interaction for neutrons and antineutrons as a function of the particle momentum for the different configurations. The probability of interaction depends mainly on the mass of material. All of the configurations give an antineutron interaction probability larger than 80 %; smaller (but larger that 50 %) interaction probabilities are found for the neutron.

Results for the neutron efficiency are shown in Fig. 106. The detector is considered efficient when at least 4 MeV of energy is deposited in one scintillator layer. For momenta larger than 1 GeV/c the efficiency approaches the probability of interaction (compare with Fig. 105). For smaller momenta, the probability that the energy deposited in the scintillator by the interaction is below the fixed threshold becomes relevant, and depends mainly on the fraction of inert material. The drop in efficiency at low momenta is essentially due to neutron interactions where the proton does not escape from the lead (or iron). The configuration without lead gives a smaller but less energy-dependent efficiency.

References

[1] A. D. Martin, J. Outhwaite and M. G. Ryskin, J. Phys. G**26**(2000) 600.

[2] Z. Kunszt hep-ph/0003057.

[3] M. Davier and A. Hocker, hep-ph/9805470.

[4] S. Groote *et. al.* Phys. Lett B**440** (1998) 375.

[5] S. Eidelman, F. Jegerlehner, A. L. Kataev and O. Veretin, Phys. Lett B**454** (1999) 369; F. Jegerlehner, hep-ph/9901386.

[6] M. Swartz, Phys. Rev. D**53** (1996) 5268, hep-ph/9509248.

[7] S. I. Eidelman and F. Jegerlehner, Z. Phys. C **67**, 585 (1995).

[8] R. Alemany, M. Davier and A. Höcker, Eur. Phys. J. C **2**, 123 (1998).

[9] M. Davier and A. Höcker, Phys. Lett. B **419**, 419 (1998), *ibid* B **435**, 427 (1998).

[10] A. D. Martin and D. Zeppenfeld, Phys. Lett. B **345**, 558 (1995).

[11] H. Burkhardt and B. Pietrzyk, Phys. Lett. B **356**, 398 (1995).

[12] J. H. Kühn and M. Steinhauser, Phys. Lett. B **437**, 425 (1998).

[13] S. Groote et al., Phys. Lett. B **440**, 375 (1998).

[14] J. Erler, Phys. Rev. D **59**, 054008 (1999).

[15] A. D. Martin, J. Outhwaite, M. G. Ryskin, Phys. Lett. B **492**, 69 (2000), Eur. Phys. J. C **19**, 681 (2001).

[16] F. Jegerlehner, hep-ph/0105283.

[17] H. Burkhardt and B. Pietrzyk, Phys. Lett. B **513**, 46 (2001), LAPP-EXP2001-03

[18] J. F. de Trocóniz and F. J. Ynduráin, FTUAM 01-15, hep-ph/0107318, 2001.

[19] R. R. Akhmetshin *et. al.* (CMD-2 Collaboration), hep-ex/9904027.

[20] M. N. Achasov *et. al.* (SND Collaboration), hep-ex/9910057; Phys. Lett. b**462** (1999) 365.

[21] J. Z. Bai *et. al.* (BES collaboration), Phys. Rev. Lett. **84** (2000) 594.

[22] J. Z. Bai *et. al.* (BES Collaboration) , hep-ex/0102003.

[23] A. Gurtu, presented at ICHEP 2000, Osaka, 27 July-2 Aug., 2000.

[24] http://lepewwg.web.cern.ch/LEPEWWG/

[25] V. W. Hughes and T. Kinoshita, RMP **71** (1999) S133.

[26] H. N. Brown *et. al.* hep-ex/0009029, to be published in Phys. ReV. D62, Rapid Communications.

[27] H. N. Brown et al., Phys. Rev. Lett. **86**, 2227 (2001).

[28] M. Gourdin and E. de Rafael, Nucl. Phys. B**10**

[29] D. H. Brown and W. A. Worstell, Phys. Rev. D **54**, 3237 (1996).

[30] J. Erler and M.-X. Luo, Phys. Rev. Lett. **87**, 1804 (2001).

[31] J. F. de Trocóniz and F. J. Ynduráin, FTUAM 01-08, hep-ph/0106025, 2001.

[32] S. Narison, Phys. Lett. B **513**, 53 (2001).

[33] S. I. Eidelman, Talk at the II Workshop on e^+e^- Physics at Intermediate Energies, SLAC, April 30 - May 2, 2001.

[34] I. B. Logashenko, Talk at the II Workshop on e^+e^- Physics at Intermediate Energies, SLAC, April 30 - May 2, 2001.

[35] J. Denig, Talk at the II Workshop on e^+e^- Physics at Intermediate Energies, SLAC, April 30 - May 2, 2001.

[36] E. P. Solodov, Talk at the II Workshop on e^+e^- Physics at Intermediate Energies, SLAC, April 30 - May 2, 2001.

[37] M. Davier and A. Hocker, Phys. Lett. **B435**, 427 (1998).

[38] S. Eidelman and F. Jegenlehner, Z. Phys **C67**, 585 (1995).

[39] F. Jegerlehner, hep-ph/9901386.

[40] K. Melnikov, SLAC-PUB-8844 (2001), arXiv:hep-ph/0105267.

[41] M. Hawakawa and T. Kinoshita, Phys. Rev. **D57**, 465 (1996).

[42] J. Bijnens, E. Pallante, and J. Prades, Nucl. Phys. **B474**, 379 (1996).

[43] S. Laporta and E. Remiddi, Phys. Lett. **310**, 401 (1993).

[44] W. Marciano and B. Roberts, arXiv:hep-ph/0105056 (2001).

[45] H. N. Brown et al., (g-2) Collaboration, Phys. Rev. Lett. **86**, 2227 (2001)

[46] Y. S. Tsai, Phys. Rev. D4, 2821 (1971). H. B. Thacker and J. J. Sakurai, Phys. Lett. B36, 103 (1971).

[47] W. J. Marciano and A. Sirlin, Phys. Rev. Lett. **61**, 1815, (1988).

[48] S. I. Eidelman, Nucl. Phys. B (Proc. Suppl.) **98**, 281, (2001).

[49] F. J. Gilman and S. H. Rhie, Phys. Rev. D **31**, 324 (1985).
S. I. Eidelman and V. N. Ivanchenko, Phys. Lett. B **257**, 437 (1991).

[50] S. Anderson et al., Phys. Rev. D **61**, 112002 (2000).

[51] H. Czyż and J. H. Kühn, Eur. Phys. J. C **18**, 497 (2001).

[52] V. Cirigliano, G. Ecker and H. Neufeld, Phys. Lett. B **513**, 361 (2001).

[53] K. Melnikov, SLAC-PUB-8844, hep-ph/0105267, May 2001.

[54] D. Bisello et al., Nucl. Phys. B (Proc. Suppl.) **21**, 111 (1991).
(2001).

[55] S. J. Brodsky, G. P. Lepage, Phys.Lett. 87B (1979) 359; A. Duncan, A. M. Mueller, Phys.ReV. D21 (1980) 1636.

[56] S. J. Brodsky, G. P. Lepage, Phys.Rev. D22 (1980) 2157;

[57] A. Antonelli et al, Phys.Lett. B313 (1993) 283; A. Antonelli et al., Nucl.Phys. B517 (1998) 3.

[58] H. W. Hammer, U. G. Meißner, D. Drechsel, Phys.Lett. B385 (1996) 343.

[59] U. G. Meißner, Nucl.Phys. A623 (1997) 340.

[60] V. Chernyak, A. Zhitnitsky, Nucl.Phys. B246 (1984) 52.

[61] H. N. Li, G. Sterman, Nuc. Phys. **B381**(1992) 129-140; N. Isgur, C. H. Llewellyn-Smith, Nuc. Phys. **B317**(1989) 526-572; P. Kroll et al., Phys. Lett. **B316** (1993) 546-554.

[62] A. A. Logunov, N. Van Hieu,I. Todorov, Ann.Phys. (NY) 31 (1965) v203.

[63] D. Bisello et al., Nucl.Phys. B224 (1983) 379, LAL 88-58 (1988).

[64] M. E. Biagini, L. Cugusi, E. Pasqualucci, Z.Phys. C52 (1991) 631.

[65] R. Gatto, N. Cabibbo, Phys.Rev. 124 (1961) 1577; J. C. Körner, M. Kuroda, Phys.Rev. D16 (1977) 2165; M. Giannini, E. Santopinto, M. Krivoruchenko, Dubna, 1994; S. Dubnička, Nuovo Cimento A104 (1991) 1075; A. Z. Dubničkova et al., Z.Phys. C70 (1996) 473.

[66] J. Ellis, M. Karliner, H. Kowalski, Phys.Lett. B235 (1990) 341; G. Holzwarth, Z.Phys. A356 (1996) 339.

[67] G. Bardin et al., Nucl.Phys. B411 (1994) 3.

[68] G. Bassompierre et al., Phys.Lett. B68 (1977) 477; B. Delcour et al., Phys.Lett. B86 (1979) 395; D. Bisello et al., Z.Phys. C48 (1990) 23; T. A. Armstrong et al., Phys.Rev.Lett. 70 (1992) 1212; A. Antonelli et al, Phys.Lett. B334 (1994) 431; E835 coll. M. Ambrogiani et al., PR D60 (1999) 32002.

[69] V. A. Matveev, R. M. Muradyan, A. N. Tavkhelidze, Lett.Nuovo Cim. 7,15 (1973) 719; S. J. Brodsky, G. R. Farrar, Phys.Rev.Lett. 31 (1973) 1153.

[70] T. Gousset, B. Pire, Phys.Rev. D51 (1995) 15.

[71] C. B. Dover, Proc. 4th Int.Symp. on $N\overline{N}$ Int.,Syracuse(1975).

[72] I. S. Shapiro, Phys.Rep. 35 (1978) 129.

[73] R. L. Jaffe, Phys.Rev. D17 (1978) 1444.

[74] C. B. Dover and J. M. Richard, Ann.Phys. 121 (1979) 70.

[75] F. Myhrer and A. W. Thomas, Phys.Lett. 64B (1976) 59.

[76] A. Antonelli et al, Phys.Lett. B365 (1996) 427.

[77] R. Baldini, P. Gauzzi, S. Pacetti, E. Pasqualucci, Y. Srivastava, Eur.Phys.Jour. C11 (1999) 4.

[78] B. O. Kerbikov and A. E. Kudryavtsev, Nucl.Phys. A558, 177 (1993).

[79] P. Stoler, Phys. Rev. D 44 (1991) 73.

[80] A. Donnachie, H. Mirzaie, Z. Phys. **C33**(1987) 407.

[81] M.N. Achasov et al., Phys. Lett. B440: 442-448, 1998, hep-ex/9807016.

[82] CMD-2 Collaboration (R.R. Akhmetshin et al.), Phys. Lett. B462: 380, 1999, hep-ex/9907006.

[83] M.N. Achasov et al., Phys. Lett. B479: 53-58, 2000, hep-ex/0003031.

[84] M.N. Achasov et al., Phys. Lett. B485: 349-356, 2000, hep-ex/0005017.

[85] P.M. Ivanov et al., Phys. Lett. B107: 297, 1981.

[86] L.M. Barkov et al., Nucl. Phys. B256: 365-384, 1985.

[87] S.I. Dolinsky et al., Phys. Rept. 202: 99-170, 1991.

[88] E.V. Anashkin et. al., ICFA Instr. Bulletin 5: 18, 1988.

[89] M.N. Achasov et al., Nucl. Instrum. Meth. A449: 125-139, 2000, hep-ex/9909015.

[90] M.N. Achasov et al., Phys. Rev. D63: 072002, 2001, hep-ex/0009036.

[91] G.J. Gounaris and J.J. Sakurai, Phys. Rev. Lett. 21: 244, 1968.

[92] M. Bando et al., Phys. Rev. Lett. 54: 1215, 1985.

[93] N.N. Achasov et al., Sov. J. Nucl. Phys. 54: 664-671, 1991; Int. J. Mod. Phys. A7: 3187-3202, 1992.

[94] M. Benayoun, S.I. Eidelman, V.N. Ivanchenko, Z. Phys. C72: 221-230, 1996.

[95] N.N. Achasov and A.A. Kozhevnikov, Phys. Rev. D62: 117503, 2000.

[96] CMD-2 Collaboration (R.R. Akhmetshin et al.). BUDKERINP-99-10, Apr 1999, hep-ex/9904027.

[97] D. E. Groom et al. (Particle Data Group), Eur. Phys. Jour. C **15**, 1 (2000).

[98] I.B. Logashenko, hep-ex/0106101.

[99] D. Bisello et al., Phys. Lett. B220: 321, 1989.

[100] M. Benayoun et al., Eur. Phys. J. C2: 269, 1998.

[101] A. Antonelli et al., Z. Phys. C56: 15-19, 1992.

[102] S.I. Eidelman, V.N. Ivanchenko, Nucl. Phys. Proc. Suppl. 76: 319-326, 1999.

[103] M.N. Achasov et al., Phys. Lett. B462: 365-370, 1999, hep-ex/9910001.

[104] CMD2 Collaboration (R.R. Akhmetshin et al.), Phys. Lett. B466: 392-402, 1999, hep-ex/9904024.

[105] M.N. Achasov et al., Preprint IYaF 2001-34, Novosibirsk, 2001.

[106] V.N. Ivanchenko, In Proc. of Workshop on Hadron Spectroscopy, Frascati 1999, 667-676.

[107] CMD-2 Collaboration (R.R. Akhmetshin et al.), Phys. Lett. B489: 125-130, 2000, hep-ex/0009013.

[108] M.N. Achasov et al., Phys. Lett. B486: 29-34, 2000, hep-ex/0005032.

[109] D. Bisello et al., Nucl. Phys. Proc. Suppl. 21: 111, 1991.

[110] K.W. Edwards et al., Phys. Rev. D61: 072003, 2000, hep-ex/9908024.

[111] CMD-2 Collaboration (R.R. Akhmetshin et al.), Phys. Lett. B509: 217-226, 2001, hep-ex/0103043.

[112] A. Antonelli et al., Phys. Lett. B212: 133, 1988.

[113] M.N. Achasov et al., Nucl. Phys. A675: 391c-397c, 2000, hep-ex/9910057.

[114] J. Buon et al., Phys. Lett. B118: 221, 1982.

[115] D. Bisello et al., Z. Phys. C39: 13-19, 1988.

[116] D. Bisello et al., Z. Phys. C52: 227-230, 1988.

[117] S.I. Bityukov et al., Phys. Lett. B188: 383, 1987.

[118] V.M. Aulchenko et al., JETP Lett. 45: 145-147, 1987; Pisma Zh. Eksp. Teor. Fiz. 45: 118-120, 1987.

[119] D.C. Peaslee, Private communication.

[120] M. Atkinson et al., Nucl. Phys. B245: 189, 1984.

[121] D. Aston et al., SLAC-PUB-5722, Dec 1991. In *College Park 1991, Proceedings, Hadron '91* 75-78.

[122] OBELIX Collaboration (A. Bertin et al.), Phys. Lett. B408: 476, 1997.

[123] OBELIX Collaboration (A. Bertin et al.), Phys. Lett. B414: 220-228, 1997.

[124] A. Abele, Phys. Lett. B391: 191, 1997.

[125] A. Abele, Phys. Lett. B468: 178, 1999.

[126] D.M. Alde et al., Z. Phys. C66: 379, 1995.

[127] I.A. Koop, e-Print Archive: hep-ex/0106013.

[128] M. Benayoun et al., Mod. Phys. Lett. A14: 2605-2614, 1999.

[129] E.P. Solodov, e-Print Archive: hep-ex/0107027.

[130] N. Isgur, J. Paton, Phys. Rev. **D31**, 2910 (1985).

[131] T. Barnes, F.E. Close, E.S.Swanson, Phys. Rev. **D52**, 5242 (1995).

[132] UKQCD Collab., Nucl. Phys. **B63**, 203 (1998).

[133] C. Bernard *et al*, Nucl. Phys. **B73**,264 (1999).

[134] P. Lacock, K. Schilling, Nucl. Phys. **B73**,261 (1999).

[135] P. Page, E.S. Swanson, A.P. Szczepaniak, Phys. Rev. **D59**, 34016 (1999).

[136] UKQCD Collab., Phys. Lett. **B309**, 378 (1993).

[137] C. Morningstar, M. Peardon, Phys. Rev. **D60**, 34509 (1999).

[138] F.E. Close, P.Page, Phys. Rev. **D56**, 1584 (1997).

[139] A.D. Donnachie, Yu.S. Kalashnikova, Phys. Rev. **D60**, 114011 (1999).

[140] P.L. Frabetti *et al*, Phys. Lett. **B514**, 240 (2001).

[141] A.B. Clegg and A. Donnachie, Z.Phys. **C34**, 257 (1987).

[142] P.J. Franzini and F.J. Gilman, Phys Rev. **D32**, 237 (1985).

[143] A. Zallo, Proceedings of the PEP-N Workshop on e^+e^- physics at Intermediate Energies,SLAC, 30 Apr-2 May 2001.

[144] P.L. Frabetti *et al.* (E687 Coll.), flavors," EPS-HEP97,Jerusalem,19-26 august (1993).

[145] J. Gronberg et al., Phys. Rev. D **57** (1998) 33.

[146] M. Diehl et al.,PRL **81**(1998) 1782.

[147] M. Diehl, T. Gousset, B. Pire, hep-ph/0003233.

[148] V. G. Serbo, talk given at Photon 2000, 26-31 August 200 Ambleside U.K.(http::/photon2000.lancs.ac.uk/photon2000)

[149] G. R. Farrar, E. Maina, and F. Neri, Nucl. Phys. **B259** (1985) 702.

[150] J. F. Gunion and D. Millers, Phys. Rev. **D34** (1986) 2657.

[151] V. L. Chernyak and I. R. Zhitnitsky, Nucl. Phys. **B246** (1984) 52.

[152] TASSO, M. Althoff and others, Phys. Lett. **B130** (1983) 449.

[153] JADE, W. Bartel and others, Phys. Lett. **B174** (1986) 350.

[154] TPC/Two Gamma, H. Aihara and others, Phys. Rev. **D36** (1987) 3506.

[155] ARGUS, H. Albrecht and others, Z. Phys. **C42** (1989) 543.

[156] CLEO, M. Artuso and others, Phys. Rev. **D50** (1994) 5484.

[157] VENUS, H. Hamasaki and others, Phys. Lett. **B407** (1997) 185.

[158] M. Anselmino, P. Kroll, and B. Pire, Z. Phys. **C36** (1987) 89.

[159] C. F. Berger, Title: Exclusive two-photon reactions in the few GeV region, Diploma thesis, Technological University Graz (1997).

[160] M. Anselmino, F. Caruso, P. Kroll, and W. Schweiger, Int. J. Mod. Phys. **A4** (1989) 5213.

[161] P. Kroll, M. Schurmann, and W. Schweiger, Int. J. Mod. Phys. **A6** (1991a) 4107.

[162] P. Kroll, Th. Pilsner, M. Schürmann, W. Schweiger, Phys. Lett. **B316** (1993) 546

[163] P. Kroll, M. Schürmann, and P. A. M. Guichon, Nucl. Phys. **A598** (1996) 435.

[164] P. Kroll, M. Schurmann, and W. Schweiger, Z. Phys. **A342** (1992) 429.

[165] P. Kroll, M. Schurmann, and W. Schweiger, Z. Phys. **A338** (1991) 339.

[166] G. A. Schuler, hep-ph/9611249 (1996).

[167] G. A. Schuler, Comput. Phys. Commun. **108** (1998) 279.

[168] LPTURTLE code stems from Decay TURTLE, SLAC-246, (1980) modified by W. Kozaneki for SLC to include beam-gas bremsstrahlung and by D. Coupal and T. Fieguth for PEP-II.

[169] BaBar Technical Design Report, SLAC-R-95-457 (1995), page543.

[170] T. Sjöstrand, Computer Physics Commun. 82 (1994) 74

[171] J.F. Kral, "Simulation of trigger rates due to beam-gas background", BABAR note n.165, September 13, 1994

[172] J. Simkin and C.W. Trowbridge, "Three Dimensional Non-Linear Electro-magnetic Field Computations using Scalar Potentials". IEEE Proc., Vol 127 (Part B) No 6, 1980, November 1980.

[173] V. Azzolini and M. Placidi, "The PEP-N IP Magnet". Proc. e^+e^- Physics at Intermediate Energies Workshop, SLAC, Stanford, CA, April 30-May 2, 2001.

[174] S. Biagi, "Bagbolts-MONTE" computer program.

[175] NA-45-Private communication

[176] G. Rai, A. Arthur, F. Bieser, C.W. Harden, R. Jones, S. Kleinfelder, K. Lee, H.S. Matis, M. Nakamura, C. McParland, D. Nesbitt, G. Odyniec,D. Olson, H.G. Pugh, H.G. Ritter, T.J.M.Symons, H. Wieman, M. Wright and A. Rudge, IEEE Trans. Nucl. Sci. 37, (1990) 56; LBL-28141

[177] Bloom, Ronaldi, "Particle Detection with Drift Chambers," Springer-Verlag, Berlin, 1994.

[178] STAR experiment, RHIC, Brookhaven Natl. Lab.

[179] F. Sauli, Nucl. Instr. & Meth., A386 (1997) 531.

[180] Compass experiment, CERN.

[181] T. Mayer, ALICE experiment, private communication.

[182] NA-49 experiment, CERN.

[183] M. Adinolfi *et al.*, The KLOE electromagnetic calorimeter, submitted to Nucl. Inst. Meth. A. on 26/3/2001.

[184] M. Placidi *et al.*, The PEP-N IP dipole, PEP-N Workshop, SLAC, April 30-May 2, 2001

[185] M. Adinolfi *et al.*, The QCAL tile calorimeter of KLOE, submitted to Nucl. Inst. Meth. A on 20/4/2001.

[186] A. Antonelli *et al.*, Contruction and performance of lead-scintillating fiber calorimeter prototypes for the KLOE detector, Nucl. Inst. Meth. A354(1995)352-363.

[187] A.Onuchin et al., Nucl. Instr. and Meth. A 315 (1992) 517

[188] A.R.Buzykaev et al., Nucl. Instr. and Meth. A 379 (1996) 453

[189] A.R.Buzykaev et al., Journal of Non-Crystalline Solids 225 (1998) 381

[190] M.Yu.Barnykov et al., Nucl. Instr. and Meth. A 419 (1998) 584

[191] M.Yu.Barnykov et al., Nucl. Instr. and Meth. A 453 (2000) 326

[192] A.P.Onuchin, et al., 5th Int. Conf. Instr. for Colliding Beams Physics, Novosibirsk, 1990 (World Scientific,1990) p.208.

[193] A.G.Shamov and A.R.Buzykaev, Proc. of 'Computing in High Energy Physics 97', http://www.ifh.de/CHEP97/paper/212.ps

[194] V.V.Anashin et al., "Status of the KEDR detector", Vienna Conf. on Instrum., 2001

[195] A.R.Buzykaev et al., Nucl. Instr. and Meth. A 379 (1996) 465

[196] A.R.Buzykaev et al., Nucl. Instr. and Meth. A 433 (1999) 396

[197] A.F.Danilyuk et al., Nucl. Instr. and Meth. A 433 (1999) 406

[198] I.Adachi et al., Nucl. Instr. and Meth. A 355 (1995) 390

[199] Ecklund, S; Field,C; Mazaheri,G. A fast luminosity monitor sustem for PEP-II. SLAC-PUB-8688, Oct 2000. Submitted to Nucl.Instrum.Meth.

[200] Kleiss, R and Burkhardt, H. BBBREM-Monte Carlo simulation of radiative Bhabha scattering in the very forward direction. NIKHEF-H/94-01, Jan 1994 (hep-ph 9401333).

[201] A.E.Blinov *et al.*. Luminosity measurement with the MD-1 Detector at VEPP-4. *Nuc. Inst. Meth.* A273 (1988), 31-39.

[202] F. M. Renard, Basics of Electron Positron Collisions, Editions Frontieres, Gif sur Yvette, France (1981).

[203] M. K. Jones et al., Phys. Rev. Lett. 84,1398(2000).

[204] X. C. Lou, W. M. Dunwoodie, BABAR BAD XX.

[205] F. Anulli, R. Baldini, A. Calcaterra, R. DeSangro, D. Falciai, A. Zallo, BABAR note 437.

[206] R. Baldini, R. DeSangro, A. Palano, A. Zallo, BABAR note 223;
S. Bagnasco et al., BABAR BAD 56.

[207] E. P. Solodov, BaBar Note, in preparation

[208] Hongguo Zhu, "A Measurement of the Neutron Electric Form Factor in $\vec{D}(\vec{e}, e'n)p$ Quasi-elastic Scattering at $Q^2 = 0.5$ (GeV/c)^2", Ph.D Thesis, University of Virginia, August 2000, unpublished.